University of Poitiers

Faculty of Fundamental and Applied Sciences

M2 Internship Report

Completed at XLIM - UMR CNRS 7252

March 27 2023 - September 31 2023

Approaches for Ganglia and Neuron Detection in 3D Multivariate Cardiac Nervous System Images

---

Haydar JAMMOUL

M2 EUR SMART IOT

haydar.jammoul@etu.univ-poitiers.fr (till 15th of September) haydarjammoul.hj@gmail.com

Supervised by:
D. Noel RICHARD
D. Thierry URRUTY

Pedagogical tutor:
Prof. Christine Fernandez

Keywords: Computer Vision; Mathematical Morphology; Texture Analysis; AI; Light Sheet Imaging;

Acknowledgment

My deepest gratitude to **Dr. Clency PERRINE**, my master's director, for accepting my EUR program candidacy and fostering my research interests. Your unwavering support, guidance in my Ph.D. search, internship quest. I extend heartfelt thanks to my master's tutors, the I3M team, and the Tactic Graduate School. Your guidance over these two years has shown that education is more than just a profession; it's a platform to convey knowledge and passion. Your support, receptiveness, and promotion of interdisciplinary learning have been truly inspiring.

My gratitude extends to the Préti team, especially **Dr. Aurélien Chatelier** and **Jean-François Faivre**, for their open-door and willingness to address my curious inquiries. Your generosity in sharing insights and patience have been invaluable. I'm thankful to my colleague, **Alice Jean**, for sharing the journey's ups and downs during the acquisitions and internship.

To my internship tutor, **Thierry Urruty**, I owe a significant debt of gratitude. Your continuous guidance, vast experience, and valuable contacts have been pivotal. Your unwavering support has been invaluable. To my mentor and tutor, **Dr. Noël Richard**, my appreciation knows no bounds. Your scientific "descartesian" approach and pedagogical methodology have had a profound impact. Your guidance, engaging conversations, and unwavering assistance during my Ph.D. search and internship quest have been transformative. Your dedication to tutoring during this project, even during your busiest times and vacations, has been remarkable. Working alongside you has been a privilege. I'm grateful for the time and effort you invested, and I hope my contributions have been satisfying. Your influence and guidance have been transformative, and I'm honored to have worked with you.

Table 1: Notation Table

Binary Context	
B, D_B	Structuring Element (SE) and its spatial domain of definition
b_{ij}	Structuring Element (SE) element of B
ε_b, δ_b	Erosion and dilation in binary
$p = (x, y)$	Spatial coordinates of pixel x (integer)
$(x + i, y + j)$	Translated pixel coordinates (integer)
$I(p)$	Image function at spatial location p, whose value is a binary 0 or 1
η_b	Binary Hit or Miss
g', g''	Inferior and superior SE
I^c	Complement of binary image $I^c(p) = \begin{cases} 1 & \text{if } I(p) = 0 \\ 0 & \text{if } I(p) = 1 \end{cases}$
$\cap$	Logical AND
Grayscale Context	
B, D_B	Structuring Element (SE) and its spatial domain of definition
b_{ij}	Structuring Element (SE) element of B
ε_g, δ_g	Erosion and dilation in grayscale
$I(p)$	Image function at spatial location p, $I(p) \in [0, 2^{n-1}]$.
I^r	Reflection of I, $I^r(p) = I(-x, -y)$
$\|\overrightarrow{v}\|$	Vector norm
$>, <$	Superior and inferior signs for scalars
$\bigwedge(\cdot)$	Minimum of a set
$\bigvee(\cdot)$	Maximum of a set
g', g''	Inferior and superior SE
h'_g, h''_g	Value of g' and g'' at the spatial origin of g' and g'' respectively
$\tau = h'_g - h''_g$	Threshold of SOMP or MOMP
Color Context	
B, D_B	Structuring Element (SE) and its spatial domain of definition
b_{ij}	Structuring Element (SE) element of B
ε_c, δ_c	Erosion and dilation in Color.
$I(p)$	Image function at spatial location p, $I(p) \in \mathbb{R}^3$
$+_c$, $_c$	Addition and subtraction for color coordinates.
$\succ_c$, $\prec_c$	Superior and inferior signs for color coordinates.

$\succ_{CRA}$, $\prec_{CRA}$	Superior and inferior signs for color coordinates based on CRA(conditional ratio and angular distance ordering relation) ordering.
$\bigwedge_{CRA}(\cdot)$	Minimum of a set based on CRA ordering relations.
$\bigvee_{CRA}(\cdot)$	Maximum of a set based on CRA ordering relations.
Sup, $Sup[-1]$	Maximum coordinate and 2^{nd} maximum coordinate.
C_p	Color coordinates of pixel at position p
$\Delta E(C_{p_1}, C_{p_2})$	Perceptual distance between two color coordinates: the L2 norm in CIE lab space
$d(,)$	Distance.
h'_g, h''_g	Value of g' and g'' at the spatial origin of g' and g'' respectively
$\tau = \Delta E(h'_g, h''_g)$	Threshold of CMOMP
O^-, O^+	Color convergence points coordinates specidied uppon application.
O_2^-, O_2^+	Extended convergence points coordinates for erosion and dilation
I^r	Reflection of I, $I^r(p) = I(-x, -y)$
I^c	Complementary of I. [1]
$\circ_m$	Opening operation: erosion followed by dilation using the same structuring element.
$\bullet_m$	Closing operation: dilation followed by erosion using the same structuring element.
Spectral Context	
λ	Wavelength $\lambda \in \{\lambda_1, \lambda_2\}$ (Spectral image)
S	Image value as a function of λ (Spectral image)
$\mathcal{S}$	Input Set (Spectral image)
S^-, S^+	Spectral reference coordinates (Spectral image)
$\Delta(S_i, S_j)$	Distance between two arbitrary spectral functions

[1] Check Annex C.

Table 2: List of Abbreviations

Abbreviation	**Meaning**
EUR	Ecole Universitaire de Recherche
IoT	Internet of Things
Préti	Physiopathologie et Régulation des Transports Ioniques
PBS	Pole Biologie Santé
ICNS	Intrinsic Cardiac Nervous System
MM	Mathematical Morphology
SE	Structuring Element
CRA	Conditional Ratio and Angular Distance Ordering Relation
VOI	Volume of Interest
DL	Deep Learning
AI	Artificial Intelligence
PCA	Principal Component Analysis
SNR	Signal to Noise Ratio
SOMP	Single Object Matching using Probing
MOMP	Multiple Object Matching using Probing
CMOMP	Color Multiple Object Matching using Probing
MMOMP	Multivariate Multiple Object Matching using Probing
ChAT	Choline Acetyltransferase
PGP	P-glycoprotein
TH	Tyrosine hydroxylase
KLPD	Kullback-Leibler pseudo- divergence
BRATS	The Multimodal Brain Tumor Segmentation Challenge
VGG16	Visual Geometry Group 16

Contents

1 Introduction

The EUR Ceramics & ICT - TACTIC Graduate School provides education in the fields of Ceramics and Information and Communication Technologies. The University of Limoges, in collaboration with the University of Poitiers and the CNRS, is conducting the graduate school. In the EUR smart IoT program students acquire not only in-depth knowledge of the IoT discipline, but also a better understanding of future social concerns from the realm of research.
As part of my M2 master's in EUR Smart IoT at Poitiers University, I chose to complete a 6-month internship in a research interdisciplinary project. This decision aligns with my long-term professional goal of pursuing research in the domain of computational sciences at the interface of biology. The project involved collaboration between researchers from the fields of pathology (Préti researchers) and AI/Image and signal processing (XLIM - ICONES team) at the University of Poitiers, where my research internship was affiliated with the ICONES team.
The heart's functions, including heart rate, contractility, and conduction velocity, are regulated by a network of peripheral neurons known as the intrinsic cardiac nervous system (ICNS). The intrinsic cardiac nervous system consists of three main elements: ganglia, neurons, and fibers. Ganglia are clusters of nerve cell bodies interconnected by inter-ganglionic fibers. Figure **??** displays an image of the intrinsic cardiac nervous system of a mice heart acquired through light sheet imaging. Figure **??** shows a typical cardiac nerve (indicated by a black arrowhead) and two ganglia (indicated by white arrowheads). Figure **??** depicts cardiac neurons (white arrows) and inter-ganglia fibers (black arrows) within the intrinsic cardiac nervous system (ICNS).

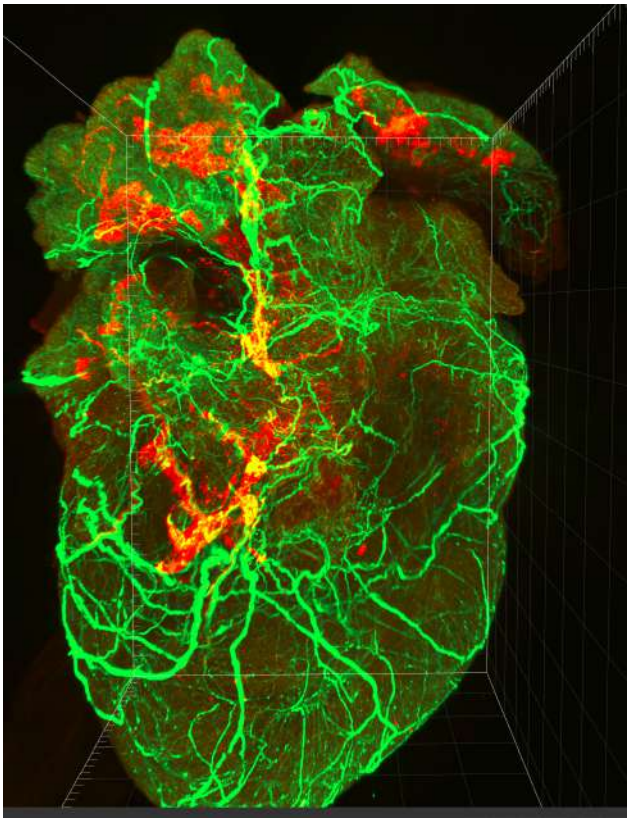

Figure 1: 3D cellular image visualizing the intrinsic cardiac nervous system (ICNS) of a mice heart using light sheet microscopy. Green is TH antibody response and red is PGP response.

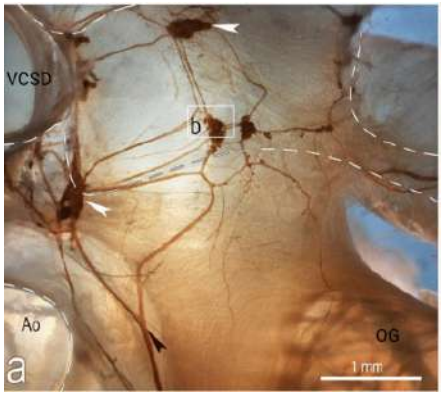

(a) A typical example of a cardiac nerve is indicated by the black arrowhead. The two white arrowheads show two ganglia. (VCSD: Superior vena cava; OG: Left atrium; Ao: Aorta)

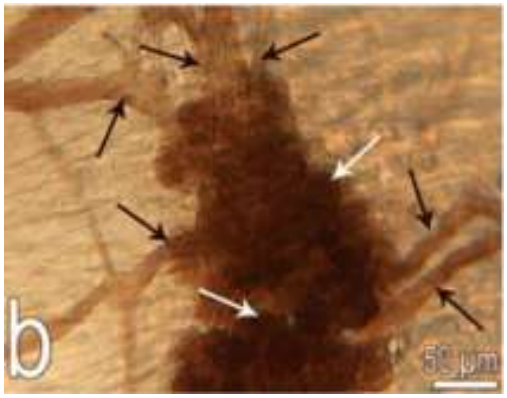

(b) b is a zoom to ganglia in the white square in image a. The white arrows point to cardiac neurons, while the black arrows indicate inter-ganglia fibers.

Figure 2: Images showing intrinsic cardiac ganglia and their interconnections [**?**] in mice hearts that were visualized through a histochemistry protocol, which is different from the light sheet microscopy used.

The researchers at Préti are exploring the relationship between characteristics of heart structures and cardiac arrhythmia. Lizot et al.[**?**] demonstrated that the mouse Intrinsic Cardiac Nervous System (ICNS) is a suitable model for studying cardiac function and arrhythmia. The Préti researchers aim to analyze 3D cellular images of cleared(transparentized) mouse heart using light sheet microscopy, as shown in Figure **??**. **The proposed subject for the internship is to develop an automatic detection of the neurons, and consequently the ganglia.**

The rest of the report is organized as follows: First, we will detail the acquisition protocol and pose the problematic of the internship. **Second**, we will explain the proposal we had to analyze shapes and contrast in the image. **Third**, we will delve into the analysis of the images and their pre-treatments. **Fourthly**, we will present the primary results we obtained when applying morphological probing to mice heart images. **Fifth**, we will present the work environment, the project management, the risk assessment, and how we adapted to the risks that occurred. **Finally**, we will conclude this report.

2 Problematic, Images and measures

In this section, **first** we will present the acquisition protocol of the **mice heart intrinsic nervous system**, then we will proceed to present the **problematic** of this internship.

2.1 Context

To better understand the correlation between cardiac arrhythmia and the role of the ICNS structures to it the PRéti researchers seek to compare the characteristics of ICNS structures at mice heart presenting the arrhythmia pathology and those that don't. By introducing genetic modifications to replicate arrhythmia pathologies, researchers can investigate the underlying mechanisms in a controlled experimental environment. Utilizing light sheet imaging of these mice hearts provides a three-dimensional representation of the ICNS, enabling comprehensive characterization and a better grasp of its relationship with cardiac arrhythmias in mice hearts. To characterize the ICNS Préti researchers want to notably detect the ganglia inside the mice heart, count them, measure their volume and count the neurons within them.
The main focus of this internship is to develop tools to detect neurons and ganglia from 3D multivariate cellular images of the mouse heart ICNS.

2.2 Problematic

Detecting and characterizing the ICNS structures manually can be challenging and time-consuming(images of 20 GB, thousands of 2D z-slices). **This characterization involves differentiating ganglia from fibers or noise, measuring their volumes, and counting neurons within ganglia structures**. To manually count the neurons within a ganglia, biologists would tally the neurons every few slices to approximate the count. However, this method lacks precision due to the three-dimensional nature of neurons, which are similar to ellipsoids (figure **??**).

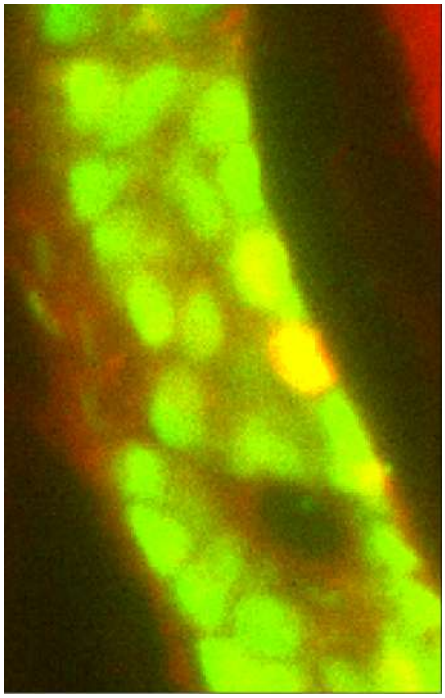

Figure 3: A 2D slice of neurons (elliptic green or yellow shapes) forming a ganglia, captured using light sheet microscopy and labeled with PGP and THE antibodies.

Before my internship, multiple projects attempted to implement Deep Learning to contribute to the automatic characterization of ICNS, yet they didn't yield success. One example is M. Coupet's UNET model, influenced by the UNET's first application for the segmentation of neuronal structures in electron

microscopic stacks [?]. Some might question this choice, given the project's absence of manual binary masks similar to the BRATS dataset, which would facilitate mask reconstruction and metric assessment like the DICE score. Another potential Deep Learning approach could involve utilizing classified volumes and neural network models or leveraging transfer learning, such as VGG16[?], for volume classification. Consequently, this enables the use of a confusion matrix to assess the model's performance. However, these approaches can't quantify ganglia volume or neuron counts due to their lack of metrology. Labeling the images with tasks like neuron counting posed difficulties due to uncertainties in human extraction, limiting the performance of an AI-based solution. Given the incomplete dataset and the challenges associated with measurements, these Deep Learning methods weren't pursued.

In this report, we will be focusing on Mathematical Morphology for the analysis of the images since prior implemented Deep learning-based methods did not yield good results due to the lack of enough data and normalization. As shown in Figure **??** above, it is notable that neurons often have a particular shape. These shapes are defined by a specific multivariate response of the antibodies. Therefore, we explored the possibility of using probing techniques to detect these shapes and count the neurons. This led us to focus on **Mathematical Morphology**, which is the study of shapes in images, particularly using probing techniques. **The challenge is to implement these methods for multivariate images and define the needed template to be probed**.

Although multivariate probing is not an automatic approach, it allows us to define both an inferior and a superior template. This permits the detection of objects that fall between these two templates, allowing for a margin of differences. This degree of liberty is advantageous as biological structures are not perfectly uniform. Additionally, it gives the expert control of the target templates, facilitating interaction with expert knowledge similar to a form of learning by interrogation.

2.3 Acquisition protocol

To enable the three-dimensional imaging of mice hearts and the examination of the ICNS, a preparatory process known as the iDISCO protocol is employed. This protocol involves clearing the heart tissue, rendering it transparent, and applying immunolabeling to highlight specific structures. The iDISCO protocol enhances visualization by eliminating tissue opacity. Illustrated in Figure **??**, the Cardiac Clearing Protocol follows a multi-step approach to ready heart tissue samples for cellular imaging.

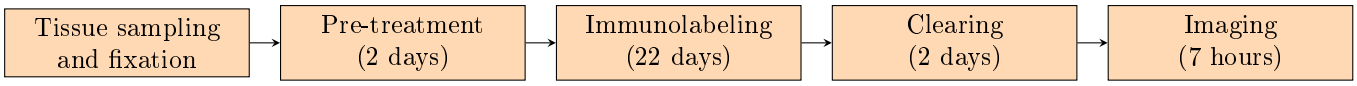

Figure 4: Steps of cardiac clearing protocol iDISCO prior to imaging a tissue.

Particularly, this protocol includes the **Immunolabeling** stage. During this stage, antibodies labeled with fluorescent dyes (fluorophore) are used to specifically target and visualize proteins of interest within a sample. In this protocol, the biologist team will use three different antibodies: tyrosine hydroxylase (TH), choline acetyltransferase (ChAT), and P-glycoprotein (PGP). These antibodies are enzymes found in neurons and are commonly used as markers for the ICNS. As shown in Figure **??**, when excited with a laser beam at a precise frequency, the fluorophore will emit a fluorescent signal that can be captured by the camera to construct the image of the ICNS.

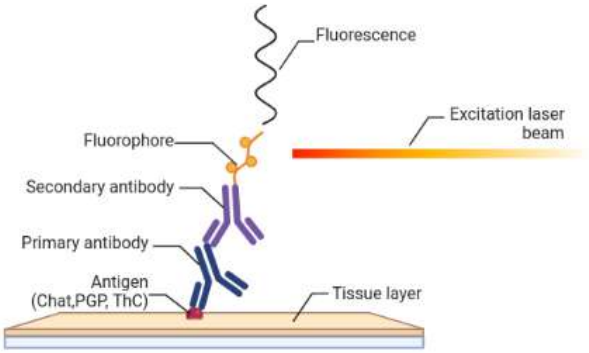

Figure 5: Immunofluorescence concept. During immunolabeling, primary antibodies bind to antigens inside the neurons, while secondary antibodies bind to the primary antibodies. When excited by a laser beam during light sheet microscopy acquisition, the fluorophore on the secondary antibodies emits a fluorescent signal that is captured by the camera.[2]

Light sheet microscopy is a fluorescence microscopy technique used to capture high-speed three-dimensional images of biological samples. A photograph of the Préti microscope, and the setup are shown in figure **??**. The technique involves illuminating a thin plane within the sample using a sheet of laser light and capturing images from the illuminated plane. The sample is then scanned in the z dimension to capture a series of two-dimensional images which are later combined to produce a three-dimensional image of the sample. This results in the creation of a 3D image of the sample.

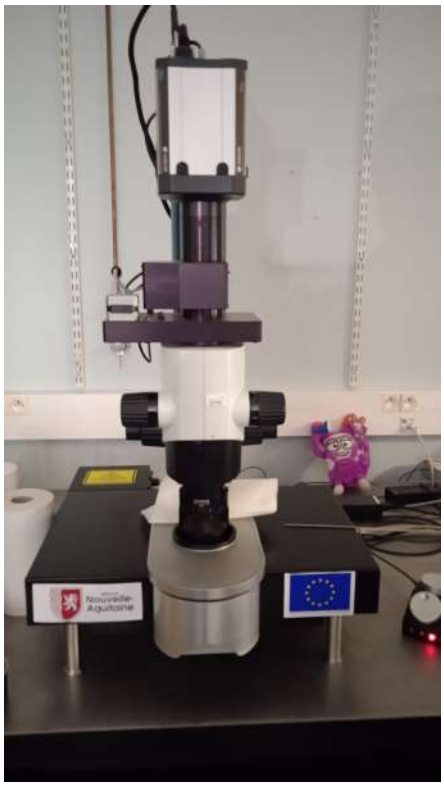

(a) Préti Labratory light sheet microscope

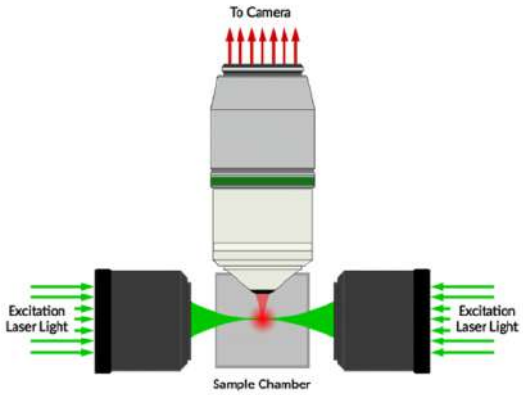

(b) Light sheet Microscope setup [**?**]

Figure 6: Light Sheet Microscope

[2]Image generated using Biorender software.

2.4 Acquired bi-valued images

The following figure ?? shows the Mice heart excited by two different laser beams. One for each fluorophore which immunolabel different types of neurones. Exciting the heart tissue with laser frequencies in 2D planes along the z direction results in the acquisition of a 3D cellular image. Both acquistions will construct a bivalued image of the ICNS as in figure ?? or ??.

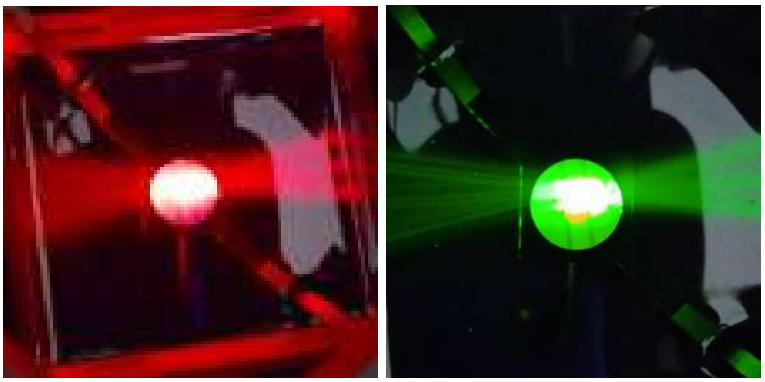

(a) Heart excited by 1^{st} laser beam (b) Heart excited by 2^{nd} laser beam

Figure 7: Heart under Light Sheet Microscope. Image beam acquired at the objective's location.

2.5 Challenges in Dataset Construction and Image Analysis

The creation of a dataset serves two critical purposes: it provides insights into images for non-biologists and establishes a foundational basis for training algorithms. Such datasets are relatively rare, with Préti standing as a global pioneer in conducting light sheet acquisitions on mice hearts. Constructing a ground truth dataset involves challenges. One approach is employing binary masks, as seen in the "BRATS dataset" for MRI images [?], where manual segmentation of ICNS structures like ganglia occurs. However, this technique demands significant expert time and resources. Alternatively, expert classification of volumes containing specific ICNS structures or noise is an option. These datasets must accommodate intra-class variability, including diverse shapes and sizes of image crops containing fibers and ganglia. Préti currently possesses volumes with ganglia samples for ChAT and TH acquisitions.
These acquisitions come with several challenges, notably the inability to perform normalization due to the absence of a "white reference" for acquisition. Images display various artifacts, confounding the differentiation of noises, fibers, and ganglia for biologists. Some artifacts stem from marker volatility or unpredictable reactions, alongside the limited reproducibility of these acquisitions. An artifact type, the "aggrega," visible in Figure ??, can be mistaken for ganglia and arises from antibody attachment imperfections. Subsequent sections will explore image noise and acquisition hurdles.
Reproducibility in these acquisitions is hampered by biological tissue diversity, where factors like age and body composition introduce variations. Furthermore, human involvement during the iDISCO protocol adds variability, turning each acquisition into a unique adventure that might entail new challenges.

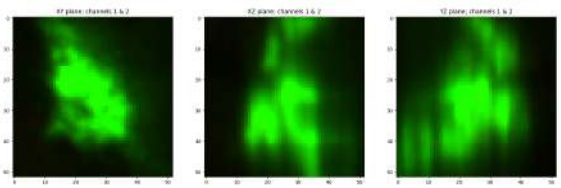

Figure 8: Aggrega noise that can be confused with ganglia. Captured using light sheet microscopy and labeled with ChAT and TH antibodies.

In the following section, we will discuss multivariate MM probing we implemented to detect specified shapes in the bi-valued images.

3 Proposed probing method

In this internship, we focused primarily on **mathematical morphology (MM)** and **probing techniques**, as **deep Learning (DL)-based methods** did not yield successful results on the acquired images. Firstly, we will introduce MM as initially proposed for **binary images**, including the **hit or miss transformation used to detect templates in binary images**. Secondly, we will explore previous works on extending MM operators and the hit or miss transformation to **grayscale images**, referred to as multiple object matching using probing **MOMP**. Finally, we will discuss the challenges and considerations involved in extending these techniques to **color and multivariate images**.

3.1 Mathematical Morphology (MM)

One purpose of image analysis is to identify spatial objects within images, which often encompass geometrical shapes with varying luminance or color contrasts [**?**]. Mathematical morphology leverages these spatial and contrast characteristics to offer a toolkit for extracting valuable information, referred to as feature extraction.
Mathematical morphology, a branch of mathematical image analysis, originated from the work of Georges Matheron[**?**] and Jean Serra[**?**] in the 1960s. They developed this theory to analyze and describe the geometrical structures present in images. Mathematical Morphology (MM) belongs to the category of non-linear processing, where the traditional addition and multiplication operations are substituted with the infimum ($\bigwedge$) and supremum ($\bigvee$) operators. Jean Serra's significant contributions to mathematical morphology include the development of fundamental operators such as erosion and dilation, which are used to extract information about the shapes and structures in a binary image. He introduced the concept of Structuring Elements (SE), which are small patterns or shapes used in the erosion and dilation processes [**?**]. The SE defines the pixel neighborhood for erosion and dilation, similar to a convolution kernel. It determines the influence of surrounding pixels on a pixel, aligned with the origin of the SE, during dilation or erosion. In binary, a structuring element is considered flat as it can only have a single value as in figure **??** where -Inf indicates positions to be discarded.

-Inf	1	-Inf
1	1	1
-Inf	1	-Inf

(a) A flat SE used in binary, grayscale or multivariate MM operations.

-Inf	$b_{ij} \in [0, 2^{n-1}]$	-Inf
$b_{ij} \in [0, 2^{n-1}]$	$b_{ij} \in [0, 2^{n-1}]$	$b_{ij} \in [0, 2^{n-1}]$
-Inf	$b_{ij} \in [0, 2^{n-1}]$	-Inf

(b) A non-flat SE used in grayscale MM operations.

Figure 9: The Structuring Element (SE) is used as the convolution kernel in Mathematical Morphology operations. It defines the pixel neighborhood during an MM operation. Positions with a value of -Inf in the SE are discarded.

The erosion and dilation are MM operators used to modify the shape or size of binary objects in an image. Erosion removes pixels from the boundaries of objects, making them smaller, while dilation adds pixels to the boundaries, making objects larger. The structuring element defines the shape and size of the neighborhood considered during the operation. By sliding the structuring element over the image, each pixel in the image is compared to the corresponding pixel in the structuring element. The erosion operation retains only the pixels in the image that match the structuring element, while the dilation operation adds pixels whenever there's a match in the surrounding of a pixel (Figure **??**). *More on these operator's properties in the annex B.* The mathematical expressions of these operators are as follows:

Binary Erosion:

$$\varepsilon_b(I, B) = \bigwedge_{(i,j)\in D_B} I(x+i, y+j)$$

Binary Dilation:

$$\delta_b(I, B) = \bigvee_{(i,j)\in D_B} I(x+i, y+j)$$

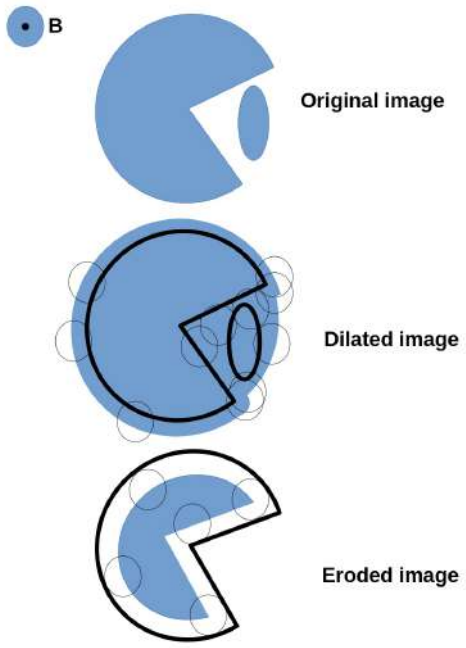

Figure 10: Binary erosion and dilation. B represents the Structuring Element (SE) used for erosion and dilation at each point of the image. The center of B is the origin of the SE, where the operation is applied. Empty circles on dilated and eroded images indicate some positions where the SE was slid during the erosion/dilation iteration. In the dilated and eroded image, the black lines indicate the contours of the original image.

We desire to count specific templates in the ganglion images: the neurons. The hit-or-miss transformation allows the detection of specific shapes in the images. It was firstly developed by G. Matheron and J. Serra for binary images [**?**].

Hit-or-Miss

$$\eta_b(I, g', g'') = \varepsilon_b(I, g') \cap \delta_b(I^c, g'')$$

3.2 MM Extension to grayscale

The extension of MM operators to grayscale was described by Soille and Serra in [?]. Whilst a flat SE is possible as shown in Figure **??**, depending on the characteristics of the object to be processed, where the SE contains a single value. In grayscale MM, a non-flat SE is defined where the values belong to the domain $D_B = \left[0, 2^{N-1}\right] \cup -\infty$ as illustrated in figure **??**. These values inside the non-flat SE determine an offset during erosion or dilation, as seen in the following mathematical expressions of the operators:

Grayscale Erosion

$$\varepsilon_g(I, B) = \bigwedge_{(i,j)\in D_B} \{I(x+i, y+j) - B(i, j)\}$$

Grayscale Dilation

$$\delta_g(I, B) = \bigvee_{(i,j)\in D_B} \{I(x+i, y+j) + B(i, j)\}$$

As shown in Figure **??**, the non-flat SE can be imagined as a 3D object with the height (or the third dimension) defining the offset during an erosion or dilation.

(a) Cross non-flat SE. Non-flat SE shapes to be used in grayscale or multivariate MM operations. More of these non-flat SE shapes in the annex.

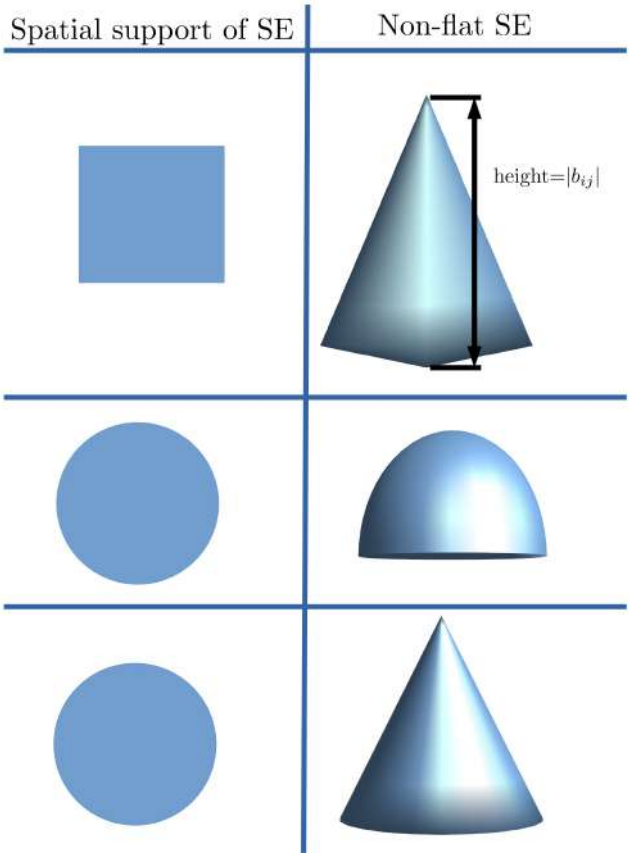

(b) Non-flat SE shapes (pyramid, semi-sphere, cone) to be used in grayscale or multivariate MM operations.

Figure 11: Different non-flat SE shapes for use in grayscale or multivariate MM operations.

The operations involve sliding the structuring element (SE) over the image and calculating the minimum (erosion) or maximum (dilation) values within the neighborhood defined by the SE after applying the offset. An erosion might result in negative values, and a dilation might result in values exceeding the maximum value as illustrated in figure **??**. Although not interpretable, these numerical results are valid and essential for various morphological image processing applications.

Figure 12: Erosion and dilation in grayscale can result in negative and values beyond original image extremal values.

3.2.1 Extension of Hit or Miss to grayscale: MOMP

The extension of the Hit or Miss transformation to grayscale is not straightforward. However, C. Barat proposed a solution called MOMP (Multiple Object Matching using Probing) [**?**], which is applicable to real-life pattern detection applications, such as ours. MOMP allows for the definition of both superior and inferior structuring elements, as illustrated in Figure **??**. At each position in the image, the two templates are probed to check if the signal falls within the templates range of shape and value. This approach enables the detection of templates even in the presence of noise or variations in size and shape.

MOMP

$$MOMP(I, g', g") = \begin{cases} 1, & \text{if } \delta_g(I, (-g'')^r) - \varepsilon_g(I, g') < \tau \\ 0, & \text{otherwise} \end{cases}$$

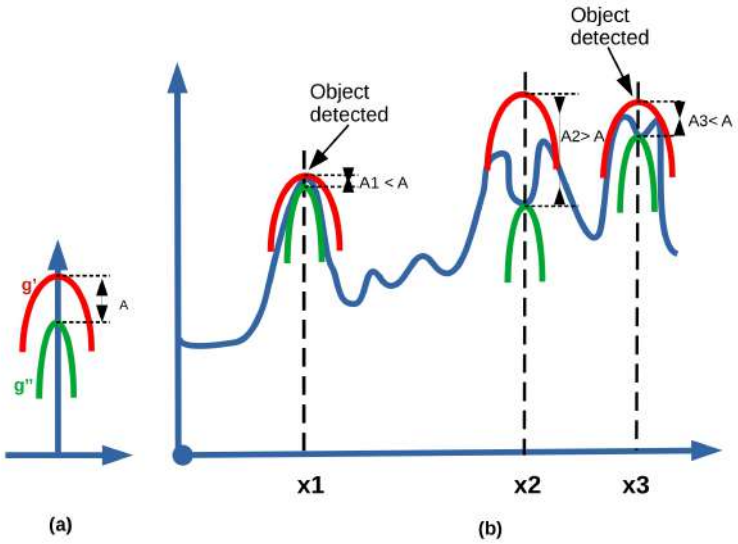

Figure 13: MOMP probing concept: Both templates are probed for every point of the signal. (a) Inferior and superior SE. (b) Two detections at positions x1 and x3.

By defining the maximum and minimum spatial support and the maximum and minimum contrast difference for these structuring elements, MOMP enables the identification of specific templates in the image, allowing for defined contrast and shape variations as shown in the figure **??**.

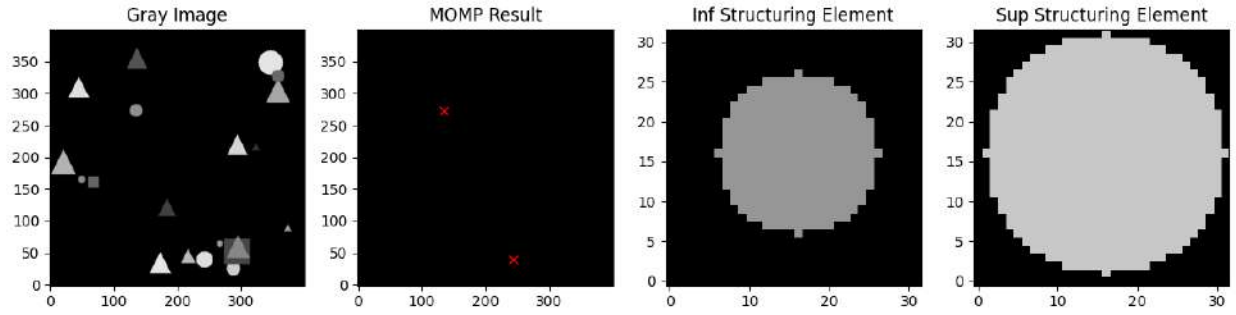

Figure 14: MOMP was applied to a grayscale image in order to detect round shapes with radii between 10 and 15 pixels, and pixel values between 100 and 150 on the grayscale intensity scale. The result plot of the MOMP shows the positions of detections (represented as red crosses), where the shapes fall within the specified range of sizes and the pixel values within the specified range.

MOMP appears to be a suitable operation for our application of counting neurons since the latter exhibit contrast and shape variations, as shown in Figure **??**.

3.3 MM extension to multivariate

Whilst the extension from 2d to 3d is natural as we're dealing with vectors. The extension to multivariate, or multichannel, such as color or multispectral images is not straightforward. Defining erosion and dilation in a multivariate space necessitates the introduction of addition operators ($+_c$ or $+_m$) and subtraction operators ($-_c$ or $-_m$), along with the establishment of an ordering to determine the minimum and maximum values in a multivariate context.

3.3.1 From grayscaly to multivariate

Addition and subtraction operations imply vectorial displacements in 1D, with specific amplitudes towards $+\infty$ and $-\infty$, respectively. Ledoux's PhD research [**?**] on extending MM to color images introduced the concept of these operators as vectorial displacements in the CIE lab space, aimed at convergence points. In the context of integer addition or subtraction, these convergence points inherently align with $+\infty$ and $-\infty$, respectively. Eroding an image infinitely(with a non-flat SE),or at least a sufficient number of iterations will result in an image whose values converge towards $-\infty$. Dilating an image infinitely(with a non-flat SE) will result in an image whose values converge toward $+\infty$.
In multidimensional space Ledoux proposes to define convergence points which would be the convergence points of infinite iterations of erosion or dilation [**?**]. The concept of the displacement in multivariate space towards convergence points is depicted in the figure **??**. The choice of these convergence points depends on the specific application. O^+ designates foreground coordinates, while O^- refers to background coordinates. Dilation expands regions with values near the foreground, and erosion does the same for regions close to the background. In the multivariate context, the structuring element (SE) defines the amplitude of vector displacement toward a convergence point during erosion or dilation operations. In the following, figure **??**, the construction of a non-flat multivariate SE. The NaN(Not a number) is introduced to prevent confusion with the convergence point O^+.

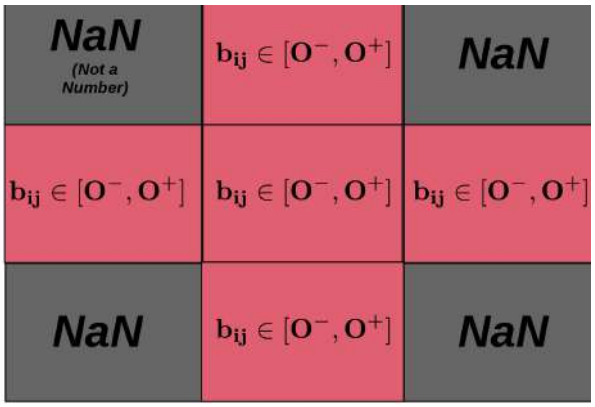

Figure 15: Multivariate non-flat SE. $b_{ij} \in \mathbb{R}^n$.

The mathematical expression for vectorial displacement, as depicted in figure **??**:
Displacement of point C towards O^-

$$\overrightarrow{D_i} = \overrightarrow{CO^-}$$

$$\text{Direction of displacement: } \overrightarrow{d_i} = \frac{\overrightarrow{D_i}}{\|\overrightarrow{D_i}\|}$$

$$\text{Displacement magnitude: } \alpha = \|b_{ij}\|$$

$$\text{Displaced color coordinate: } \overrightarrow{O^-C_i'} = \overrightarrow{O^-C_i} + \alpha \cdot \overrightarrow{d_i}$$

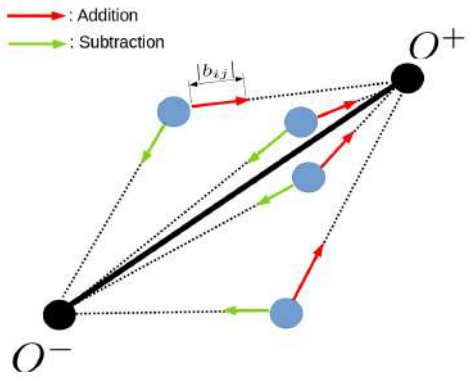

Figure 16: Multivariate coordinate displacement concept associated with the notion of convergence. The amplitude of an addition or subtraction is equal to the norm of the coordinates of the corresponding non-flat SE value.

The convergence points will serve to define a multivariate displacement. Nevertheless it will also serve to define the ordering between multivariate coordinates. As described in ledoux's thesis [**?**], the minimum is the closest to O^- and the maximum is the closest to O^+. Ledoux's work focused on the extension of MM to color images and chose to define the color coordinates and the convergence points in **CIE lab** space as its a perceptual space where variations in color are proportional to human perception of color variation and because the $\Delta E$is a valid distance in this space that reflects this perceptual variation.
Color ordering

$$C_i \prec_c C_j \iff \Delta E(C_i, O_2^-) < \Delta E(C_i, O_2^-)$$

$$C_i \succ_c C_j \iff \Delta E(C_i, O_2^+) < \Delta E(C_i, O_2^+)$$

3.3.2 Adaptation to the Mice Heart Images

The adaptation of MM to the multivariate case involves combining distance functions within a multivariate domain. Audrey Ledoux chose to operate within the CIELAB color space to employ a perceptually uniform Euclidean metric, directly related to human color perception. Hilda Deborahs, on the other hand, ventured into multivariate mathematical morphology within hyperspectral spaces, utilizing an adapted spectral similarity measure known as KLPD[?]. This approach, rooted in the spectral domain, provides a closer alignment with the physical world.
Given that the Preti experts define the ground truth based on the color representation of acquired RGB images for Ganglia, **we opted to utilize the CIELAB space to better reflect their expertise. This decision is not a limitation but rather a strategic choice for preliminary results. It remains flexible and subject to modification as needed.**

3.3.3 Refined Approach: Adapted MMOMP (Multivariate MOMP)

While Audrey Ledoux initially developed the CMOMP transforms through a combination of ordering functions, Rania Goutali's work in [?] revealed that the proposed ordering construction did not uphold the necessary idempotency property for the opening and closing transforms. To address this limitation, Hilda Deborah proposed an ordering function based on vector angles in [?]. **In the context of this project, we intend to integrate Hilda Deborah's ordering approach into the CMOMP function originally defined by Audrey Ledoux.** This ordering employs two references separately for minimum and maximum extraction. Which means that the local minima found using the $\prec_c$ is different than that found using the $\succ_c$.

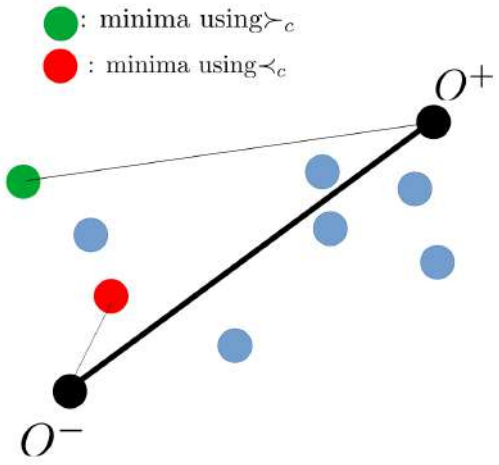

Figure 17: Different local minima preventing the idempotence property of morphological operators (where idempotence means that applying the operator multiple times to an image produces the same result as applying it once).

For this reason we will choose to build the multivariate morphological operators using CRA(conditional ration and angular ratio of distance) ordering developed during Deborah's thesis[?].
CRA ordering:

$$g^-(C_i) = \frac{\Delta E(C_i, O^+)}{\Delta E(C_i, O^-)}, \quad g^+(C_i) = \frac{\Delta E(C_i, O^-)}{\Delta E(C_i, O^+)}, \quad g_A(C_i) = 2 \cdot \frac{\Delta E(C_i, O^-)}{\Delta E(O^-, O^+)}$$

$$C_i \prec_{CRA} C_j \iff \begin{cases} g^-(C_i) > g^-(C_j), & \text{or} \\ (g^-(C_i) = g^-(C_j) \text{ and } g_A(C_i) < g_A(C_j)) \end{cases}$$

$$C_i \succ_{CRA} C_j \iff \begin{cases} g^+(C_i) > g^+(C_j), & \text{or} \\ (g^+(C_i) = g^+(C_j) \text{ and } g_A(C_i) > g_A(C_j)) \end{cases}$$

The concept of CRA ordering is illustrated in the following figure **??**.

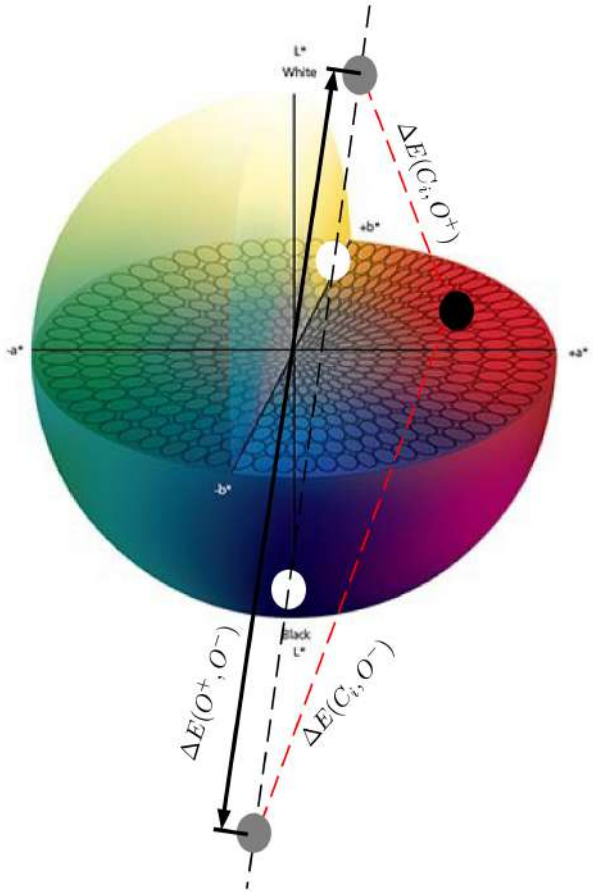

Figure 18: CRA ordering concept in CIE lab color space. Initial convergence points are in white which are extended(in grey) before performing the ordering of the considered point(in black) according to the two extended convergence points.

With the CRA ordering minima and maxima are determined by the ratio of distance to the two convergence points. Thus allowing to construct MM operators that verify idempotency and duality which is necessary to perfom non-linear or Morphological filters and will be essential for us to validate our operators by testing these properties.

3.3.4 Behavior of MM Operators at Convergence Points

After a number of dilations and erosions iterations the coordinates might reach the convergence points. A question we aimed to solve is: How should the MM operators behave when a coordinate reaches a convergence point? As this question was not previously studied, we explored it to define the adapted behavior of Mathematical Morphology (MM) for our study.
It is important to prevent divergence and ensure convergence when a dilated coordinate value reaches a convergence point as in the figure **??**. The reason behind this decision is that if the coordinates diverges then the dilated coordinates loose their numerical meaning and interpretability.

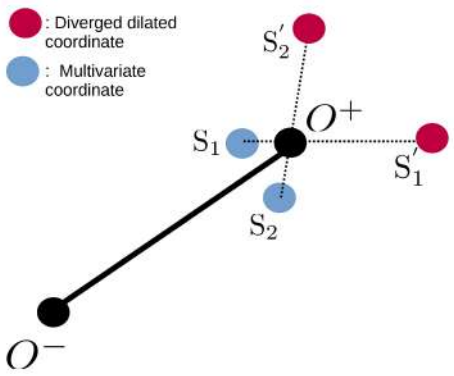

Figure 19: Divergence of the multivariate coordinate displacement after iterations of dilation or erosion.

Due to the non-uniformity in shapes sizes and histogram of values in granulometric analysis the velocity of convergence is not uniform. One problem when ensuring the divergence might be the saturation of the displaced coordinates at the convergence coordinates as in the following figure **??**. Saturation is achieved after one iteration of dilation and thus Sup and $Sup[-1]$ will no longer be differentiable after this iteration.

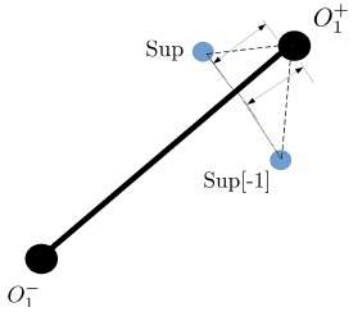

Figure 20: Saturation of coordinates after one iteration of dilation. "Sup" is the closest point to O_1^+, and "Sup[-1]" is the second closest. After a single iteration of dilation, both points will coincide with O_1^+.

However as mentioned in [**?**], the erosion and dilation are to be increasing and dual operators. The convergence points needs to be chosen far enough from the points distribution to prevent saturation and preserve ordering relation. The figure **??** illustrates the concept of convergence point extension to prevent saturation and loss of order. The extension of convergence points follows the following formula where same to be applied for O_1^-:

$$\text{if } \|\overrightarrow{SupO_1^+}\| < \|b_{ij}\|. \tag{1}$$

Place the new convergence point: O_2^+ such as:

$$\overrightarrow{O_2^+O_1^+} = K \cdot \overrightarrow{SupO_1^+} \cdot \overrightarrow{O_1^-O_1^+} \tag{2}$$

It is important to emphasize that the size of the structuring element or the number of processing iterations is predetermined or defined prior to image analysis. Therefore, the value of K can be readily established based on factors such as image size, image processing parameters, or human interaction.

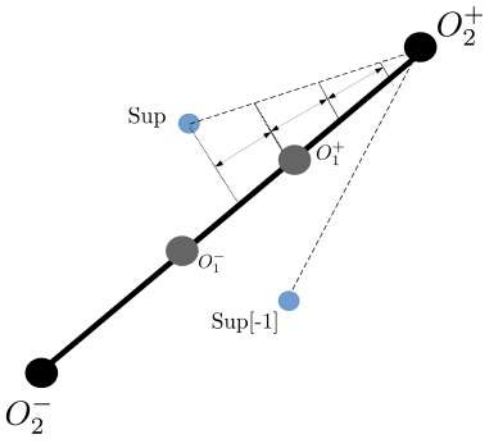

Figure 21: Saturation prevention by extending the convergence points. Initial convergence points in grey. Extended convergence points in black. The number of iterations before saturation of local maxima is 4 (K=4).

3.3.5 Proposed MMOMP algorithm

Once we have established the definitions of $+_c$ and $-_c$, as well as how to order multivariate coordinates in the multivariate space, we can define the MM operators in multivariate space and proceed to define multivariate MOMP (MMOMP). Refer to Figure **??** for the steps involved in applying CMOMP and its concept. Following are the mathematical expressions involved for the color expression: **Color Erosion**

$$\varepsilon_c(I,B) = \bigwedge_{\substack{CRA \\ (i,j)\in D_B}} \{I(x+i,y+j) -_c B(i,j)\}$$

Color Dilation

$$\delta_c(I,B) = \bigvee_{\substack{CRA \\ (i,j)\in D_B}} \{I(x+i,y+j) +_c B(i,j)\}$$

MMOMP

$$MMOMP(I,g',g") = \begin{cases} 1, & \text{if } d(\delta_c(I,(-g'')^r),\varepsilon_c(I,g')) < \tau \\ 0 & \text{otherwise} \end{cases}$$

In the context of CIELAB application, the function d(,) is established as the Euclidean distance between color coordinates within the CIELAB color space, effectively defining the perceptual distance (ΔE metric). For applications in the spectral domain, where the preservation of metrological constraints is crucial, a KLPD similarity metric can be employed. The L2 metric find use under specific assumptions and dedicated validation. **The decision has been made, as previously justified, to utilize the ΔE metric (L2) within the CIELAB color space for the intended applications**. This choice aims to yield results that closely align with Expert judgments.

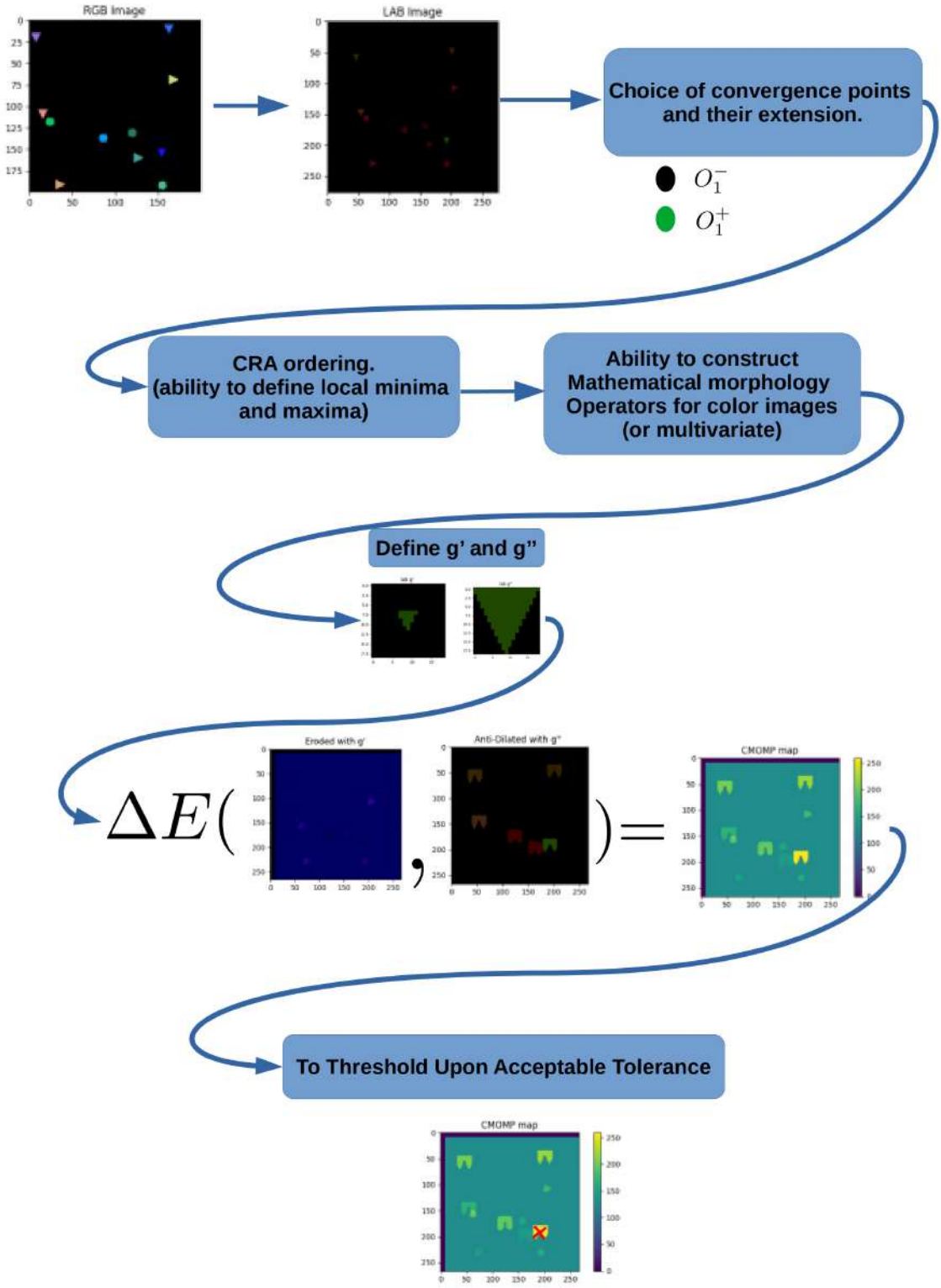

Figure 22: CMOMP concept and the block diagram that shows the steps to apply Mathematical morphology on a multivariate image.

Choice of CMOMP threshold depends on distance between convergence points and allowed tolerance of color(in the lab space) and shape.

$$Threshold = f(d(\text{background}, \text{target}), \text{shape}) \tag{3}$$

The following Figure ?? shows CMOMP probing applied to a color image where all discs have the same shape, but different RGB coordinates. The intended validation process will detect discs that possess a color content falling within the specified templates (SE inf and SE sup), thereby conforming to colors within the range defined by the threshold. The first line displays variations in the blue coordinate, the second line shows variations in the red coordinate, and the last line shows green variation. However, the detection depends on the contrast in the CIE Lab color space. The threshold was manually chosen to be $\Delta E(O_2^+, O_2^-)/39$. This was a manual empirical choice that is consistent with Equation ??, as the convergence points are chosen based on the background and foreground colors(blue color of the first disk on the 2^{nd} line).

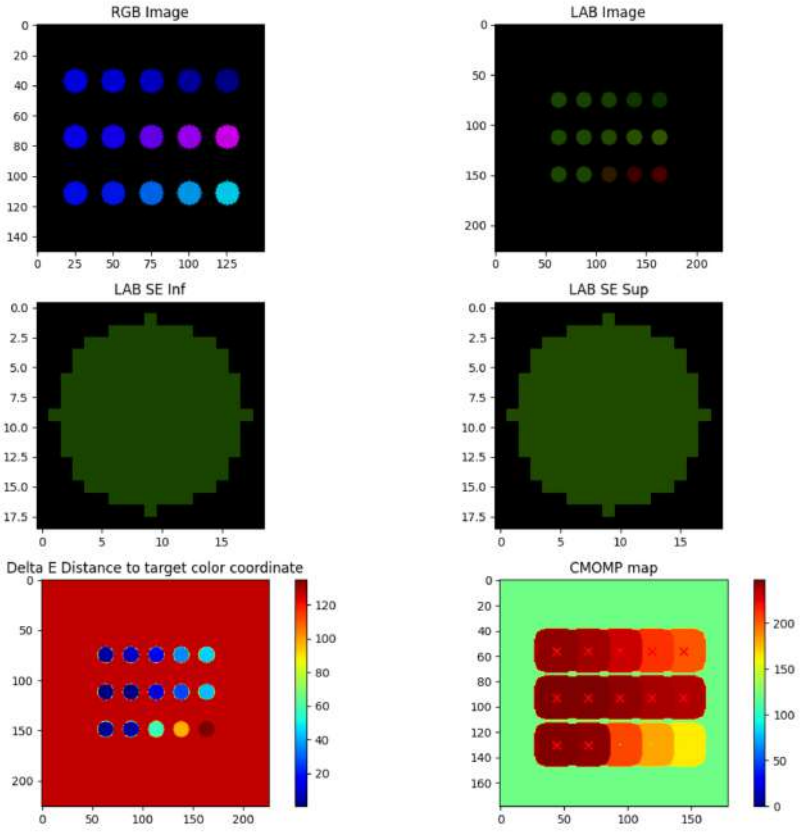

Figure 23: CMOMP applied to a figure with identical shapes and color variations. Both SEs have the same size, with their color being higher and lower than the target color, which corresponds to the first circle in the second line from the right. The red crosses on the CMOMP plot indicate the positions of detection. The threshold is manually set to $\Delta E(O_2^+, O_2^-)/39$. The convergence points are initially set to black (O^-) and the target color coordinate (O^+) before extension.

The following Figure ?? demonstrates tolerance to shape and size variations. We observed a high sensitivity to shape differences, and whenever the size exceeds the range of the structuring element (SE) sizes, the CMOMP values become much higher. Therefore, the threshold choice is more constrained to contrast variation.

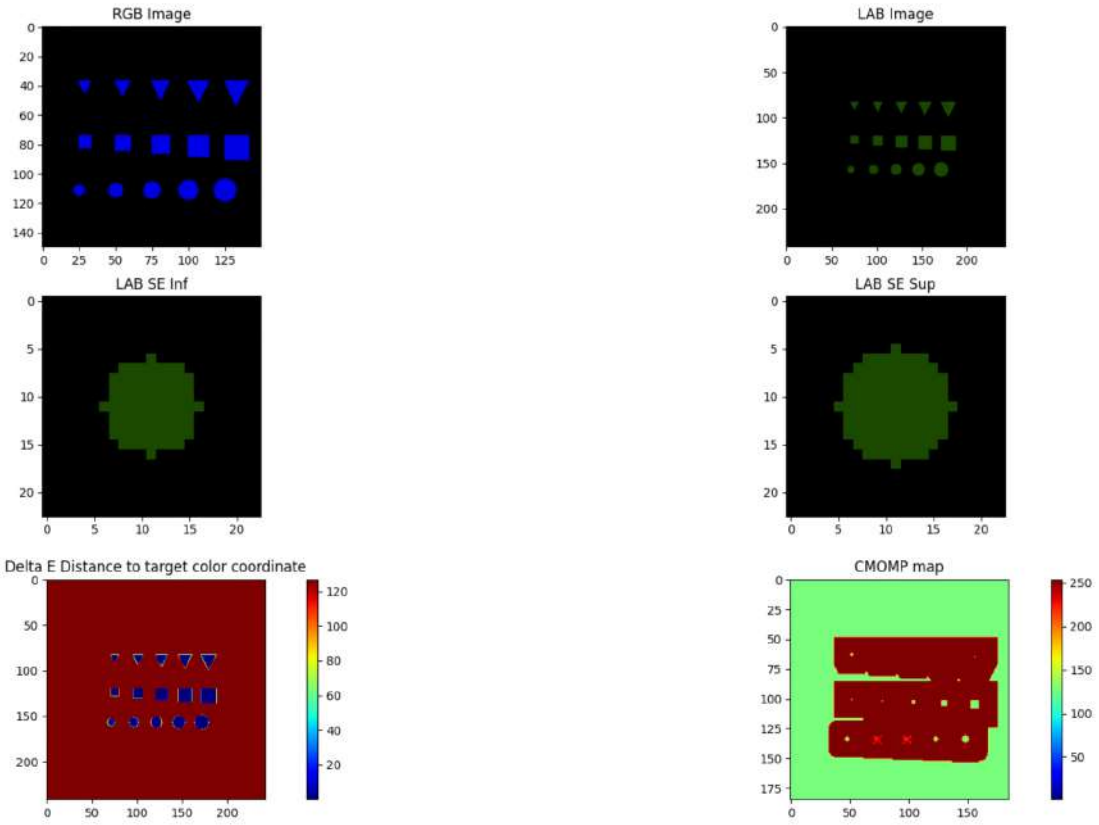

Figure 24: CMOMP applied to a figure with different shapes and sizes but the same colors. The SEs have the same color as all the objects in the figure. The sizes of the SEs fall between that of the 2nd and 3rd circles from the right. Red crosses indicate the positions of detection where the CMOMP value is below the manually set threshold. The convergence points are initially set to black (O^-) and the target color coordinate (O^+) before extension.

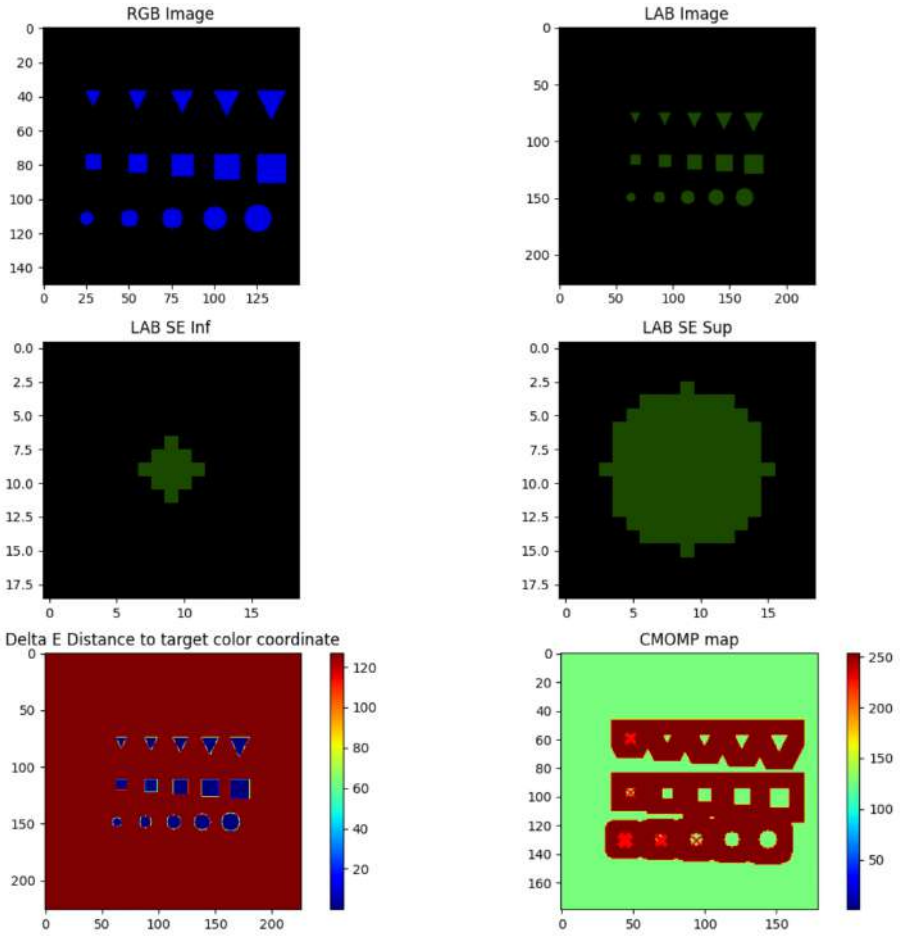

Figure 25: CMOMP was applied to a figure containing objects of different shapes and sizes but the same colors. The difference in structuring element size includes objects of various shapes. The red crosses indicate the positions of detection where the CMOMP value is below the threshold. This figure shows that if an object, regardless of its shape, is inside the shape margin defined by the SE inf and sup, it is detected.

Note that the background of the probes can be used in the shape and color specification of the target object to detect shapes of a specific color with specific backgrounds. This capability allows for the identification of objects based on both their color and the context in which they appear **??**. (please review the code in the GitLab repository for figures with enhanced contrast.)

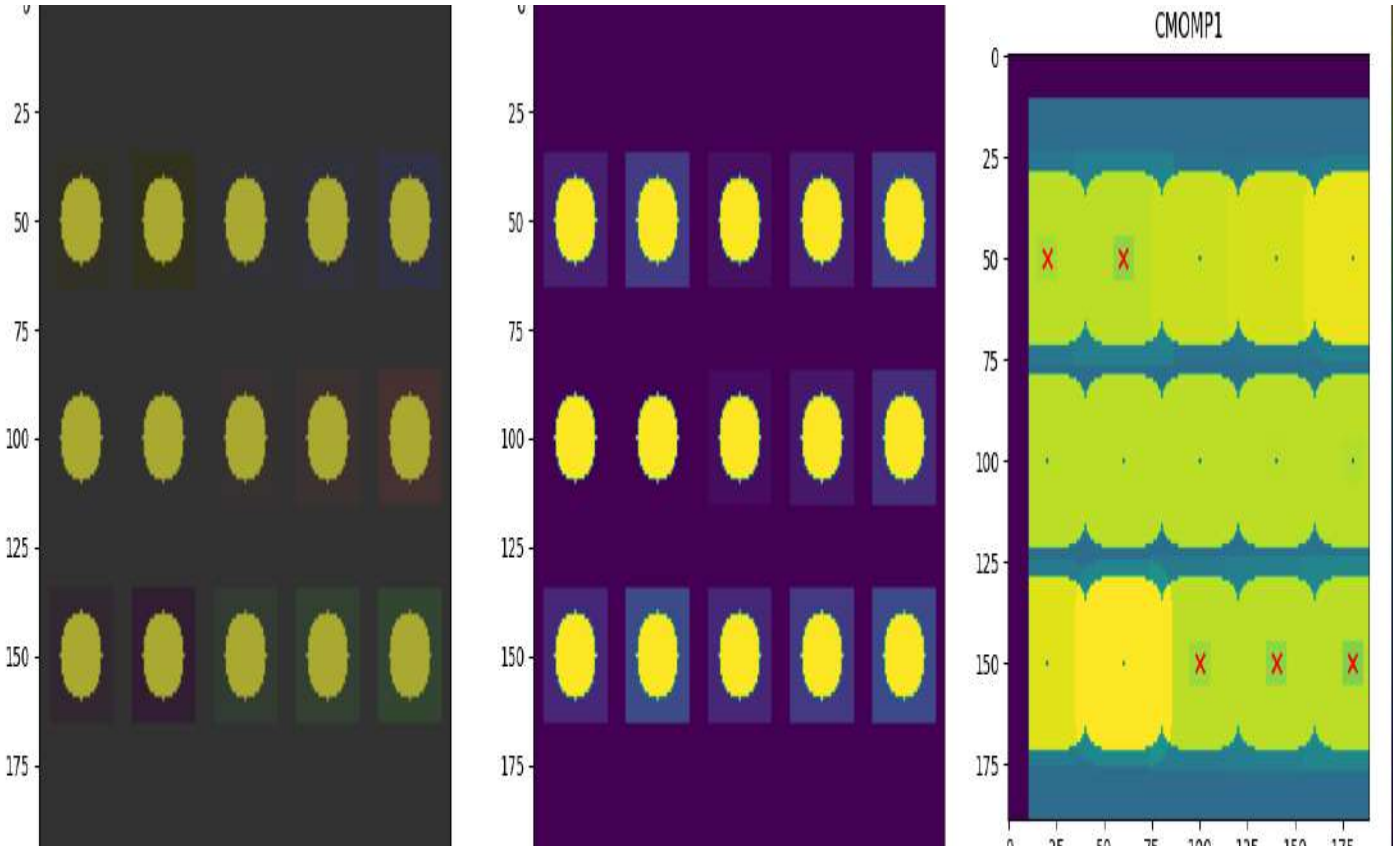

Figure 26: CMOMP applied to a figure with identical shapes of different backgrounds.

The below figure **??** shows the impact of adding noise to the image. We noticed that only slight changes in the background were sufficient to alter the expected results. Only a single detection was left from the previous image upon adding noise. Thus revealing the necessity of pre-treatment and filtering.

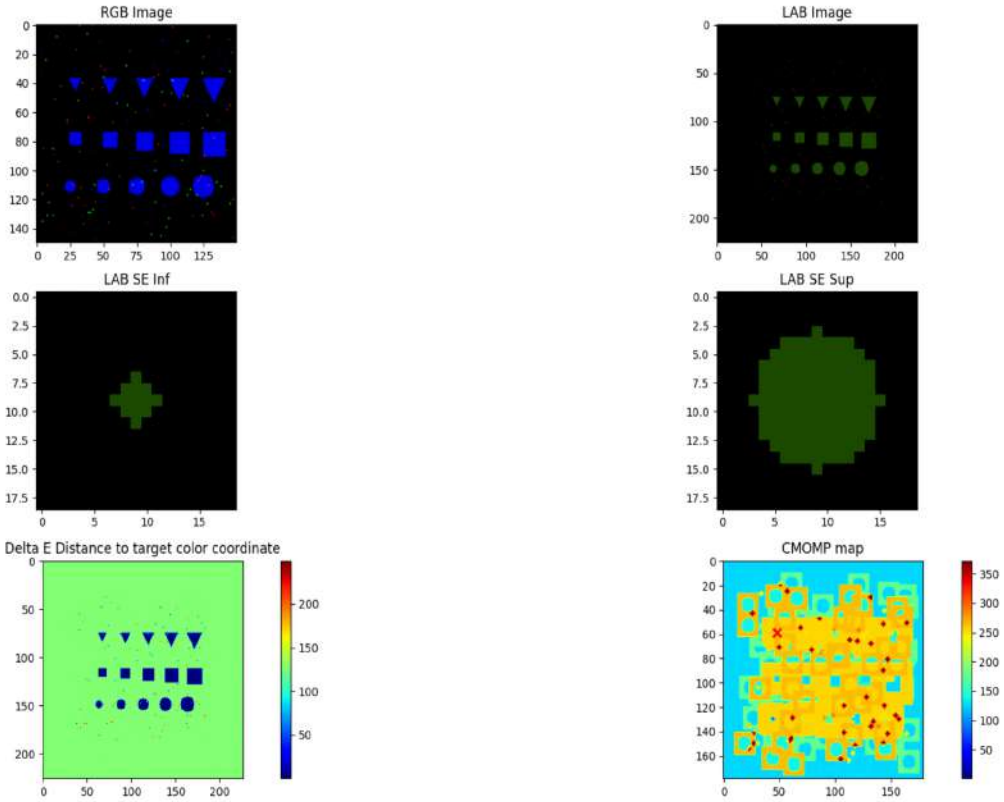

Figure 27: CMOMP applied to a figure with additive Gaussian noise of std=0.35 and mean of 0 on the three channels. Detection is interrupted due to the noise sensitivity.

Due to this sensitivity of MMOMP to noise in the next section, we will analyze the mice heart images and apply some pre-treatments. Neurons often exhibit a non-uniform arrangement in the form of disk-like shapes. To capture this distinctive morphology, our goal is to employ a filtering technique that can generate images with consistently uniform disk-like structures.

Contributions

- Proposition of a new Multivariate MOMP:
  - Developed based on Ledoux's original construction.
  - Incorporates the ordering approach proposed by Hilda Deborah, ensuring the fulfillment of the idempotency property.
  - Introduces a study and proposition for effectively managing convergence coordinates in cases involving non-flat structuring elements.
- Implementation and illustration in the color space using RGB images, employing the perceptual distance metric (CIELAB ΔE).
- Suggested an approach for neuron extraction utilizing the color version (CMOMP) to align with expert ground truth. This choice primarily impacts preprocessing (color transform) and the distance metric used in the ordering.

4 Analysis & Pretreatment of images

In the preceding section, we observed the **sensitivity of the CMOMP implementation** to image noise. Additionally, it's worth noting that the morphological approach was chosen following two months of exploring learning-based solutions and conducting statistical analysis. These analysis revealed significant variability in antibody responses, lack of homogeneity within the region of interest across different slices, and even within the same slice.

Given these findings, our next step, before delving into the implementation of the CMOMP on **mice heart images**, will involve a study of these variabilities. Subsequently, we will propose filtering approaches aimed at enabling successful CMOMP transforms.

4.1 Analysis and observations

Initially, Préti had acquisitions of heart immunolabelled with TH and ChAT antibodies (1st acquisition series). However, since the response of one of the channels was too noisy and blurred, they decided to start new acquisitions using PGP and Th antibodies instead (2nd acquisition series), which was unfortunately not successful. Therefore, most of the observations are based on images acquired using TH and ChAT, and these observations are planned to be repeated once acquisition problems are resolved.

As shown in figure **??**, ganglia comes in different shapes and sizes. It can be noticed that in these ganglia images we can not manually count the neurons(disks in red, green or yellow) which is the reason they decided to change the ChAT marker with PGP to experiment if it has different response to the laser excitation that enables us to identify clearly the neurons.

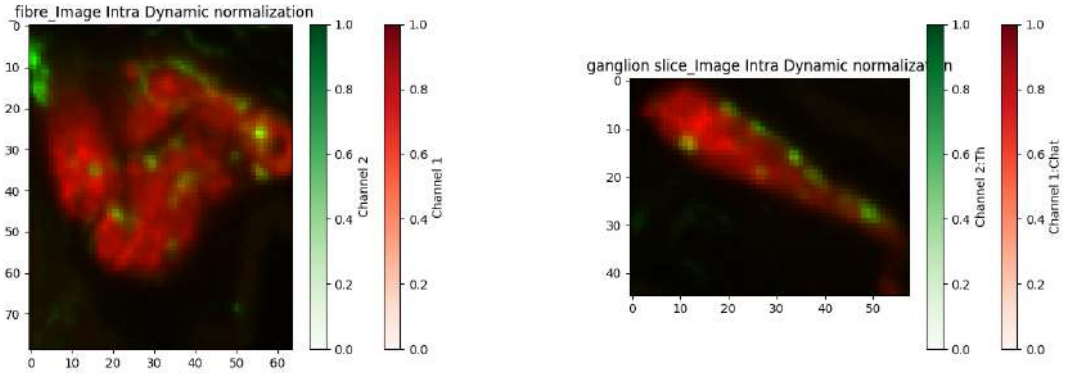

(a) Ganglion 1.

(b) Ganglion 2.

Figure 28: Images(2D Z slices) of two different ganglia labeled with TH(red) and ChAT(green) markers.

As in any image acquisitions **noise** has many sources. Some are from the sensor itself and the from the scene. Some of the noises we observed were due to the miscalleneous response of the marker sometimes cause its old and expired so it forms some aggregas as in figure **??**, or the heart was not properly cleared so traces of the markers will stay in the heart even if not attached to a neurone such as the red dots in **??**. One other source of scene related noise is auto-fluorescence, actually even if not immunolabelled when excited with a laser beam a tissue will respond by emmitting some fluorescence.

In the following pages, we will analyze the image content and values. In a light sheet acquisition process, the laser intensity is not uniform on a slice (2D horizontal plane), leading to variabilities in fluorescence emission and pixel intensity of a given channel. The heart's partial opacity also introduces variabilities in photon transmission. Furthermore, it's important to note that there is no applied calibration process for image acquisition. Consequently, a visual assessment is conducted for each heart to select acquisition parameters (exposure time, channel gain, light sheet parameters) based on an empirically chosen region containing neurons. This has resulted in significant differences in average and range values across different acquisitions.

To better comprehend these variabilities, we conducted a statistical study. This study guided the development of filtering approaches for Ganglia and Neuron Detection in 3D Multivariate Cardiac Nervous

System Images, which were applied before performing CMOMP operations.

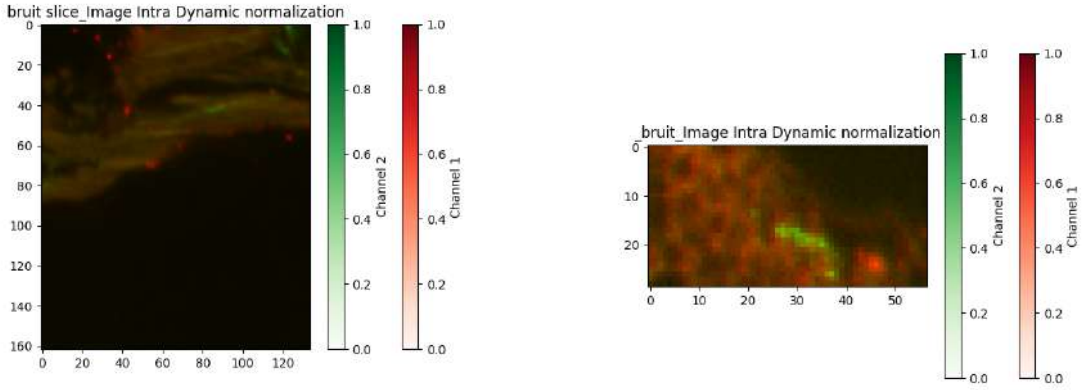

(a) Autofluorescence and miscellaneous marker response(red dots).

(b) Autofluorescence.

Figure 29: Images(2D Z slices) of two noise zones. (ChAT and TH markers).

We observed the values distributions in different zones and pixels classified as noise, fiber or ganglia. In table ?? the boxplots of both channels voxel values of crops of ganglions, fibers and noise can be observed. These boxplots show that these crops have similar distribution not exceeding the range of 10000 for both channels. This is why in the following figures, the value range is reduced to the range of [0,10000] instead of [0, 65 535].

Table 3: Boxplots for volumes containing a specific class.[3]

	Ganglia	Fibre	Noise
Channel 1	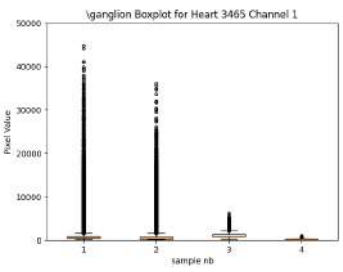	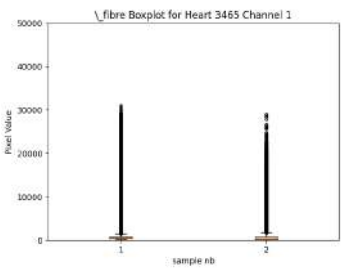	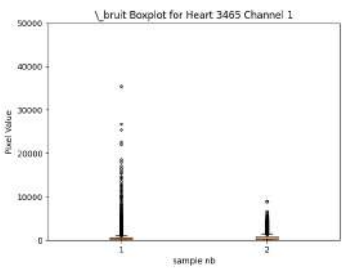
Channel 2	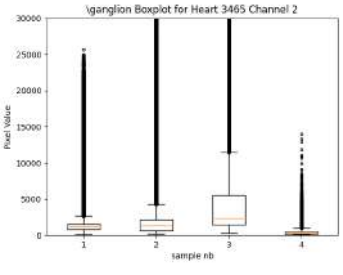	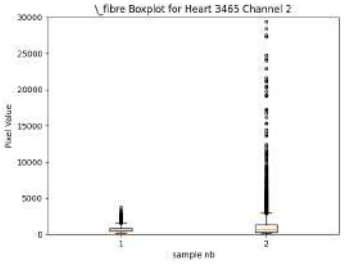	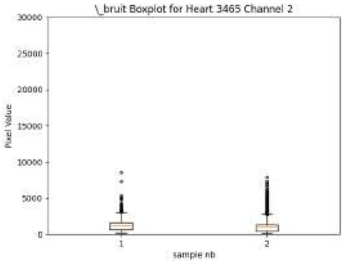

the ground-truth is established based on labeled 2D cropped zones. This approach introduces a level of uncertainty in identifying the elements of interest, such as ganglia and neurons. These labeled zones often contain a significant amount of noise and fiber, making accurate identification challenging. Conversely, the statistics of images without fiber and ganglia exhibit a narrower range of variation. Examining Table 3, we observe that the average values for ganglia tend to be higher than those for fiber and noise, particularly noticeable in channel 2. However, this tendency is somewhat counterbalanced by the data from sample 4. Furthermore, it's worth noting that noise and fiber information exhibit a high degree of correlation. This

[3]More boxplots from different hearts in the annex.

correlation adds an additional layer of complexity to the discrimination task.

Working on a channel-by-channel basis (marginal approach) overlooks a portion of the potential combination benefits. In a subsequent level of analysis, we are examining the joint probability of obtaining a specific pair of channel responses from the two antibodies. A histogram illustrates the joint probability of a value range pair for both channels of a voxel in a specific volume. Figure ?? illustrates how to interpret these histograms.

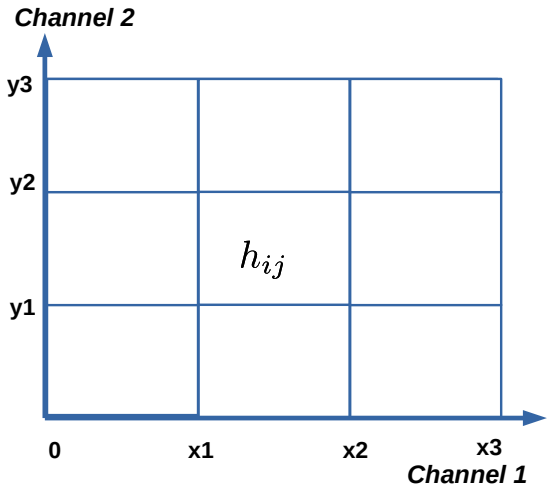

Figure 30: Reading an image histogram. The position value expresses the joint probability of $S(p)$ within a value range for both channels. $h_{ij} = \Pr\{x_1 \leq S(p) \leq x_2$ for channel 1, and $y_1 \leq S(p) \leq y_2$ for channel 2$\}$. The parameters that can be adapted in a histogram are the number of bins and bin ranges.

In Tables ?? and ??, we examine the value distributions within slices and volumes of mice heart images containing noise, fibers, or ganglia.

It's important to note that for the ICNS structure images, the channel intensities are normalized between their minimum and maximum values to enhance content perception. The green color corresponds to the Th antibody marking, while the red corresponds to the ChAT marking. To ensure comparability, all slice crops are of size 64x64, and volume crops are 64x64x64. The cropping center was specified by the expert.

For the first ganglia (first row in Table ??), the ganglia size is relatively small, with the majority of the crop accounting for background noise. This explains why the 2D histogram is concentrated on low channel values. The second and third rows depict ganglia histograms, one primarily exhibiting variations in green while the other in red.

Regarding the fiber crops, they are recognizable in the images by linear or tubular shapes. Their histograms, much like the noise, are highly concentrated at low values for both channels.

For Table ??, which considers volumes and not 2D slices from two different individuals (hearts). Volumes are classified by the expert as ganglia, noise, or fiber. For some ganglia, a main value is related to Th marker's response, whereas for others, they mainly show a low value distribution for both channels. For noise volumes, it is noticed that high values also exist for the green channel, reflecting mainly that an analysis based solely on statistics of values is not adequate for the classification of these crops.

Table 4: Observations of histograms Intra slices from multiple Mice hearts[4]

	Intra normalisation	histogram Intra Slice
ganglia 1	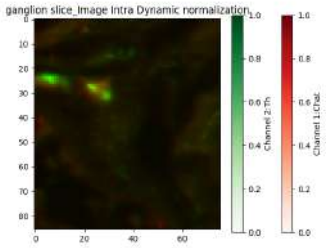	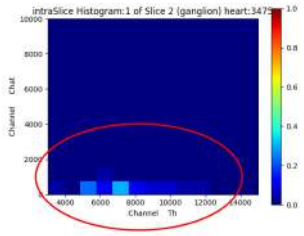
ganglia 2	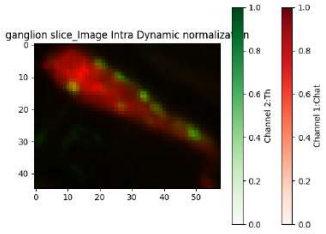	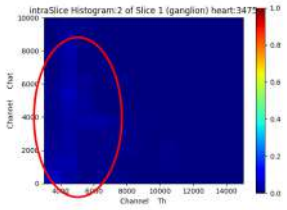
ganglia 3	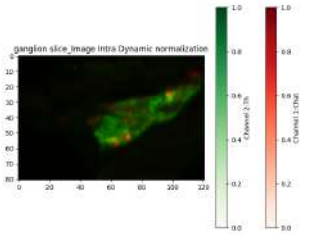	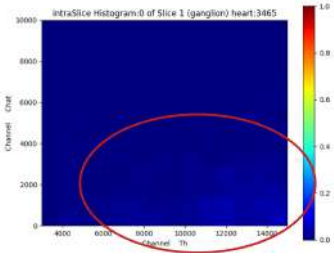
noise 1	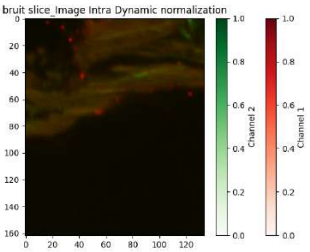	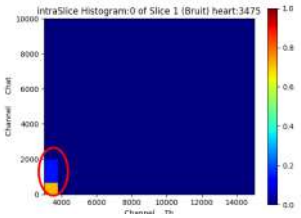
fibre 1	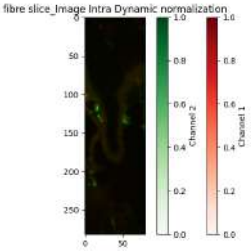	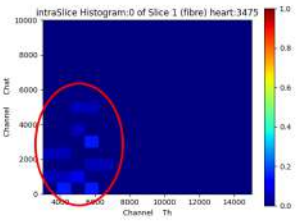
fibre 2	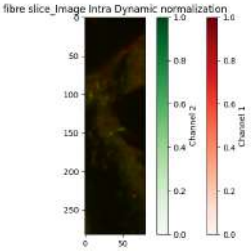	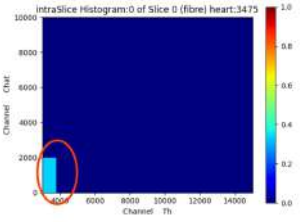

Table 5: Observations of histograms Intra VOI(Volume of Interest)

	Ganglia	Fibre	Noise
heart1	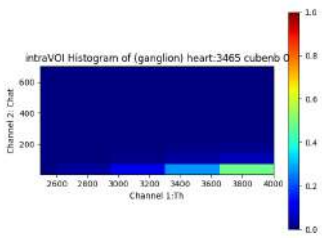	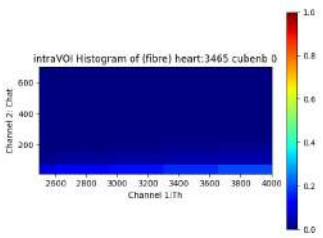	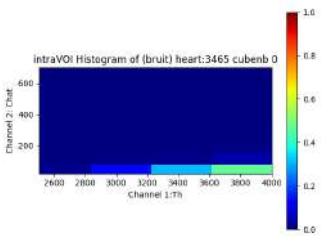
heart1	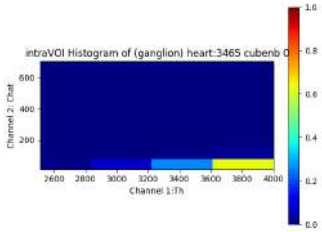	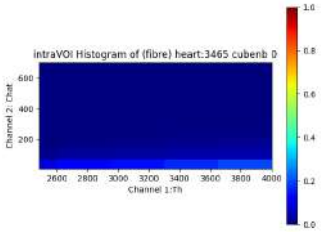	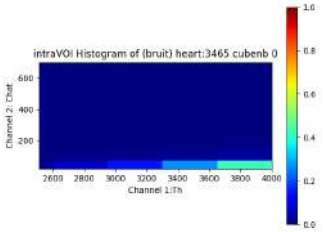
heart2	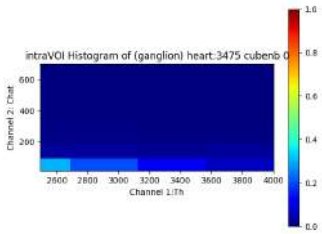	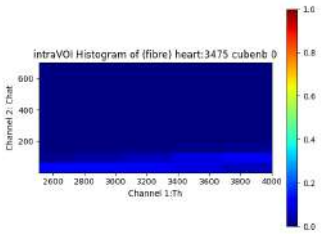	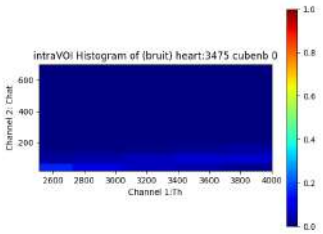
heart2	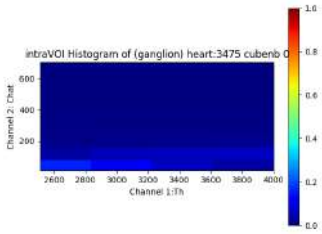	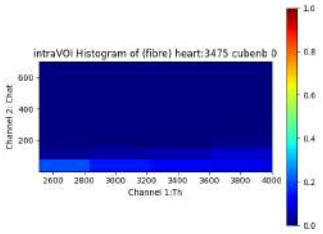	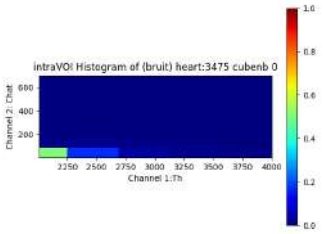

Table **??** shows that for the noise crops the values distribution over both channels is highly correlated, since both channels are captured at different times with different sensors this suggests that **the noise is linked to the scene**. when assisting one of the image acquisition sessions it was more clear as background auto-fluorescence from the sample, uneven staining of the tissue, default in the clearing protocol, air bulbs blocked inside the tissue can contribute to noise in the image and make it difficult to distinguish signal from noise.

Table 6: Correlation between channels for different heart components

Heart Component	Fibers	Ganglia	Noise
Whole Cropped Heart	0.40		
Heart 1	0.172	0.514	0.717
Heart 2	0.351	0.471	0.679

The problems faced concerning the acquisitions and the nature of the images will be discussed in the risk management section.

For the new acquisitions, we had a single sample image of a ganglion, which did not display any significant

evolution in the value distribution of measurements. In Figure **??**, we selected pixels from zones of the image that correspond to noise, fiber, and neurons, and observed the evolution of values in the Z direction. It is expected for neuron pixels or fibers to exhibit a peak value at a certain z-slice where the fluorophore exists and to decrease for higher slices. The persistent observation in this figure is that one of the channels does not provide valuable information that can be utilized to differentiate noise measurements.

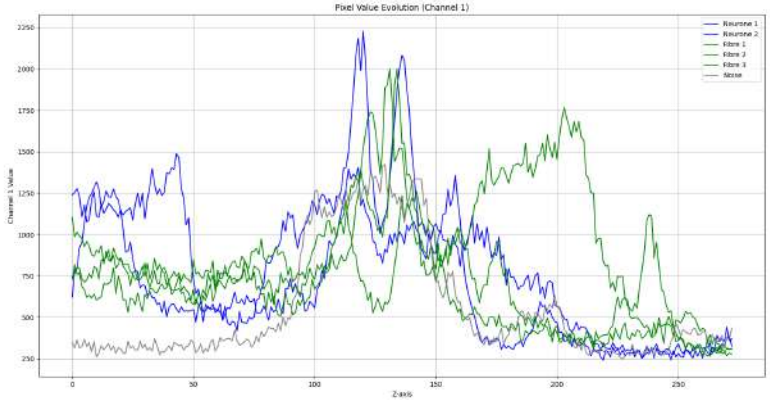

(a) Channel 1

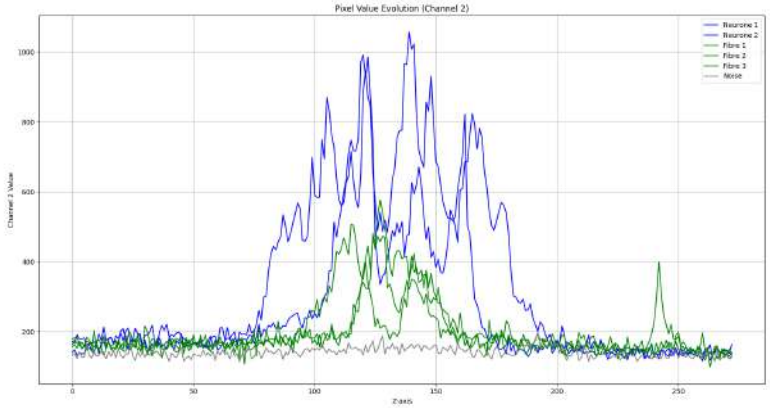

(b) Channel 2

Figure 31: Evolution of pixel values identified as neurons, noise, or fibers in the Z direction.

Neurons can be observed as a non-uniform assembly of disk-like shapes. In pursuit of this characteristic morphology, our objective is to implement a filtering technique capable of generating images with uniform disk-like structures. **To address this, we now turn our attention to the application of morphological filters.**

4.2 Morphological filtering

Nonlinear filtering of multivariate images involves operations like minimum, maximum, median, and MM operators. In contrast to the common marginal approach used in available libraries, our implementation adopts a vectorial approach and CRA ordering to process all channels simultaneously. This approach is crucial in multivariate image processing to prevent the introduction of "fake" colors or measurements, ensuring that the proposed correction remains faithful to the initial dataset. **Further details about the developed non-linear filtering based on CRA ordering, along with implementation results, can be found in the appendix. However, our current focus is directed towards Morphological filtering.**

Morphological filtering, a subtype of nonlinear filtering, is especially valuable for tasks such as noise reduction, edge detection, and feature extraction. **It aims to target specific shapes and contrast**.

Though slower due to the involvement of pixel ordering and convolutions, morphological filtering yields valuable results in image processing[?].

As explained in [?], algebraic opening is a morphological operation that combines two basic operations: erosion followed by dilation. It is used to remove small noise or small objects from the foreground of an image while preserving the overall shape and structure of larger objects. The process involves performing an erosion operation first, which reduces the size of the foreground objects and fills small gaps. Then, a dilation operation is applied, which expands the objects slightly. The expected result is that small, disconnected regions get eliminated while larger regions remain largely unchanged. Algebraic closing is another morphological operation that combines dilation followed by erosion. It is used to close small gaps in the foreground of a binary image while maintaining the general shape of the objects. The process involves performing a dilation operation first, which expands the size of the foreground objects and fills small gaps. Then, an erosion operation is applied, which reduces the objects' size slightly. The result is that small gaps between regions are closed, while the overall shape of the objects remains relatively unchanged.

Choosing the parameters of morphological filtering involves selecting the convergence points, which depends on the background and foreground colors of the target templates. The latter will influence the ordering of colors at each morphological iteration. Additionally, determining the size of the SE is based on the size of the objects to be filtered. Since neurons do not have a uniform size, this choice requires testing and image analysis, which will impact the number of iterations before convergence. The choice of filter type is also important; the more morphological operations are added, the more processing time will be required.

In table **??** (**??** and **??** in the annex), a number of morphological filters applied to the ganglia slice in fig **??**. The target object is the yellow one disk so the convergence points are set to be black for O^- and yellow for O^+. The open-close-open filter appears to offer a more uniform value and a disk or elliptical shape for the targeted neuron. This multivariate CRA-based filtering reveals that the yellow neurons become clearer, while the green disk-like neurons begin to fade out. Although the median filter is computationally less intensive, its effectiveness is limited by the persistent non-uniformity observed in the yellow neurons. This filtering approach aims to enhance the establishment of a model shape and color for neurons, rendering it more suitable for the application of MMOMP.

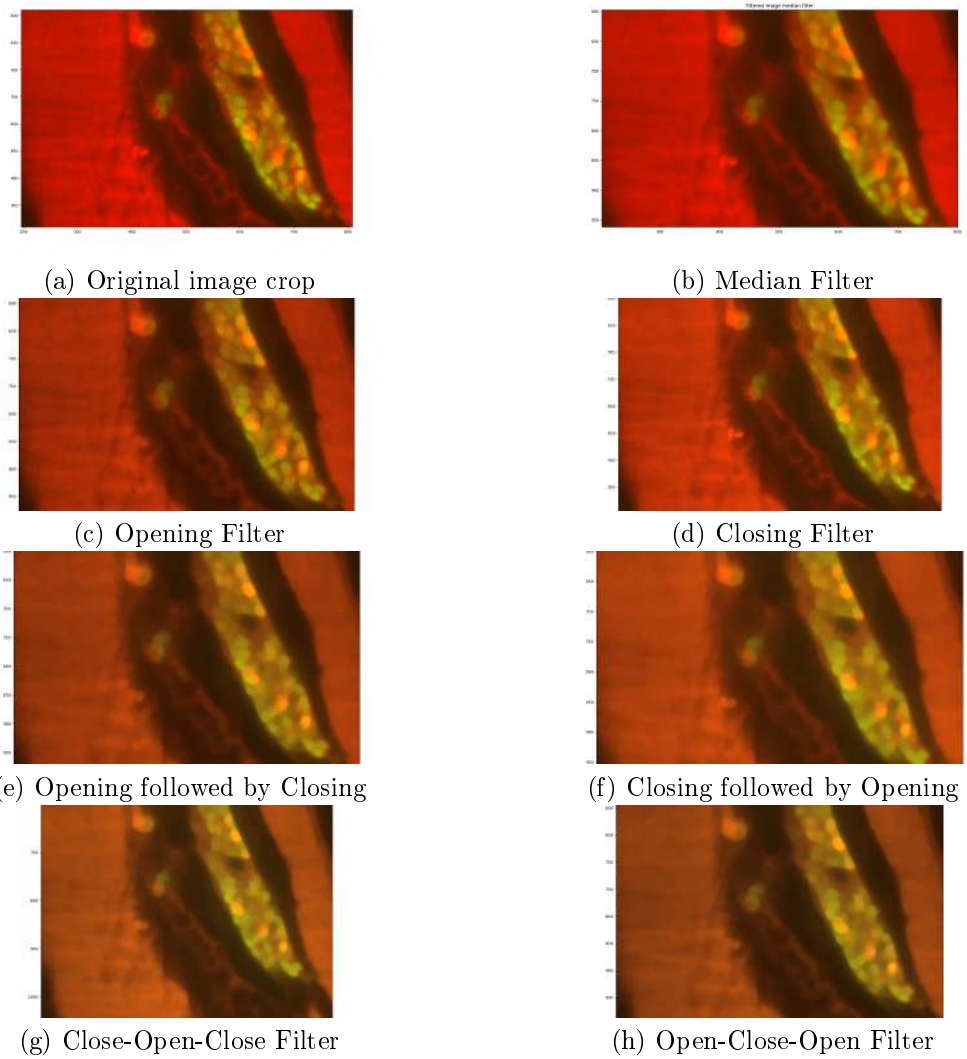

(a) Original image crop (b) Median Filter

(c) Opening Filter (d) Closing Filter

(e) Opening followed by Closing (f) Closing followed by Opening

(g) Close-Open-Close Filter (h) Open-Close-Open Filter

Table 7: Various morphological filters applied using a disk-shaped Structuring Element (SE) with a radius of 11 pixels: (b) Median, (c) Opening, (d) Closing, (e) Open-Close, (f) Close-Open, (g) Close-Open-Close, and (h) Open-Close-Open. The target object to be processed is the yellow neuron, so the convergence points are set to black and yellow. The image luminosity has been increased by a factor of two to enhance visibility, given the low signal-to-noise ratio (SNR) in the images.

For the target of green disks, the convergence points are set to black for O^- and green for O^+. Table **??** present an range of applied morphological filters using different SE sizes. When compared with the previous table where convergence points were set to black and yellow, our observations show that yellow neurons tend to fade out, while green shapes become more distinct in the image as it can be seen in **??** where the highest changes between the original and filtered image are for in the positions of the yellow neurons. Our observations demonstrate that as the SE size increases, certain neurons begin to merge, resulting in a loss of their ability to be differentiated as distinct entities. In contrast, employing a smaller SE size requires more iterations for convergence, and larger neurons necessitate a greater number of operations for processing. A larger SE size tends to make neurons resemble a "model neuron," taking on a disk-like shape.

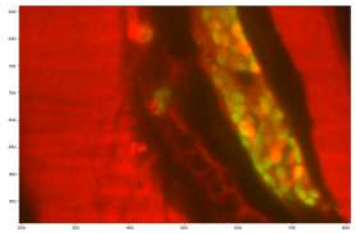

(a) Original image crop

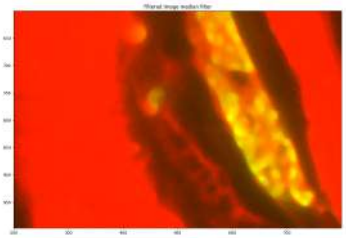

(b) Median Filter

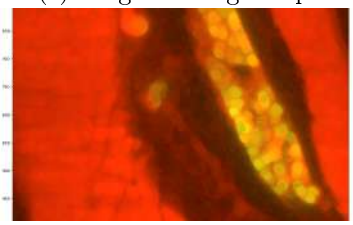

(c) Opening Filter

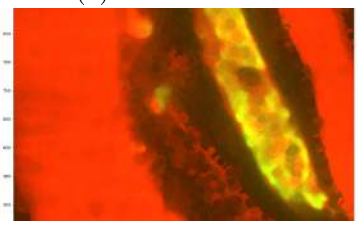

(d) Closing Filter

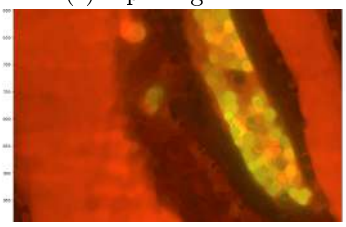

(e) Opening followed by Closing

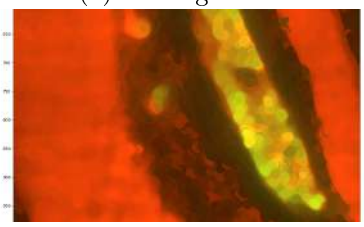

(f) Closing followed by Opening

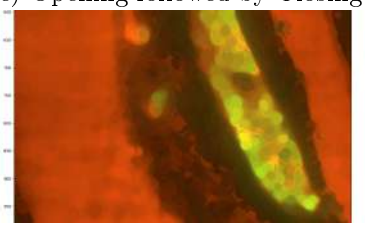

(g) Close-Open-Close Filter

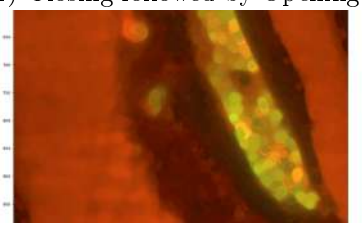

(h) Open-Close-Open Filter

Table 8: Various Morphological Filters were applied using a disk-shaped Structuring Element (SE) with a radius of 15 pixels: (b) Median, (c) Opening, (d) Closing, (e) Open-Close, (f) Close-Open, (g) Close-Open-Close, and (h) Open-Close-Open. The target objects to be processed are the green neuron, so the convergence points are black and green. The image luminosity has been increased by a factor of three to enhance visibility, given the low signal-to-noise ratio (SNR) in the images.

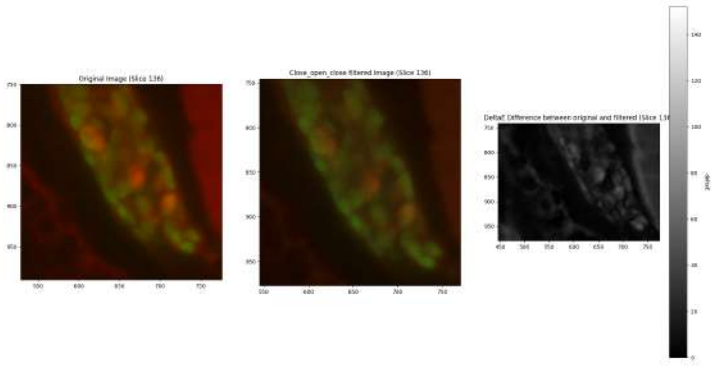

Figure 32: Open-Close-Open filter with an SE of radius 5 pixels. The convergence points are black and green. The third image shows the ΔE distance between the original and the filtered image.

Contributions

- Analysis of noisy nature in the measures of marker's response.
- Implementation of non-linear filter for multivariate images based on vectorial approach and CRA ordering.
- Test of morphological fiitering on mice heart images

5 Results

In this section, **first**, we will analyze the content of the mice heart image using the new markers. This image will be used to conduct CMOMP tests. **Second**, we will present some results of the **CMOMP** tests conducted on the mice heart images for neuron detection. For the presentation of results obtained using statistical methods, such as **texture analysis**, for ganglia segmentation on previous acquisition images, please refer to the Annex.
As depicted in Figure **??**, the slice contains background noise resulting from autofluorescence phenomena and ganglia present in other Z slices. Neurons are either part of a fiber extending along the XY plane or possess Z dimensions. Ganglia which are also constructed through the accumulation of neurons.

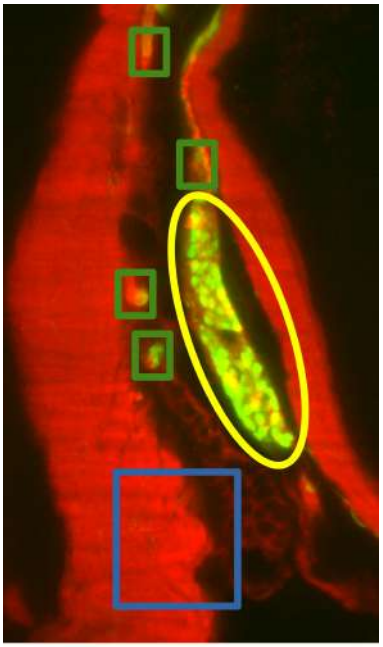

Figure 33: Content of the mice heart slice image (slice 135), used for CMOMP testing. Background noise is indicated by the blue square. Neurons, forming part of fibers along the XY plane or exhibiting Z dimensions, are denoted by the green squares. Ganglia, inside the yellow oval, are constructed from an accumulation of the green and yellow neuron structures.

5.1 Application of Probing on Heart Images

The main parameters of CMOMP include convergence points, spatial support size of the SE, SE shape and size, foreground and background values, and the threshold. Convergence points should be selected based on the foreground and background of the target object. The SE which defines the object's shape and value boundaries in the image, is constructed accordingly. An illustration of the inferior and superior SE is shown in Figure **??**. The size of the disks in the SE is determined by the adopted SE used in the filtering process. Foreground and background values are dependent on the target template. The size of the SE's spatial support needs to be tested and is influenced by how closely the objects are situated to each other. The threshold value depends on the specific SE employed; it is proportional to the distance between the inferior and superior SEs. In the images of mice hearts, defining a simple SE for all the green neurons is complicated, especially considering that the background range of these neurons and the background range of their foreground are the same. Therefore, specific models or SEs are required. A question might arise: **how many different SEs are needed to detect all neurons in the slice?**

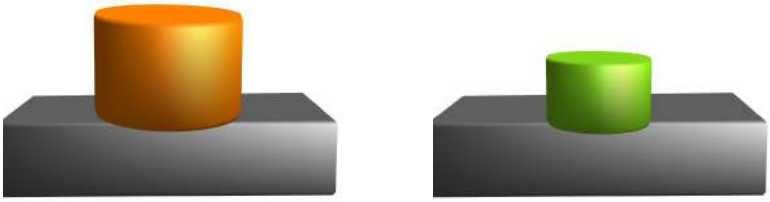

(a) Superior SE with a larger radius and higher color coordinates.

(b) Inferior SE with a smaller radius and lower color coordinate.

Figure 34: 3D representations of SEs.

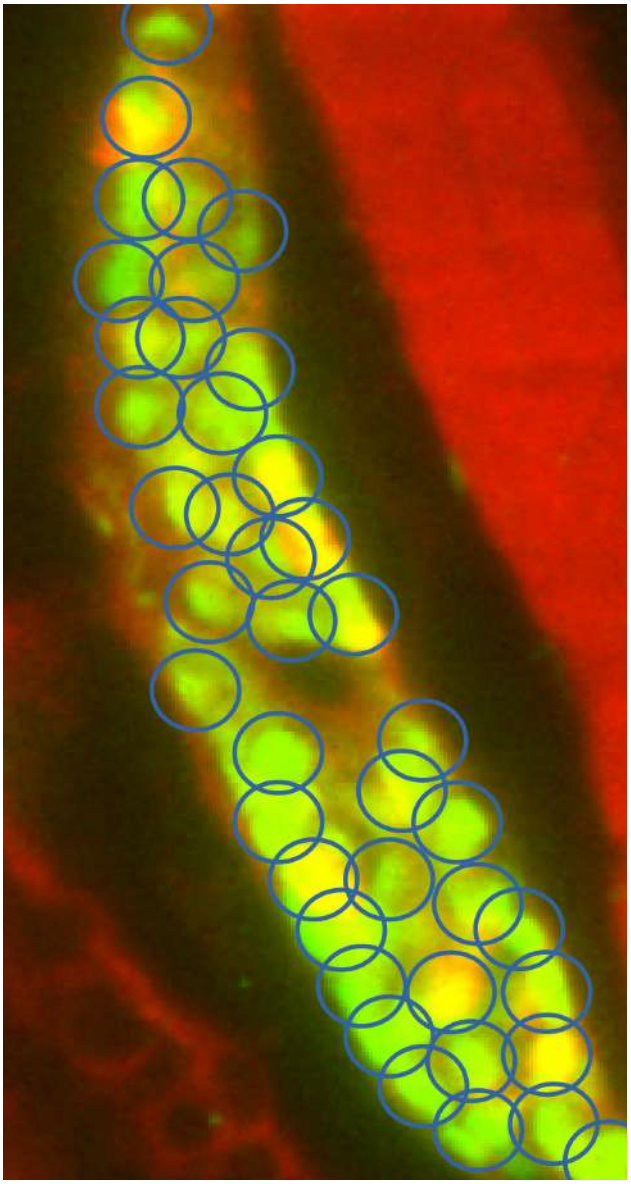

Figure 35: Ground Truth used for the assessment of CMOMP tests(slice 135). Manually generated without validation from the expert yet. Neurons are marked with blue circles.

In Figure **??**, an experiment was conducted to detect neurons similar to the one in Figure **??**. The threshold was varied to test the sensitivity of the CMOMP. **The threshold will be chosen to be fixed as the distance between the foreground of the inferior and superior SE, divided by 40.**

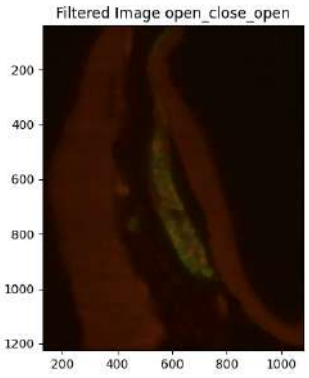

(a) Filtered image (slice 135)

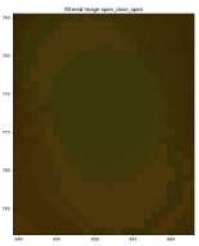

(b) Crop of the neuron used for the construction of the SEs.

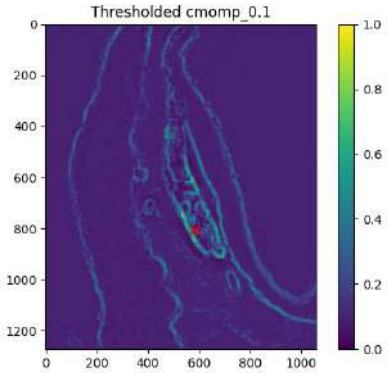

(c) $\tau = 0.1$

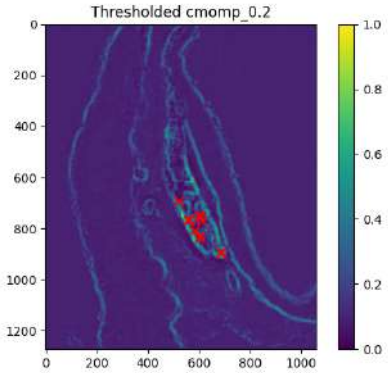

(d) $\tau = 0.2$

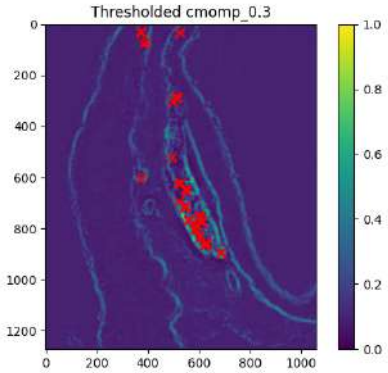

(e) $\tau = 0.3$

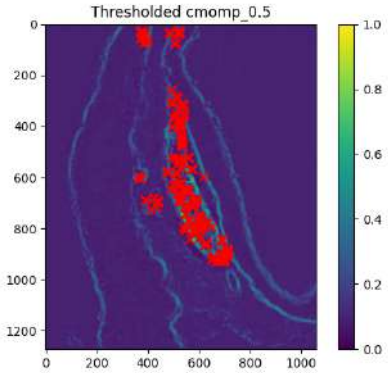

(f) $\tau = 0.5$

Figure 36: CMOMP applied to detect a green neuron. The SE was manually constructed based on the chosen neuron's foreground and background ranges. Different thresholds were assessed.The red crosses indicate the positions of detected neurons.

In Figure **??** and Figure **??**, experiments were conducted to detect another model of green neurons. In the first figure, we applied the algorithm to different nearby slices to verify that certain neurons were not being detected due to their presence in other slices where they have a maximal response in a different Z dimension. This is because during the acquisition, each Z plane is sequentially excited with the laser from bottom to top.

In the figure **??**, we tested changing the convergence points. We observed that exchanging black and green pairs with yellow and green did not significantly impact the results. This experiment was carried out because some neurons have a black background while others have a green background, and some neurons

have different foreground colors, either yellow or green. Therefore, the choice of convergence points needs to be made according to the specific SEs.

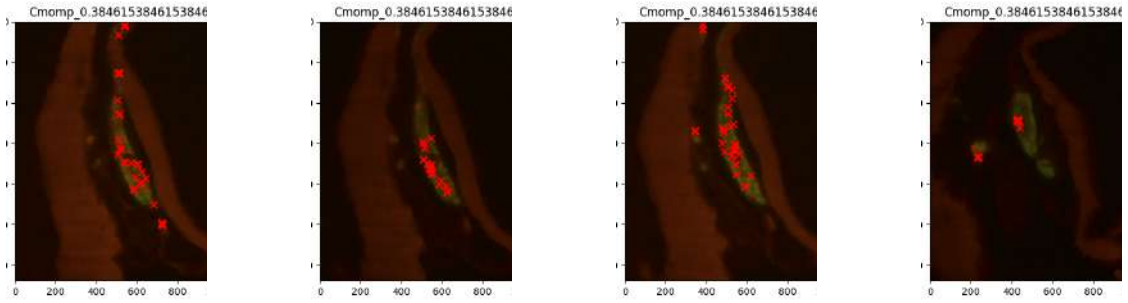

(a) Slice 133 (b) slice 136 (c) Slice 139 (d) Slice 175

Figure 37: CMOMP applied on different slices to detect a green neuron target. Convergence points: green and black. $\tau = d(g', g'')/40$. The red crosses indicate the positions of detected neurons.

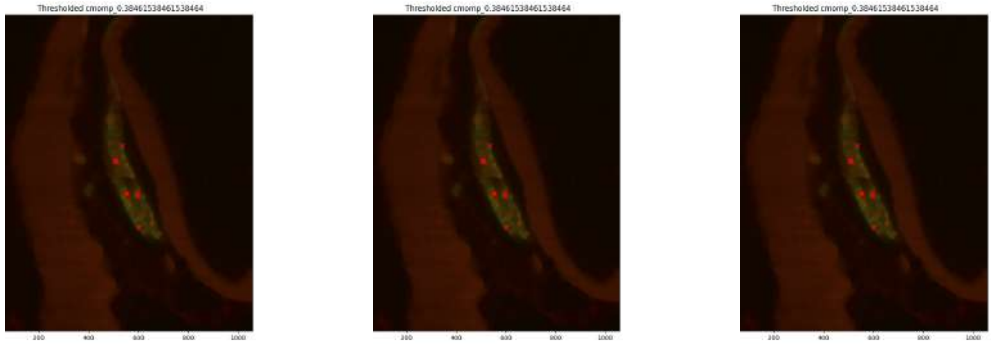

(a) Convergence points: green and black. (b) Convergence points: yellow and black. (c) Convergence points: black and green.

Figure 38: CMOMP applied to detect a green neuron target on the same slice (135). Different convergence points were used. $\tau = d(g', g'')/40$. The red crosses indicate the positions of detected neurons.

In Figure **??**, we experimented with the detection of a yellow neuron. For this purpose, yellow and black convergence points were set for both the filter and CMOMP.

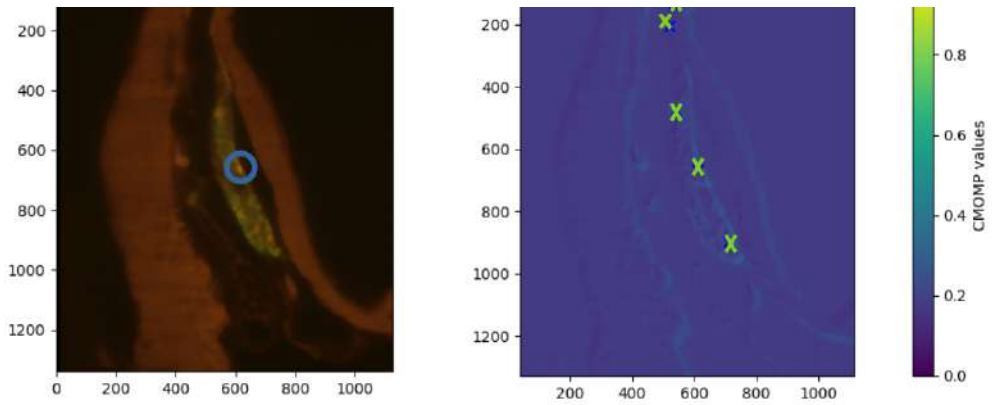

Figure 39: CMOMP applied with a yellow neuron model, circled in blue on the RGB ganglia image, which was filtered with convergence points set to yellow and black. In the CMOMP plot, detections below the threshold are marked with a green 'x'.

To quantify the algorithm's performance, I manually calculated the percentage of detected neurons in the slice and the precision of this detection. This provided insights into the percentage of false detections. The results clearly highlight that CMOMP needs to be implemented multiple times, adapting the filtering, CMOMP parameters, and SEs for the various targeted neuron models we intend to count. In MOMP, pairs of probes for detecting multiple objects are constructed from corresponding pairs specific to each object[?]. However, due to low SNR and variations in background and marker response, using a single pair of SE probes for all neurons led to a flat SE, reducing shape sensitivity. We proposed result combination from MMOMP applied to different neuron models addressed this challenge.

Table 9: Neuron Detection Results with Neuron Models on Slice 135. Percentage of neuron detection is computed based on the total number of neurons approximated in the slice. Multiple detections of the same neuron when different neuron models were used was taken into consideration.

Neuron Models Considered	Neuron Detection Percentage(Recall)	Precision
Model A(green neuron)	15%	1
Model B(green neuron)	32.5%	0.65
Model C(yellow neuron)	7.5%	0.6
All models combined	50%	0.76

We tested the probing applied in perceptual space on 2D slices for different slices, different neuron models, targets, and various CMOMP parameters. The results have indicated the necessity for further study on the SE construction. Defining all existing neurons models within the image is crucial for successful detection.

5.2 Statistical Approach Results

The initial objective of the internship was set to detect ganglia on previous dataset images. We introduced a texture descriptor for ganglia detection and its application in segmentation on 64x64x64 volumes, encompassing noise, ganglia, and fibers. We aimed to derive a distinctive feature by analyzing co-joint probability of pixel values and surroundings. The descriptor captures histogram of channel values around each voxel, using 15-pixel cubes. Manual references for ganglia, fibers, and noise are selected. Distance maps to reference descriptors are computed for voxel classification and image segmentation. Following segmentation, image classification is conducted. Instances of mis-classification, particularly fibers being incorrectly classified as ganglia, are addressed through the utilization of Principal Component Analysis (PCA). Performance evaluation of volumes classification:
Heart1 scores: Accuracy: 0.80 | Precision: 1.00 | Recall: 0.70 | F-measure: 0.82.
Heart2 scores: Accuracy: 0.846 | Precision: 1.00 | Recall: 0.778 | F-measure: 0.875.
Although these results may appear promising, it should be noted that they were only tested on samples from two hearts, which is insufficient. Additionally, the thresholds need to be tuned as there is no inter-individual normalization. Consequently, this approach is not viable in the long run.
For further details on these results, please refer to the annex.

Contributions

- Tested CMOMP on mice heart images.
  - Combined results of different neuron models.
- Assessed texture analysis-based feature extraction for ganglia segmentation on previous acquisitions.
  - Achieving 80% accuracy.
  - Utilized PCA components ratio comparison to identify tubular shapes, addressing some instances of fibers mis-segmented as ganglia.

6 Project Presentation

In this section, we will first present the **host structure**, the **involved teams**, and the relationship of my internship to each. After that, we will discuss the **project management**, including how tasks were assigned and organized, how **risks** were assessed and anticipated, and how we **adapted** to the risks and problems that occurred.

6.1 Presentation of the Host Structure & Relation With Other Projects Within the Organization.

I will be completing my Internship within XLIM labratory under the supervision of Dr. T. URRUTY and Dr. N. RICHARD. The project is a collaboration between XLIM and the Préti research labratories.

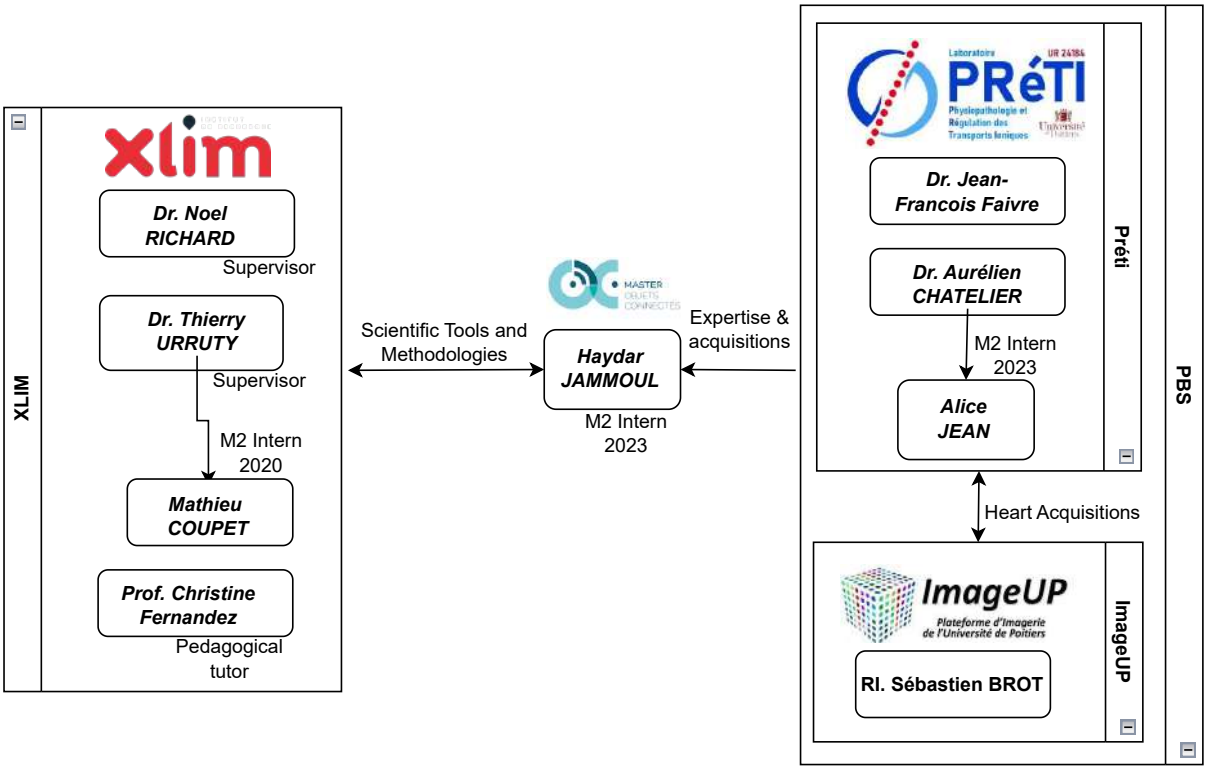

Figure 40: Project Structure

6.1.1 XLIM UMR CNRS 7252

XLIM UMR CNRS 7252 is an expert center in electronics, optics, photonics, mathematics, computer science, and imaging. It covers diverse fields such as space, telecom networks, bioengineering, and energy. XLIM is a multidisciplinary research institute spread across various locations, including Limoges and Poitiers. It comprises over 440 educators, researchers, engineers, technicians, and administrative staff.
ICONES is a Poitiers-based research team focused on color and spectral information processing in images and videos. Their research covers various areas, including measurement, acquisition, analysis, and decision support for multivalued images like color, multispectral, and hyperspectral images. Currently the biomedical field stands as one of the primary domains of application.
My XLIM supervisor, Dr. RICHARD the head of the ICONES research team, specializes in signal and image processing, with a particular interest in metrology and texture analysis. He has developed vector computation techniques for multivariate images. On the other hand, Dr. URRUTY is an expert in deep learning, automatic and semi-supervised approaches. He previously collaborated with M. Coupet on the issue of ganglia detection in cellular images using a deep learning approach. However, the results were

unsatisfactory due to limited data, inadequate annotations, and the nature of the images. The collaboration between these two experts, one specializing in data-driven and statistical approaches, and the other in handcrafted texture analysis and the study of shapes and granulometry in images such as Mathematical Morphology (MM), made this project particularly enriching. It allowed us to understand the value of each approach and how they can complement each other to achieve our goals in processing the available images.

6.1.2 Préti

PRéTI, which stands for "Physiopathology and Regulation of Ionic Transport," is a research laboratory affiliated with the University of Poitiers and led by Dr. Faivre. The lab focuses on investigating membrane ion transport across three primary domains: the cardiac environment (led by Dr. Aurélien CHATELIER), the skeletal muscular system, and epithelial membranes.
Throughout this project, I collaborated with Dr. CHATELIER's team and his intern, Alice JEAN. Our collaboration encompassed various goals, including my understanding of the project objectives and context, outlining the project specifications, conducting data analysis, and constructing the dataset. The long-term goal of my internship is to facilitate the characterization of ICNS structures within the acquisitions of light sheet images of mice hearts.

6.1.3 ImageUP

Furthermore, I had the opportunity to work with the ImageUP team, a technological platform that provides services and resources for electron and photon microscopy at the University of Poitiers. Notably, I collaborated with the research engineer responsible for the maintenance and usage of the light sheet microscope during the acquisition tests. I also received assistance from Anne Cantereau-Becq, the research engineer in charge of the optical microscopy service at ImageUP, who supported us in constructing the dataset using the facilities available at ImageUP such as Imaris software and the computers of ImageUP.

6.1.4 UP^2 project

The internships, both mine and Alice Jean's, were funded by the UP-squared project. UP-squarred aims to transform the University of Poitiers into a sustainable university, where sustainability is considered from a human, environmental, and societal perspective, directly addressing the needs of society and its territories. By promoting multidisciplinarity, UP2 focuses on three United Nations Sustainable Development Goals (SDGs), including health and well-being.

6.2 Project management

In this section, **first**, we will delve into my interactions with the individuals involved in the project and explore the utilization of agile project management using the Scrum framework. **Second** we will present the planning and the tasks assigned during the project. **Thirdly**, we will present the risk assessment that was conducted before the start of the project and updated with the changes and events that occurred, as well as how we anticipated these risks. And **fourth**, we will explain how we adapted to the problems that took place.

6.2.1 Human Interaction & Agile Project Management using Scrum

Sprint-Based Approach

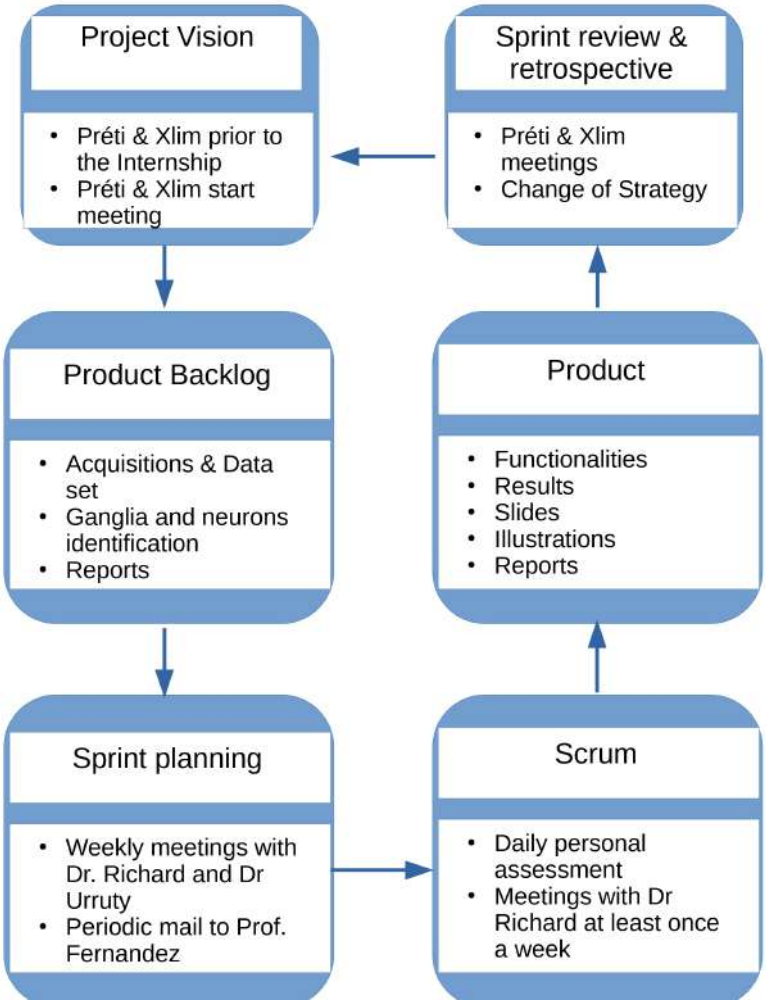

Figure 41: Tailored Scrum Methodology Applied to My Internship Project.

Our project embraced a sprint-based approach(figure **??**), reflecting the principles of Scrum. The project **vision** and initiation occurred with a comprehensive team meeting involving both XLIM and Préti researchers on May 19th. During the project, **weekly meetings were conducted with my tutors**, Dr. Richard and Dr. Urruty, at SP2MI. These meetings served as an opportunity to discuss progress or results, the scientific and technical choices, establish short-term and long-term goals, receive constructive feedback and plan for the upcoming week sprint. Ongoing communication was maintained through periodic emails and followup reports sent **every three weeks to my pedagogical tutor**, Prof. Fernandez. Meetings with M. Coupet at i3m or SP2MI provided insights into his prior implemented DL-based approach, enriching my understanding.

Sprint Review and Retrospective

Our sprint-based approach incorporated frequent feedback loops. Inputs from both my tutors and Préti researchers played a pivotal role in steering the project's evolution. Discussions with Préti served to improve current acquisitions, such as addressing low SNR, normalisation issues, and completing the dataset. Their feedback on the results and methods was enriching, especially given the aim of providing experts with control over algorithm parameters, which instilled a sense of security and trust. For instance, MMOMP allows Préti experts to choose the neuron model they intend to detect, offering a level of control that differs from DL approaches where predictions solely rely on training data. **Regular bi-weekly meetings** were scheduled with the Préti teams at PBS. These sessions were crucial to keep them informed about the project's progress, discuss outcomes, adapt objectives if necessary, and seek their expertise on specific image-related challenges. During the initial stages until mid-April, I collaborated closely with the Préti intern, Alice Jean. Our interactions aimed to understand and analyze the data and build the dataset. We continued to hold periodic meetings, discussing planned acquisitions, project progress, and advancements. Scrum sprint

retrospectives and reviews were instrumental in our effective adaptation to challenges, notably the failure of image acquisition, which prompted a direct shift to Morphological Methods (MM).

Product Backlog: Specification Document

Before the internship: The initial specifications from the Préti in the first meeting were focused on exploring methods to detect ganglia in the image acquisitions that enable the measurement of ganglia volume.

Adapted specifications and goals: After exploring DL approaches and using texture analysis to segment the ganglia, and after conducting test acquisitions using new markers, we decided to explore multivariate MM probing **for the goal of detecting the neurons.** It was the outcome of discussions with Dr. Richard, who had previously supervised the theses of Ledoux and Deborah. As a result, he was already acquainted with the potential applications of Mathematical Morphology (MM) in multivariate contexts, as well as the color template probing that was developed during Ledoux's thesis.

The deliverables include (deadline: 30th of September):

- Proof of Concept (PoC) for ganglia segmentation and neuron detection.
- Library: Multivariate MM .py and accompanying code documentation.
- Scientific report intended for use by future interns or doctorate students.
- Reports for Préti and ImageUP regarding the request for normalization and adaptation of acquisition parameters.

Constraints (Software, Hardware, Deadlines): Reservation of the lightsheet microscope and coordination with the responsible research engineer and Préti were necessary. The required software for this project initially included ImageJ and Imaris. The latter was provided on the ImageUP machines, incurring a cost of $9000 per year per machine. These software tools were utilized to crop the 20GB images into smaller segments that could be processed on my laptop. This was particularly important since we were only interested in the upper region of the heart acquisitions where the ICNS structures are located. Throughout the project, I worked on a machine provided by the Xlim laboratory, equipped with 64GB of RAM and a 2GB graphics card to enable task parallelization. For Python code development, my main tools were Spyder IDE and Visual Studio Code (VSCode).

Costs:

The running costs of 15,000 € per year include expenses for plastic ware, enzymes, antibodies, pharmacological tools, biochemistry and molecular biology reagents, and small materials for patch-clamp experiments, as well as viral preparations. Furthermore, 77,000 € are be allocated for outsourcing and subcontracting. This will cover internal microscopy platforms (16,000 €) and animal facilities (33,000 €) for animal acquisitions and cryo-recovering (12,000 €). Both my internship and Alice Jean's internship incurred a cost of 3600 euros each.

We also drew on concepts from the V-Model methodology, including long-term planning for objectives and requirements anticipation. Sprints were planned to build up-to long-term goals. For instance, one long-term objective was the implementation of CMOMP for neuron detection. **Sprints were strategically divided to target this goal**, including MM for binary implementation, MOMP for grayscale, and MOMP for multivariate implementation. Our approach also involved **unitary and integration validation** of developed functionalities. This encompassed MM operator validation, synthesis image testing, validation of mathematical properties, and finally, practical tests on mice heart images.

6.2.2 Initiation and planning

The initial phase of research project management is crucial for setting the objectives and goals. In my case, the goals were established during a collaborative meeting between both teams. **The goals are focused on detecting cardiac ganglia, measuring their volume, and counting the neurons within them**. To accomplish these objectives, the necessary resources involve collaboration with the pathologist to gain a comprehensive understanding of the images and the structures we are investigating and constructing a data-set for training and testing algorithms.

After the initiation stage, the planning stage follows, which includes scheduling tasks. The initial Gantt chart was set upon the initial team meeting (Figure **??**). However, following the decision to start acquisitions using new markers and due to the poor reproducibility of statistical-based approaches, a new Gantt chart was established with a focus on mathematical morphology techniques. This adapted Gantt chart is shown in

Figure ??. Additionally, certain tasks were unanticipated, leading us to allocate time for them, such as testing morphological filters and resolving issues in the multivariate morphology probing implementation.The implemented Gantt chart is shown in Figure ??.

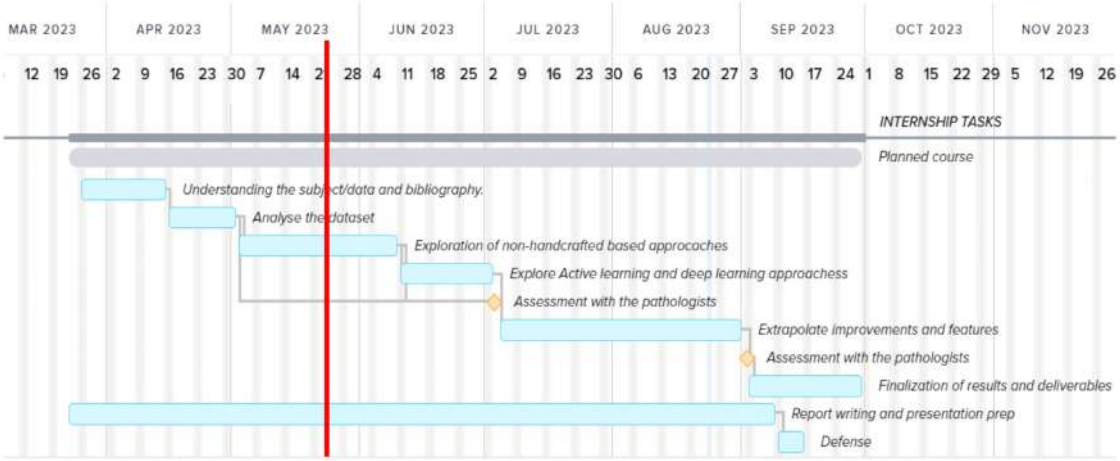

Figure 42: Initial Gantt chart. The vertical red line shows when the new strategy was decided.

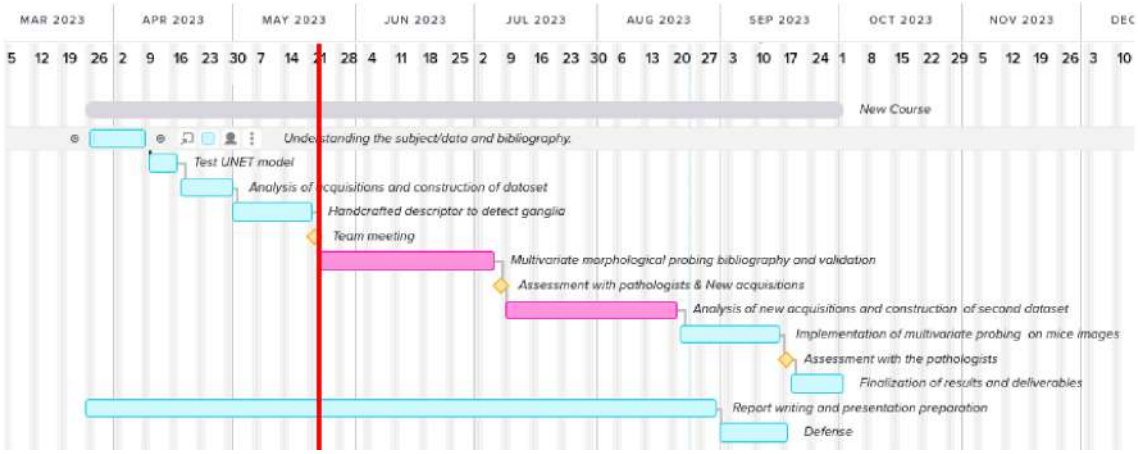

Figure 43: Adapted Gantt chart. The vertical red line shows when the new strategy was decided. The tasks in pink are the ones planned after the new course.

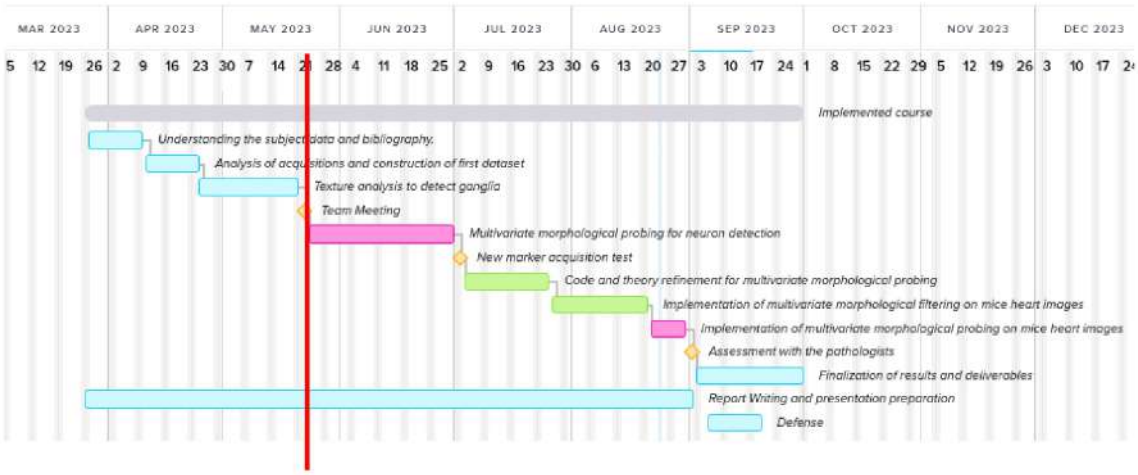

Figure 44: Implemented Gantt chart. The vertical red line shows when the new strategy was decided. The tasks in pink are the ones planned after the new course. The tasks in green are the ones implemented without prior anticipation.

Table **??** offers a descriptive overview of the major tasks considered during this internship. It includes the objectives of each task, the challenges encountered, the completion status, and notes on how the challenges were addressed or how the tasks were implemented.

Table 10: Task Progress - Major Tasks

Tasks	Objectives	Challenges	Status
T1	• Understand the subject and problem statement. • State of the art implementation.	• Limited works on the subject. • Limited documentation of the previous works of the team.	Done 100%
T2	• Analyze data. • Construction of dataset.	Poor quantification resolution, noisy and blurry images.	In progress 80%
T3	Test non-linear filters.	Time complexity of algorithms, test multiple parameters.	• In progress 60%. • Need to test different convergence points and kernel sizes.
T4	• MM documentation. • Implementation of extension to multivariate images.	Existing implementation not conforming with the literature.	Done 100%
T5	Document the research work and prepare presentations.	N/A	In progress 60%
T6	• Add more distance functions for multispectral extension. • Construct 4D SE for 3D extension. • Tensorflow implementation of convolutions.	Choice of distance function according to the mathematical nature of the images.	In progress 50% - To do

A detailed progress table with subtasks can be found in the annex.

6.2.3 Risk Anticipation

In this sub-section, we will list the anticipated risks during this project, explain how we assessed them, and detail the steps taken to anticipate these risks, as summarized in Tables ?? and ??. The color codes for criticality scores are explained in Figure ??.

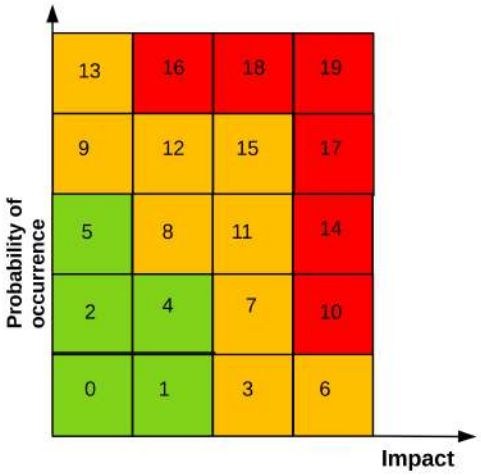

Figure 45: Matrix of Risk Criticality based on probability of occurrence of a risk and its gravity.

Table 11: Anticipated Risks with Risk Criticality Scores.

Risk	Initial Score	Risk Mitigation Strategies
New image acquisition failure with the new markers	19	• Made use of previous images. • Transitioned to exploring MM. • Utilized a ganglia image provided during the acquisition tests.
Low SNR in images	19	• Minimal time spent on AI based approaches. • Implementation of filtering. • CMOMP allows shape and noise tolerance. • The teams agreed to define a methodology to adapt the acquisition parameters. (Not solved yet)
Incomplete ground truth dataset	16	• Collaborated with Alice JEAN and our tutors to define a strategy to construct the ground truth dataset.

In the next subsection, we will discuss how we addressed the challenges that arose.

Risk A: New Image Acquisition Failure with the New Markers Initially, acquisitions of 5 to 20 hearts with the new markers were planned. Risk A pertains to the potential failure of image acquisition due to factors beyond our control, particularly as biologists are replacing ChAT with PGP, as discussed in our initial meeting. This risk could disrupt data collection for testing and validating the algorithms. During the project, acquisition sessions did not yield promising results, increasing the likelihood of this risk occurring. Thankfully, the biologists provided a single ganglia volume acquisition using the new marker, which was used to test the CMOMP algorithm. This event, combined with the adoption of MM and the abandonment of DL-based methods, reduced the severity of this risk. Nevertheless, it still hindered us from conducting comprehensive tests on the entire heart and various individuals to thoroughly validate the algorithms.

Risk B: Low SNR in Images, "Beautiful Image" or "Useful Image" From the first meeting, the challenges associated with these images were discussed, particularly the often blurred and noisy responses of the markers. This issue, encountered in previous internships, led to limitations in their outcomes. Préti had plans to replace one of the channels.

During the meeting on May 20th, we delved into this problem after analyzing images, as represented by the boxplots in Figure **??**. These boxplots illustrate the voxel value distributions of ganglia and noise crops for both channels. Surprisingly, volumes containing noise (auto-fluorescence phenomena) and volumes containing antibody reactions exhibited similar dynamic ranges. The values in the first three quartiles did not surpass a few hundred for both channels. This suggests that the full measurement potential of the 16-bit sensor is not being utilized.

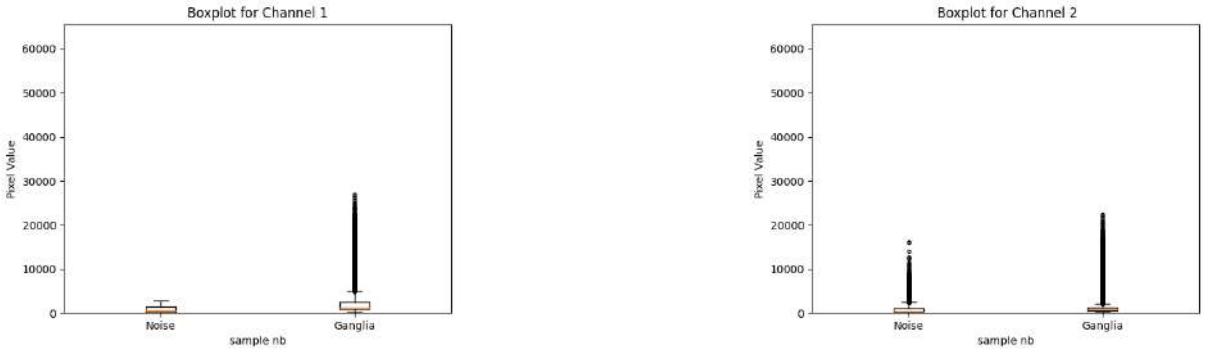

(a) Channel1 (b) Channel 2

Figure 46: Boxplots of both channels for two volumes of the same size (64x64x64), centered around noise (auto-fluorescence) and ganglia. **The dynamic range is not exploited.**

A possible explanation for this phenomenon is that biologists often seek visually appealing images, where noise or the auto-fluorescence effect helps locate structures within the heart. However, for our specific tasks, we need to harness the markers' responses for precise measurements. This creates a conflict between obtaining a "beautiful image" and a "useful image." To address this, we proposed adjusting acquisition parameters like amplification and exposure time for new mice heart acquisitions. Our aim is to achieve sensor responses aligning with the ideal boxplots shown in Figure **??**, thus not fully utilizing the measurement capabilities of the 16-bit sensor.

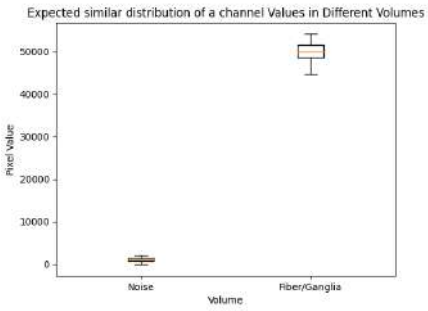

Figure 47: Ideal Box-plots illustrating the expected value distribution in a given channel for a 16-bit depth sensor. We anticipate a higher sensor response for a marker response (ganglionic neurone/fiber).

While adapting the acquisition parameters, we expect to improve the sensor's dynamic range and sensitivity, enabling more accurate and informative measurements. However, as no tests for this adaptation were conducted, this risk remains probable. Furthermore, the implementation of morphological filtering and the use of CMOMP, which allows tolerance to noise and shape differences, have helped mitigate its impact.

Risk C: Incomplete Ground Truth Dataset Throughout this internship, we anticipated a risk associated with the expert's ground truth. After analyzing previous datasets and discussing with M. Coupet, we identified several challenges, including:

- Insufficient samples for certain noise, artifacts, or fibers, leading to an uneven class distribution in the dataset.
- The lack of metadata, such as physical resolution, making it difficult to compute ganglia volumes in the images.
- Uncertainty in the expert's segmentation and classification of volumes.

During the ganglia segmentation phase, the dataset was not validated by the intern's supervisor until the beginning of May, resulting in labeling errors affecting previous results and analyses.
Recognizing these issues, we took the opportunity to learn from our mistakes before new acquisitions. Collaboratively, we devised a new annotation strategy and created a more suitable dataset. This was crucial for effective and efficient annotation during new image acquisition. We explored documentation of software tools like ImageJ and Imaris to identify the most efficient method for annotating required data and establishing three classes: noise, fibers, and ganglia. Access to powerful machines and software licenses at ImageUp facilitated visualization and processing of the 20GB images. Constructing a validated dataset was the initial step toward achieving the main project goal of ganglia detection. We also decided to present the dataset only after validation to avoid confusion and save time. With the upcoming new acquisitions, the risk of an incomplete dataset is expected to be significantly reduced with these recommendations.

Table 12: Impact of Risk Mitigation

Risk	Initial Score	Revised Score
Image Acquisition Failure with the New Markers	19	15
Low SNR in Images	19	13
Incomplete ground truth dataset	16	4

6.2.4 Adaptation to problems that took place

As an intern in a research environment,I must adapt to unpredictability by swiftly adjusting. The scientist's mindset of **embracing changes is key** to overcoming challenges related to acquisitions, choice of algorithms, or methodologies, and ensuring the project's success. The table **??** lists the risks or problems that took place and how we adapted.

Encountered Problems	How We Adapted
Normalization problem	• Postponed working on automatic methodologies. • Focused on pretreatment and template probing. • The teams agreed to define a methodology for establishing a white reference.(Not solved yet)
Scientific Libraries Inadequate for Multivariate Images	• Implementation of non-linear filters based on CRA-ordering • Focused on validating the implementation by checking the mathematical properties of MM operators (duality and idempotence).

Table 13: Problems that took place and how we adapted

Normalization problem
Normalization is crucial for automatic processing and analysis as it standardizes data, enhances contrast, and removes biases. However, we encountered challenges in defining the "black" and "white" references

required for normalization. The black reference represents the sensor-related noise which can be measured by acquiring an image while the sensor lenses are hidden. The white reference expresses the ideal or maximal response of a neuron or ganglia. As of now, we are still working on determining an objective definition for the white reference, as the maximal response depends on the tissue and individual and the position of the molecule inside the tissue. This problem raises questions about the feasibility of automatic and data-driven approaches. Until a solution is found, we manually normalize each individual based on its intra-values before applying texture analysis and morphological probing.

Scientific Libraries Inadequate for Multivariate Images

When implementing the filtering functions and the MM operators and probing functions, validation of each implementation is crucial. One approach is to compare our results with other existing implementations or to test on specific examples where we can predict the expected outcomes. At the beginning of learning about MM, I started with implementations on binary 1D and 2D images. For grayscale images, at first, I relied on skimage and OpenCV libraries to compare my implementations. However, I found that the implementation of grayscale erosion and dilation in these libraries did not conform to the literature, leading to incorrect results. This was due to pixel value interpretation, as they did not consider the possibility of dilation resulting in values larger than the maximum (e.g., 255 for 8-bit images) or values below 0, as mentioned in [**?**]. Additionally, defining pixel values as integers in these libraries caused repeated counting for negative values in erosion and values larger than 255 in dilation, resulting in numerically incorrect and unreliable validation of our functions. **This experience highlighted the importance of specifying variable types in Python and being aware of unconventional conventions, such as BGR instead of RGB, in OpenCV.** For this reason, to validate the implementation of MM operators, it was more appropriate to rely on the verification of the mathematical properties of the operators.

For color conversion from RGB to CIE lab space, OpenCV's color conversion algorithms may not always offer the same level of accuracy and precision as the Colorpy library. Unlike OpenCV, Colorpy treats image pixel values as float32 and provides the flexibility to choose the illuminant for color conversions.

Furthermore, filtering and performing morphological operations using these libraries on multivariate images using the **marginal approach** provide empirical rather than accurate results. This deviation from our goal of aligning with the physical and mathematical nature of the image as a sensor's measure. For that, we implemented the filtering algorithms based on **CRA ordering**.

7 Conclusion

7.1 Project Conclusion

From a technical perspective, the accomplishments of this internship include:

- Analysis of acquisitions, revealing challenges and issues:
  - Discussed the trade-off between beautiful images and exploitable images.
  - Highlighted the absence of normalization references, which hinders automatic processing.
- Exploration of texture analysis for ganglia segmentation.
  - Exploration of post-processing techniques to distinguish errors, such as fibers, through blob detectors and PCA-based analysis.
- Development of a functional MM library for multivariate images.
- Generation of documentation using docstring.
- Exploration of morphological filtering, conducting tests to compare the impact of filter parameters.
- Implementation of multivariate morphological object probing.

From a scientific standpoint, the contributions of this internship encompass:

- Implementation of multivariate morphological probing based on an ordering that preserves idempotence of opening and closing operations.
- Introduction of extended convergence points for successive morphological operations, ensuring continuity of transformation and preventing saturation.

Were the objectives of the internship achieved? What is the value of this internship for both research teams?
No, automatic detection in the new acquisitions was not executed due to acquisition failures and the absence of normalization.

However, yes, certain objectives were addressed successfully. We proposed a ganglia segmentation method based on texture analysis, which requires testing on images with new markers. Additionally, we introduced a pre-treatment approach utilizing morphological filtering. Furthermore, we devised a methodology to identify neurons within a ganglia, aiding in the counting of neurons in a ganglia.

For XLIM, we explored a multivariate morphological probing methodology that has broader applicability to other color or multispectral images. This internship shed light on the problematic aspects and challenges of an automatic approach for ICNS characterization. This internship highlighted for Préti the problems and challenges associated with an automatic approach for ICNS characterization. The acquisition issues need to be resolved to enhance the signal-to-noise ratio, which in turn distinguishes between a "beautiful image" and a "useful image".

7.2 Personal Conclusion

During this internship, under the guidance of Dr. Noel Richard and Dr. Thierry URRUTY at XLIM Laboratory and the ICONES team, I gained essential **research skills, task management, productivity, and risk assessment**. Collaborating at the intersection of AI and image processing in pathological biology was a transformative experience. With Dr. Richard's mentorship, I cultivated a researcher's mindset, exploring innovative methodologies inspired by Matheron and Serra's works, overcoming traditional statistical limitations.

I am deeply appreciative of Prof. Christine Fernandez, Mathiew Coupet, XLIM lab, ICONES team, and I3M for their guidance and enriching discussions. Working with Dr. Aurelien Chatelier, Dr. Jean-Francois Faivre, and the Préti team provided invaluable insights into biological signal and image acquisitions, analysis complexities, and reproducibility challenges.

This interdisciplinary work in cellular images has shaped my research journey. Embarking on my **Ph.D.** with the Morpheme team at I3S/INRIA Sophia Antipolis, I am excited to advance in biological signal and

image processing, focusing on quantifying developmental variability in Ascidian embryos imaged using light sheet microscopy.

My gratitude extends to the Tactic graduate school, i3M, and the pedagogical team for their contributions to my knowledge. The programming, algorithmic skills, interdisciplinary exposure to data analysis, computer vision, signal processing and radio-communication aspects enhanced my comprehension of signal and image processing.

7.3 Future Considerations

In the project's next phase, we plan to:

1. Implementation of the multivariate probing in the physical domain(spectral domain) with spectral distance functions rather than the perceptual domain.
2. Utilize the concept of deep morphological networks, as demonstrated in [?], to enhance execution time during the implementation of morphological operations.

Continuing the project, we aim to:

1. Acquire and label mice heart images with TH and PGP markers.
2. Establish a strategy for acquiring a "white" reference, enabling inter-individual normalization.
3. Deeper study for the construction of the SEs.
4. Implementation of the multivariate probing in 3D.
5. Address the "beautiful image vs exploitable image" dilemma by refining acquisition parameters for better marker response exploitation and accurate fiber and ganglia detection.

These endeavors will enhance image analysis methods, furthering our understanding of neuronal structures.

8 Apendices

8.1 Appendix A:

Table 14: Task Progress

Task	Objectives	Challenges	Status	Approach/Remarks
T1	Subject and problematic comprehension	Limited works on the subject	Done 100%	Skimed Lizot thesis
T2	Re-impliment previous team's code	• No documentation • Small data-set	Done 100%	• Contacted M. COUPET • Mediocre detection results
T3	Data annotation strategy	• Large Images (20Gb) • New to Imaris/ImageJ software	Done 100%	• Collaborated with Alice Jean and ImageUP • Dr URRUTY provided his previous experience to help
T4	Image analysis	• To wait for the new acquisitions • Current acquisitions poor quantification resolution • Noisy and blurry images prevent the clear distinction of some essential features.	In progress 60%	• Failure of acquisitions • Not much progress with the previous acquisitions

Continued on next page

Table 14 – Continued from previous page

Task	Objectives	Challenges	Status	Approach/Remarks
T5	A handcrafted descriptor to detect ganglia	Poor differentiation of some fibers or aggregates of markers from ganglia	Done 60%	• Only tested on 1st acquisition images • Used blob detector to detect fiber shapes • Sensitive to some noise • Eventually chose to pass to other approaches as the new acquisitions were planned and expected to have different stats
T6	MM documentation and its extension to multivariate signals	A lot of existing approaches that extend MM operation to multivariate images (marginal, lexicographic...)	Done 100%	• Dr. Richard provided help to comprehend MM basic operations & multivariate ordering • Made use of Ledoux and Xlim previous works
T7	Implementation of MM	Implementation of existing libraries not corresponding to literature	Done 100%	• Took time to debug the implementation • Make =-use of athematical propreties of MM operators to validate them.
T8	Pretreatment and filtering of Mice heart images	• Time complexity of algorithms • Test multiple parameters	In progress 60%	Tested Min, max, median and Morphological filters.

Continued on next page

Table 14 – Continued from previous page

Task	Objectives	Challenges	Status	Approach/Remarks
T9	Implementation on Mice heart images	Choice of appropriate distance function	To Do 50%	• The ΔE distance is coherent with the expert's human perception of color, which they use in manual segmentation. • The Mahalanobis distance might be interesting to compare, as in the new acquisitions, we suspect that both channels would be correlated.
T10	To adapt new acquisitions	• Quantification resolution not exploited • Noise & channels responses low values	In progress 30%	With Dr. Richard we proposed to adapt the acquisition parameters
T11	Analyse Th and Pgp acquisitions	Postponed acquisitions	To Do 10%	Analysed a single ganglia sample image.
T12	Implement ganglia detection and MM operations on new acquisitions	-	To Do 0%	-
T13	Compare data driven approach to handcrafted descriptors	-	Discarded 0%	• To spare training timing. • No dataset on the new channels. • Normalization yet to be accomplished.
T14	• Reduce high computation time	-	To do 0%	• To benefit from neural netwok libraries such a tensorflow to perform to desired convolutions • To parallelize the convolutions

8.2 Appendix B: Non-linear filtering

Nonlinear filtering encompasses operations such as minimum, maximum, median, and morphological operators. These operations involve value selection rather than a weighted sum, as seen in linear solutions,

within a convolution process. The implementation of these filters using a marginal approach for multivariate images (processing each channel separately) yields non-metrological results and introduces new coordinates not present in the original image. The significance of implementing non-linear filters based on a vectorial approach lies in their ability to avoid the integration of "false" colors or measurements, ensuring that the proposed correction remains faithful to the initial dataset.

Next, we will present median filtering based on CRA ordering and demonstrate its application to the mice heart image. Additionally, we will cover the min and max filters along with some morphological filters experiment that have not been shown in this report yet.

8.2.1 Median Filtering

Libraries such as opencv support median filtering for rgb images where each channel is processed seperately (marginal processing) which looses metrological meaning and may generate new colors ("false" colors) not present in the original image as in figure **??**.

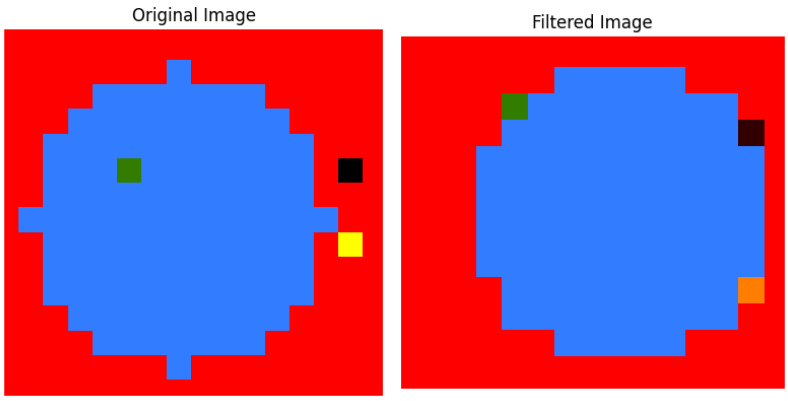

Figure 48: Marginal median filtering generates fake color that do not exist in the original image, as indicated by the presence of the orange dot along the border of the blue disk.

For that for multivariate images CRA ordering is chosen instead of a marginal approach. As in table **??** when applying median filtering the size of the kernel, its origin and its shape is an important choice to make according to the noise and the desired shapes in the image that needs to be processed. The choice of the median value in a CRA based filtering will depend also on the chosen convergence points.

Table 15: Filtered Images with Different Parameters

Label	Image
Original Image	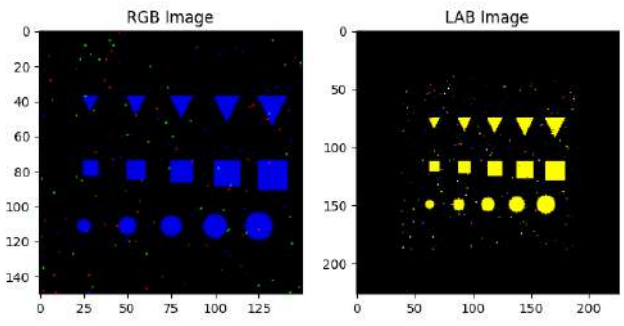

Continued on next page

Table 15 – *Continued from previous page*

Label	Image
Median Filter with Kernel 3x1	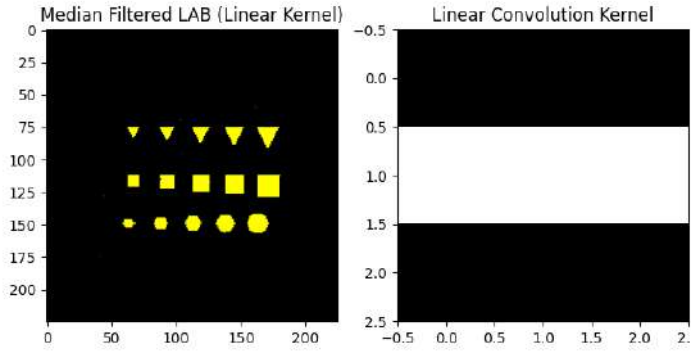
Median Filter with Square Kernel	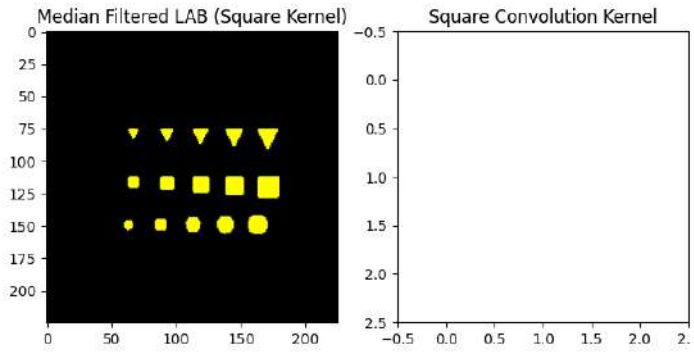
Median Filter with Circle Kernel (Radius 3)	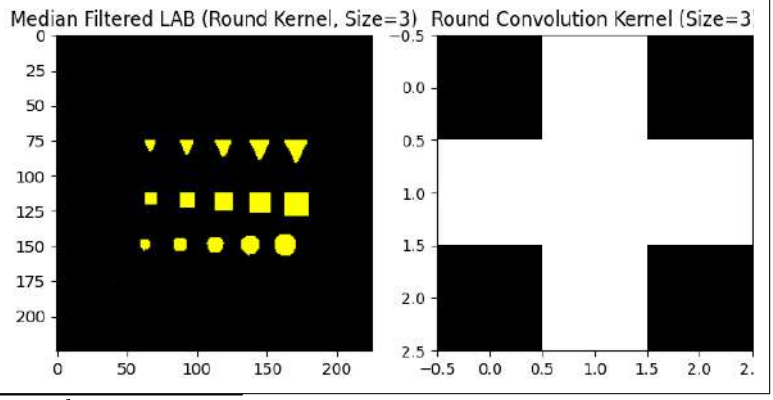

Continued on next page

Table 15 – *Continued from previous page*

Label	Image
Median Filter with Circle Kernel (Radius 5)	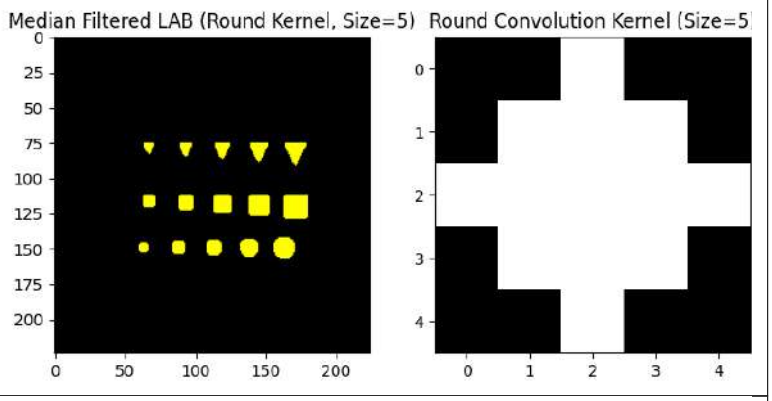
Median Filter with Circle Kernel (Radius 10)	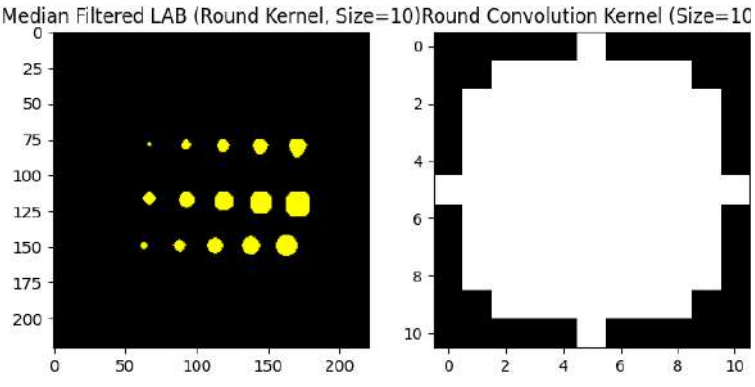
Median Filter with Circle Kernel (Radius 15)	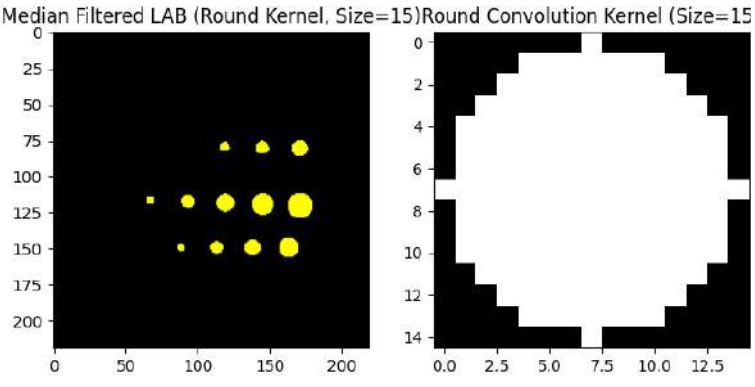

From the previous experiments with median filtering based on CRA ordering, we noticed that median filtering preserves the boundaries of the objects as long as the kernel size is smaller than the desired object. Therefore, the size and shape of the kernel need to be adapted to the desired objects in the images.

In **??** the original image in RGB and lab space that we used to test the different types of filtering in this section.

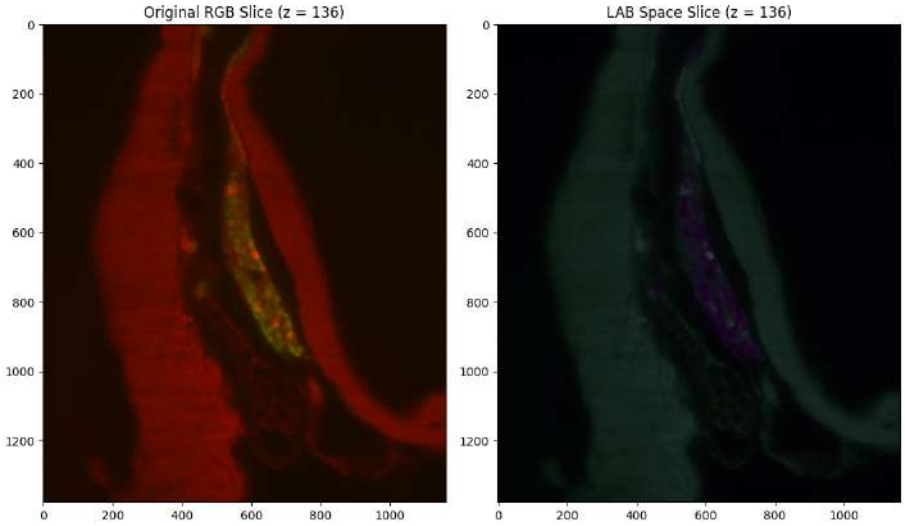

Figure 49: Original image used to test different filters implemented in RGB and LAB.

Applying median filtering based on CRA ordering to a ganglia slice in Figure **??**, we observe that the image is still somewhat noisy, but the variations within a neuron structure are significantly reduced.

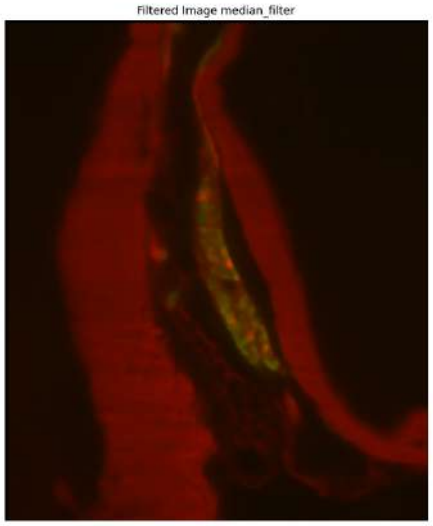

(a) Median Filtered Image

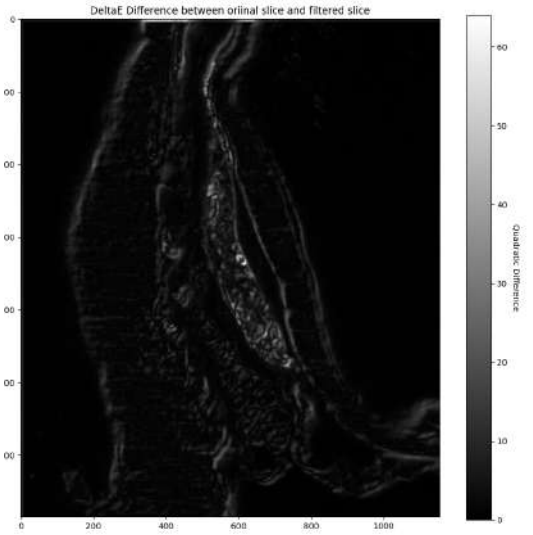

(b) Delta E between Filtered Image and Original Image

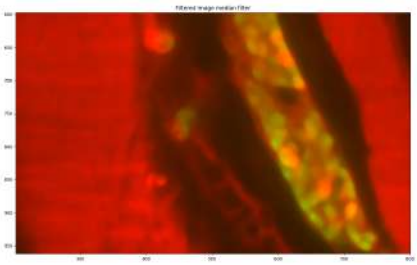

(c) Zoom in Median Filtered Image

Figure 50: 2D ganlia slice with median filter CRA-ordering based applied. Convergence points are black and yellow. Kernel filter size is a disk of 11 pixels radius.

8.2.2 Min Max Filtering

Minimal and maximal filtering are equivalent to erosion and dilation operations using a flat Structuring Element (SE). In Figure **??**, we zoomed in to examine interesting areas of the slice that demonstrate how the neuron responses are filtered.

With minimum filtering, we observe that the neurons structures are lost, while with maximum filtering, the neuron structures become clearer. However, with maximal filtering the desired uniform disk-like shape was not achieved.

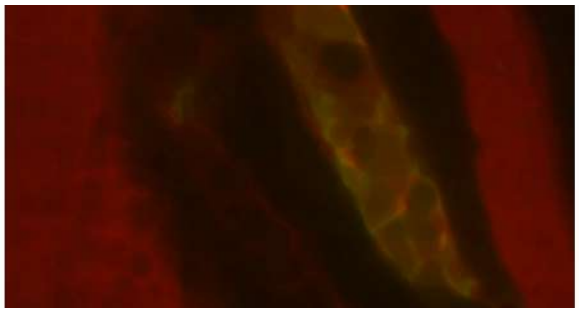

(a) Minimum filtering with CRA-ordering applied. Convergence points are black and yellow. Kernel filter size is a disk with a radius of 11 pixels.

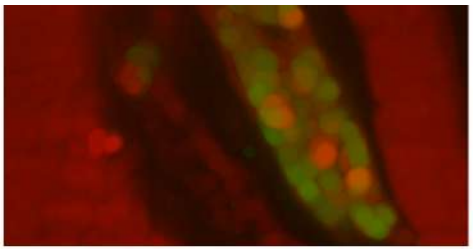

(b) Maximum filtering with CRA-ordering applied. Convergence points are black and yellow. Kernel filter size is a disk with a radius of 11 pixels.

Figure 51: 2D ganglia slice with minimum and maximum filter CRA-ordering applied.

8.2.3 Morphological Filtering Results

Following some experiments using morphological filters that have been conducted.
In table **??** for an SE of size=7.

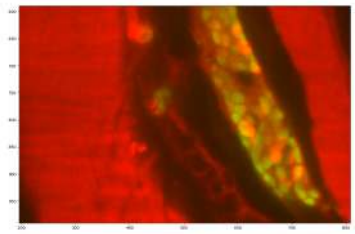

(a) Original image crop

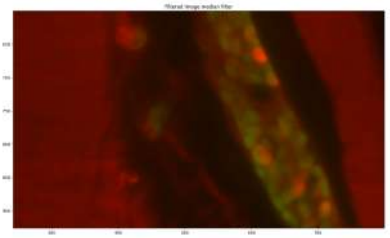

(b) Median Filter

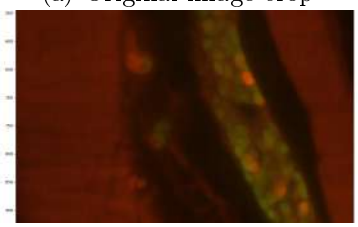

(c) Opening Filter

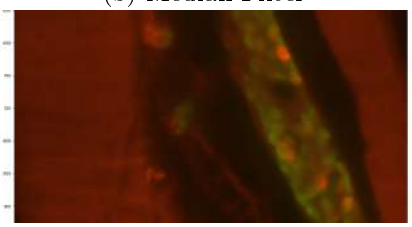

(d) Closing Filter

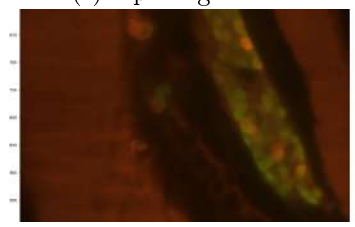

(e) Opening followed by Closing

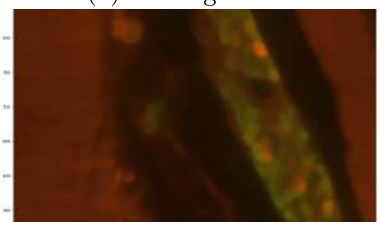

(f) Closing followed by Opening

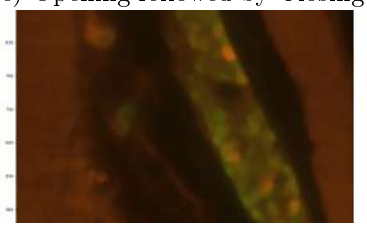

(g) Close-Open-Close Filter

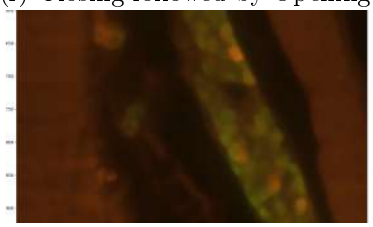

(h) Open-Close-Open Filter

Table 16: Various Morphological Filters were applied using a disk-shaped Structuring Element (SE) with a radius of 7 pixels and values in RGB 16 bits $(2^{16}, 2^{16}, 0)$, convergence points are black and yellow: (b) Median, (c) Opening, (d) Closing, (e) Open-Close, (f) Close-Open, (g) Close-Open-Close, and (h) Open-Close-Open.

In table **??** for an SE of size=19.

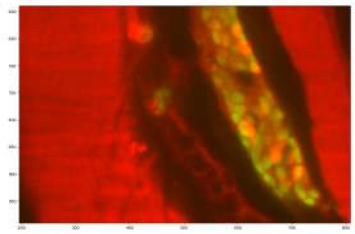

(a) Original image crop

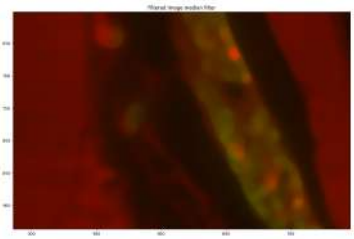

(b) Median Filter

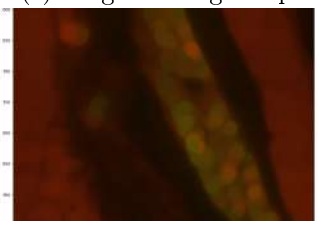

(c) Opening Filter

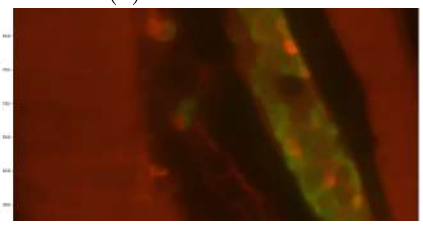

(d) Closing Filter

(e) Opening followed by Closing

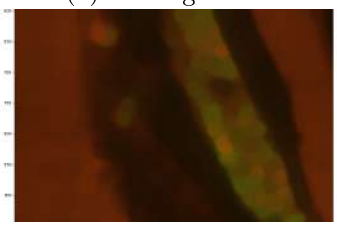

(f) Closing followed by Opening

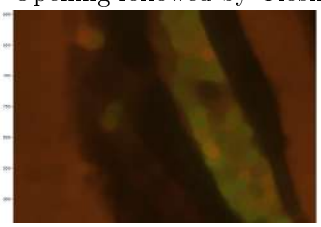

(g) Close-Open-Close Filter

(h) Open-Close-Open Filter

Table 17: Various Morphological Filters were applied using a disk-shaped Structuring Element (SE) with a radius of 19 pixels and values in RGB 16 bits $(2^{16}, 2^{16}, 0)$, convergence points are black and yellow: (b) Median, (c) Opening, (d) Closing, (e) Open-Close, (f) Close-Open, (g) Close-Open-Close, and (h) Open-Close-Open.

In table **??** for an SE of size=23.

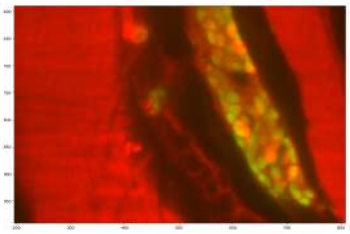

(a) Original image crop

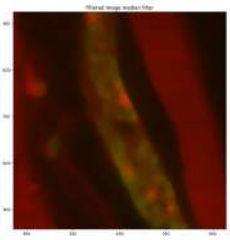

(b) Median Filter

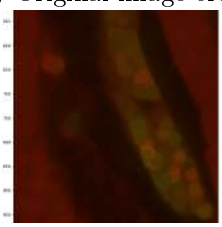

(c) Opening Filter

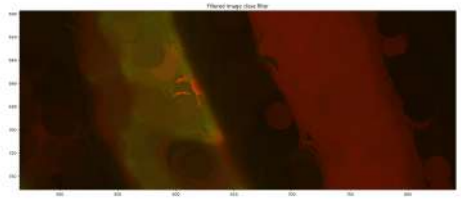

(d) Closing Filter

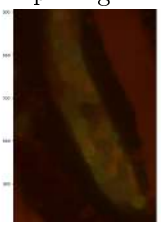

(e) Opening followed by Closing

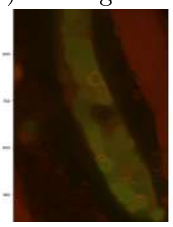

(f) Closing followed by Opening

(g) Close-Open-Close Filter

(h) Open-Close-Open Filter

Table 18: Various Morphological Filters were applied using a disk-shaped Structuring Element (SE) with a radius of 23 pixels and values in RGB 16 bits $(2^{16}, 2^{16}, 0)$, convergence points are black and green: (b) Opening, (c) Closing, (d) Open-Close, (e) Close-Open, (f) Close-Open-Close, and (g) Open-Close-Open.

Although using a larger SE leads to more rapid convergence, we have observed that the disk structures begin to merge. Therefore, the largest suitable size for the SE needs to be chosen according to the objects that needs to be processed in the image.

8.3 Appendix C: MM operators specifications

8.3.1 The Antidilation

$\delta_c(I, (-g''))^r$: The dilation with a negative SE is know to be anti-dilation. In grayscale it involves a substraction so a displacement towards $-\infty$ then applying the maximum operator. In multivariate it involves a displacement towards O_2^- then applying the multivariate maximum operator depending on the chosen ordering.

8.3.2 The Duality property:

The MM operators: Erosion and Dilation need to verify the duality property[?][?][?]. In figure **?? an illustration of this property**. Its defined as the following:

$$\delta_m(I, B) = \epsilon_m(I^c, B)^c$$
$$\epsilon_m(I, B) = \delta_m(I^c, B)^c$$

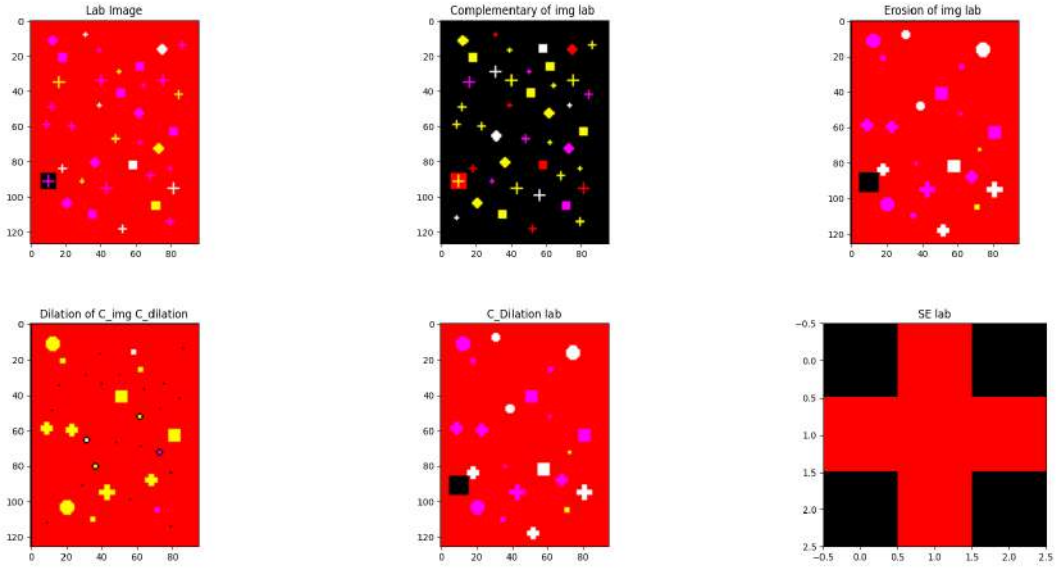

(a) Erosion of an image is identical to the complement of the dilation of the complement of the original image.

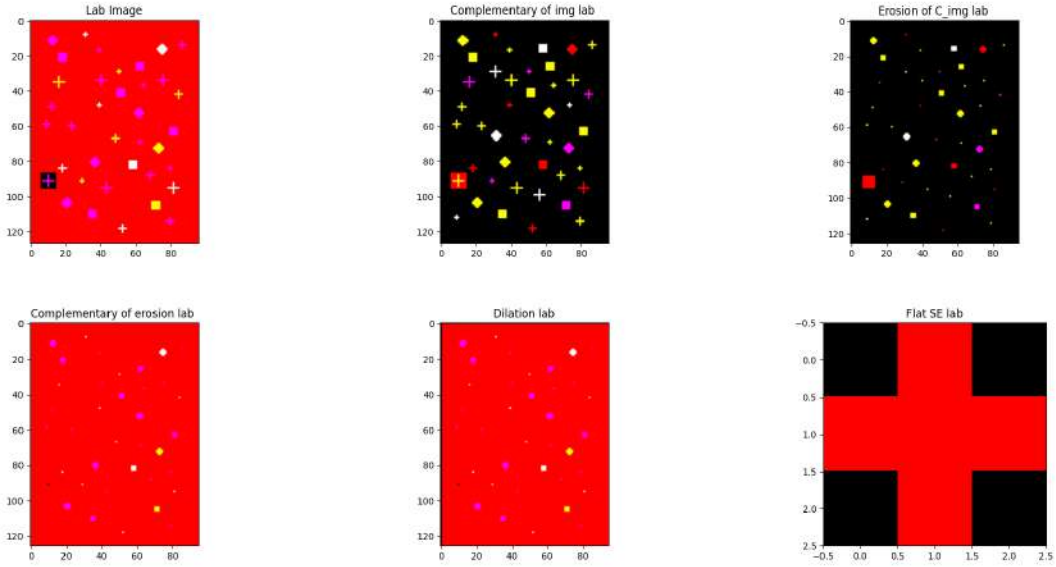

(b) Dilation of an image is identical to the complement of the erosion of the complement of the original image.

Figure 52: Duality property for multivariate MM operators verified by two definitions.

8.3.3 The complementarity:

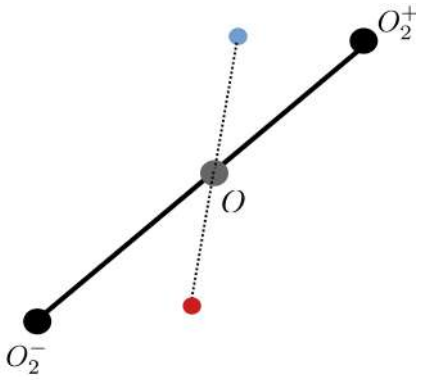

Figure 53: Complementarity of a coordinate in a multivariate space is defined as the symmetry with respect to the midpoint between the extended convergence points. The points in blue and red are complementary to each other for the considered convergence points.

8.3.4 The idempotence property:

Another property that needs to verified in mathematical morphology operators is idempotence [?]. It is essential to implement morphological filters [?]. It is illustrated in ??. It is expressed as:

$$\begin{aligned} \text{Opening: } & I \circ_m B = \delta_m((\epsilon_m(I, B)), B) \\ \text{Closing: } & A \bullet_m B = \epsilon_m((\delta_m(A, B)), B) \\ \text{Idempotence: } & A \circ_m A = A \quad \text{and} \quad A \bullet_m A = A \end{aligned}$$

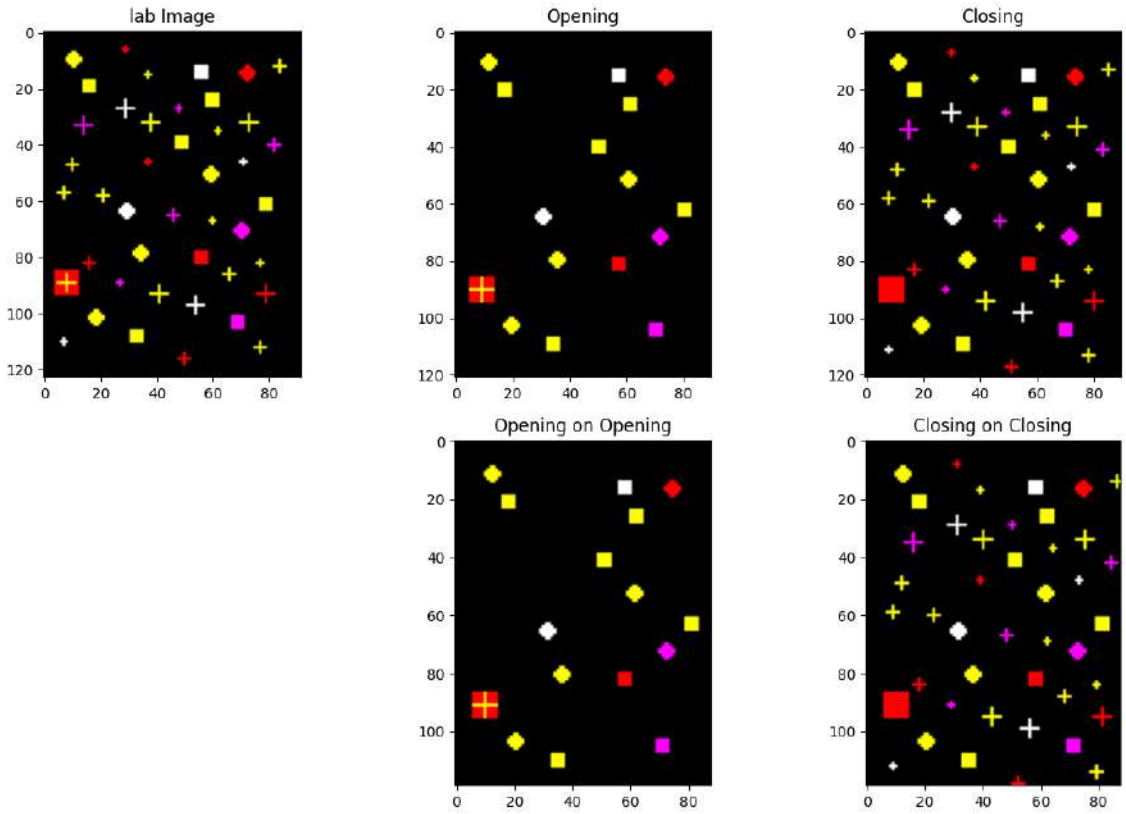

Figure 54: Idempotence property for multivariate MM (CRA based) operators: successive iterations of opening or closing do not bring additional changes to the image.

8.4 Appendix D: Statistical Methods(on 2022 dataset.)

In this sub-section, we introduce a texture descriptor designed for ganglia identification, its application in segmentation, and the outcomes of segmentation on 64x64x64 volumes selected in collaboration with the M2 pathology intern, Alice JEAN, which encompass noise, ganglia, and fibers.

The observation of histogram values in image slices or volumes is inadequate for effective classification. Within the same 3D crop, pixels can belong to various categories, such as fiber, noise, or ganglionic neurons, making pixel classification unfeasible. To identify ganglia in the initial acquisition dataset, our objective was to **derive a distinctive feature**. Texture, in this context, refers to the co-joint probability of values within a defined range and their corresponding surroundings in another range. We examined histograms of pixel surroundings (masks) extracted from different crops containing ganglia, fiber, or noise (Figure **??**). Notably, the concentration of masks corresponding to noise voxels in lower values could potentially differentiate noise regions from neurons. The descriptor encompasses the histogram of both channel values surrounding each image voxel, with the surrounding area defined by a specific cube size. After testing various sizes, we opted for cubes of 15 pixels.

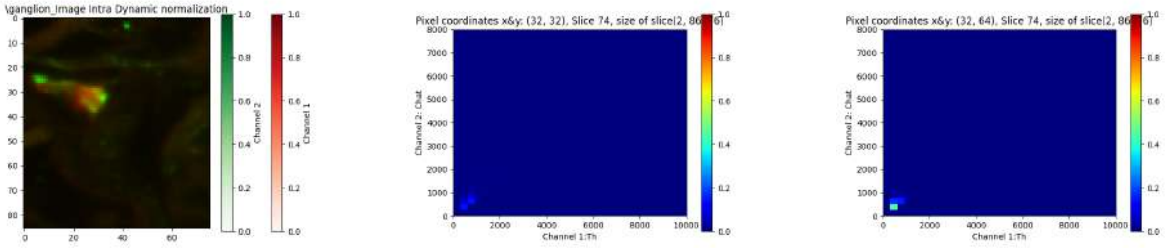

(a) Ganglia crop

(b) histogram for a chosen neurone reference pixel surrounding.

(c) histogram for a chosen noise reference pixel surrounding.

Figure 55: Observations of Intra-slice histograms for pixel surroundings with a mask size of a square of 32x32 pixels. The histogram of the noise mask is slightly more concentrated with values in the range of low channel values.

Manual references are chosen for each class: ganglionic neurons, fibers, and noise. Fibers and noises are grouped into the same class to focus on ganglia detection. Distance maps of the image pixel's descriptors to the reference descriptors are computed (Figure **??**). These distance maps are used to manually select thresholds for voxel classification and image segmentation (figure **??**). Each voxel is classified as a ganglia if it follows the rule:

$$\cdot \mathrm{d}(\mathrm{vi}, \mathrm{ref\_ganglia}) < \mathrm{d}(\mathrm{vi}, \mathrm{ref\_noise}) \quad \& \ \mathrm{d}(\mathrm{vi}, \mathrm{ref\_ganglia}) < \mathrm{d}(\mathrm{vi}, \mathrm{ref\_fibre}) \tag{4}$$

Where:

- vi represents the considered voxel's descriptor.
- ref_ganglia represents the reference descriptor for ganglia.
- ref_noise represents the reference descriptor for noise.
- distance d is the L2 norm between the two descriptors.

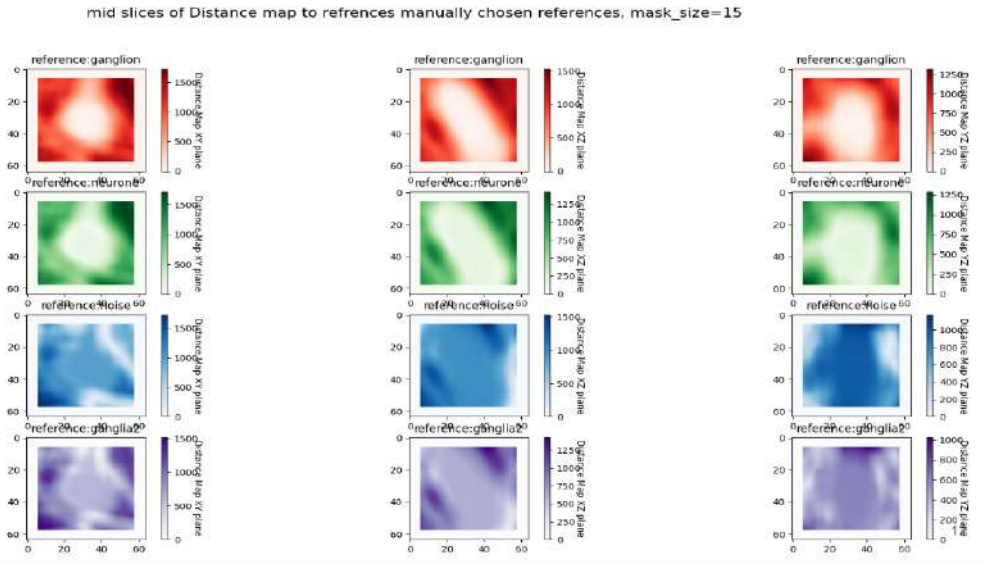

Figure 56: Distance map of mask descriptors of pixels in mid slices of a ganglia crop, viewed from three viewpoints (XY, YZ, XZ), with descriptors from a number of neurone and noise references manually chosen. Each row corresponds to the distance map of the mid slices to a different reference.

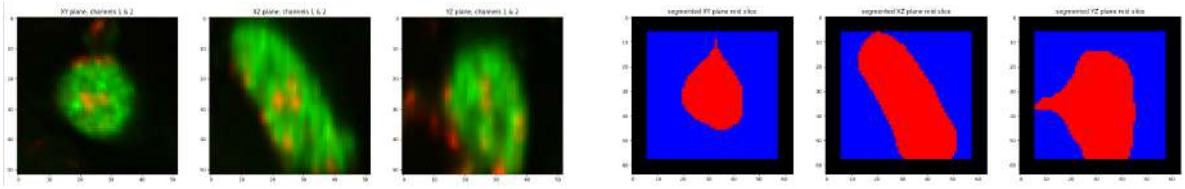

(a) The mid slices from the three points of view of a ganglia crop and its segmentation.

(b) Segmentation. In red are the ganglia-classified pixels, and in blue are the noise-classified pixels.

Figure 57: Segmentation texture descriptor-based. Segmented according to manual thresholding of distance maps of texture mask (pixel surrounding descriptors) to chosen references of neurones and noises.

The figures in Table ?? illustrate instances of mis-segmentations in our analysis. In the first case, a fiber image crop exhibits a texture resembling that of a ganglia. Despite employing different mask sizes and adding references, distinguishing it from a ganglia remains challenging. To address this, we computed the Principal Component Analysis (PCA) components on the values within this volume. Each component signifies directivity in one of the 3D directions, akin to how blob detectors identify linear or tube-like shapes [?]. When one direction's value surpasses the others after a certain threshold, it indicates a linear shape, identifying it as a fiber.

Another type of noise, undistinguishable by texture analysis, arises from marker aggregation due to inadequate heart clearing before acquisition.

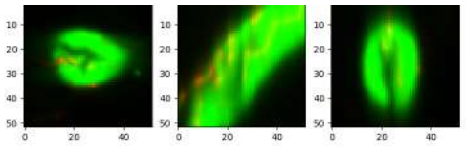

(a) Fiber mid-slices

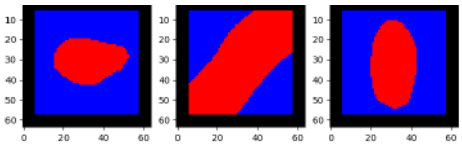

(b) Segmentation

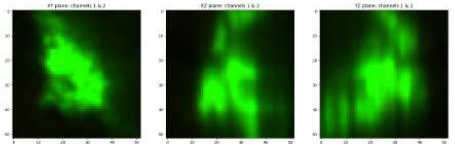

(c) Aggregated marker noise due to heart clearing protocol

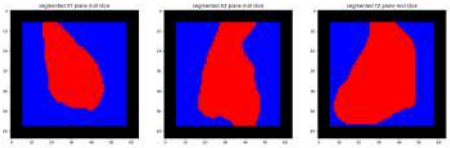

(d) Segmentation.

Table 19: Instances of Mis-segmentations using texture descriptor with a mask of size 15x15x15 pixels.

In quantifying the overall performance of this method, as we are classifying pixels inside volumes which can contain pixels that are identified as ganglia, fiber, or only noise. We calculated the percentage of voxels classified into each class, and based on a certain threshold, we determined if a volume is predicted to contain a ganglia or not (Figure **??**) then compared to the class assigned to the volume by the expert. Furthermore, to evaluate the algorithm's performance, we constructed a confusion matrix (Figure **??**). **Heart1 scores:** Accuracy: 0.80 Precision: 1.00 Recall: 0.70 F-measure: 0.82

Heart2 scores: Accuracy: 0.846 Precision: 1.00 Recall: 0.778 F-measure: 0.875

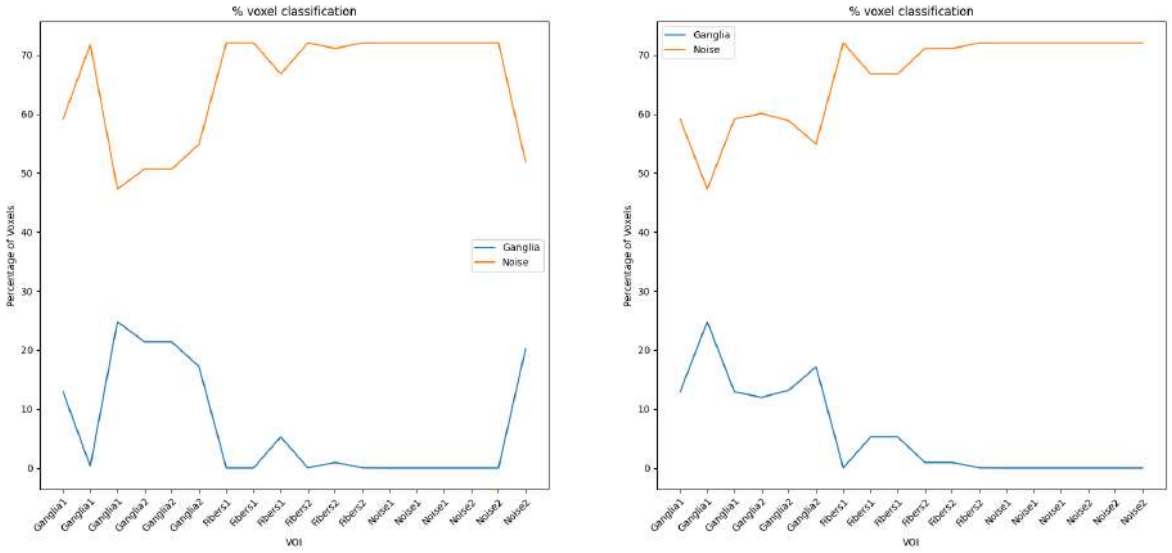

(a) heart2

(b) heart1

Figure 58: Voxel classification percentage refers to the percentage of voxels classified as belonging to a ganglion, noise, or fibers in crops extracted from the mice heart images. The same set of references is used for crops from both hearts.

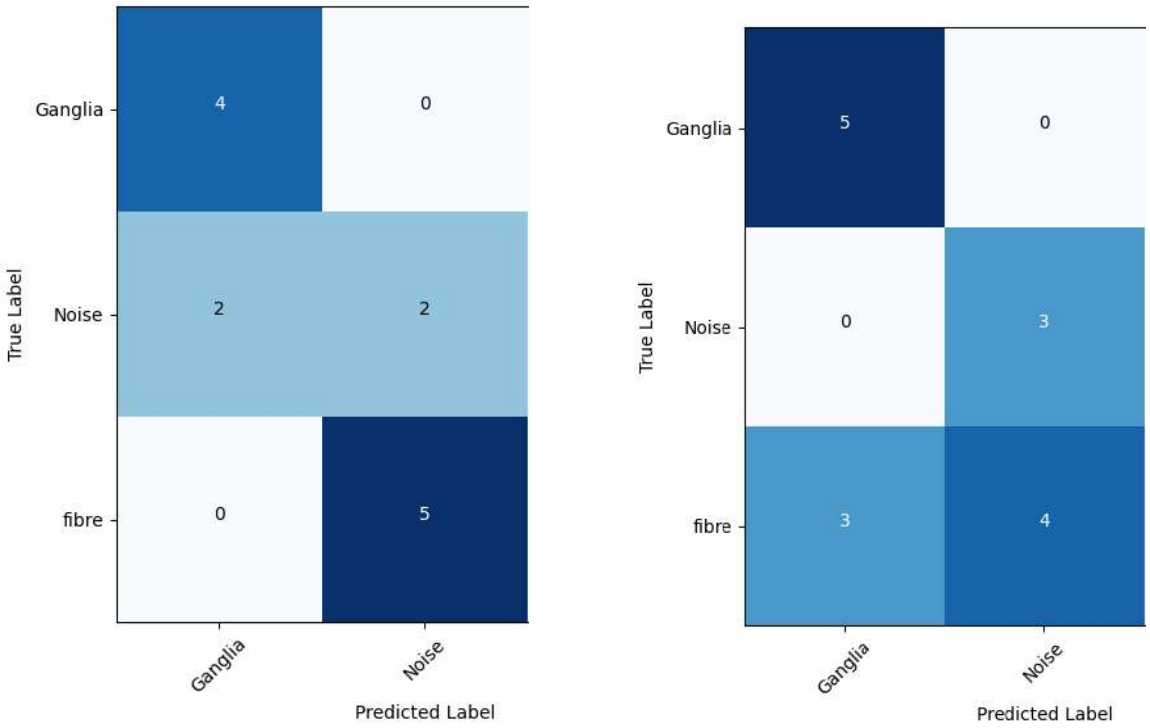

(a) heart1 (b) heart2

Figure 59: Confusion matrix for volume classification. Mask size for the descriptor is 15x15x15 pixels. Fibers are classified as noise.

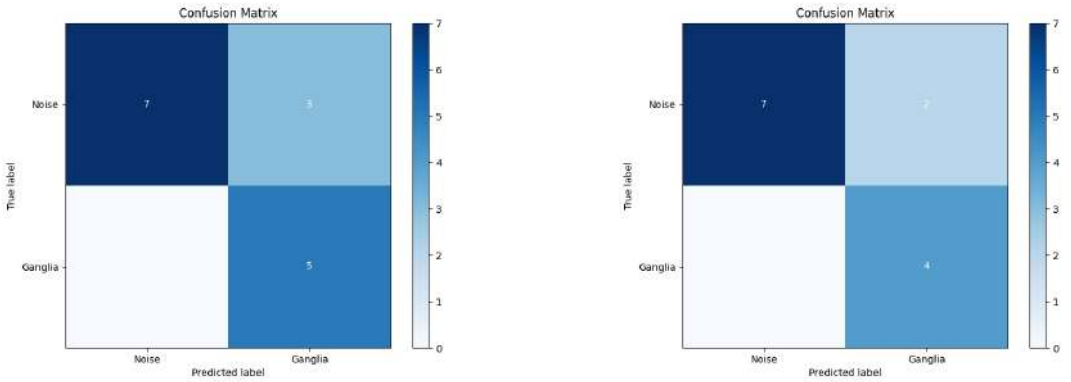

(a) heart1 (b) heart2

Figure 60: Confusion matrix for volume classification. Mask size for the descriptor is 15x15x15 pixels. Fibers are considered noise.

8.5 Appendix E: Mice Heart Observations

Table 20: Observations Of histogrames Intra slices from heart 1

	Intra normalisation	hist Intra Slice
ganglion 1	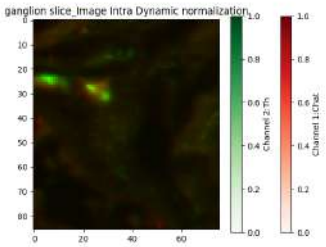	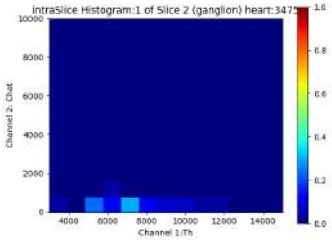
ganglion 2	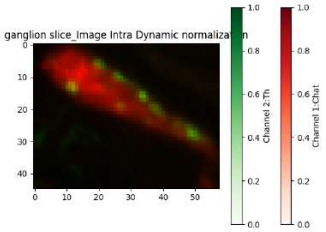	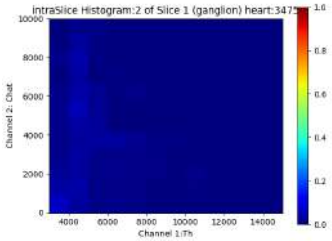
noise 1	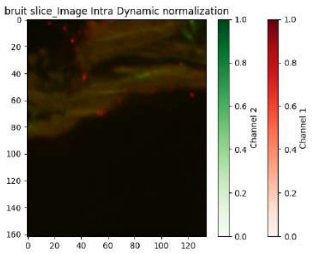	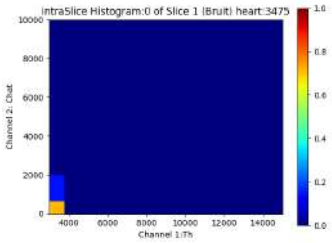
fibre 1	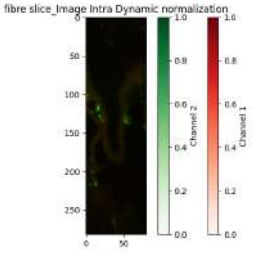	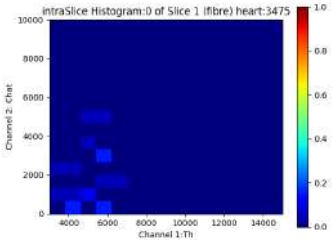
fibre 2	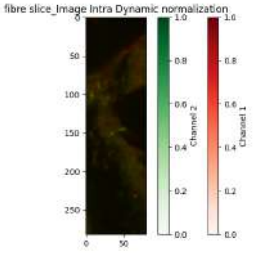	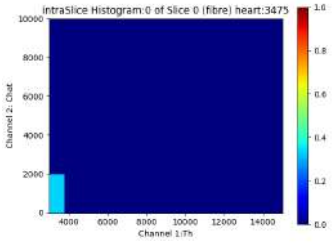

Table 21: Observations Of histograms Intra slices from heart 2

	Intra normalisation	histogram Intra Slice
ganglion 1	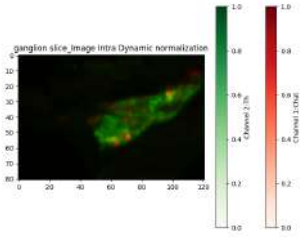	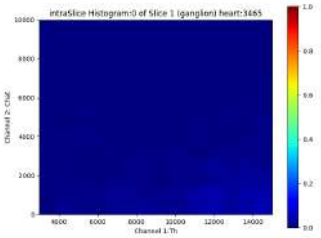
ganglion 2	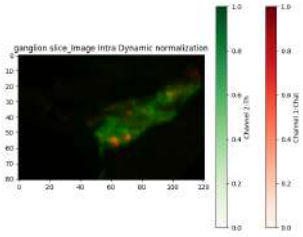	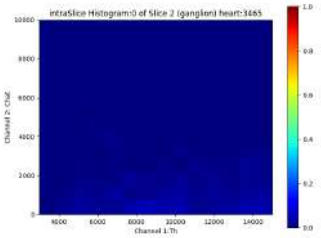
noise 1	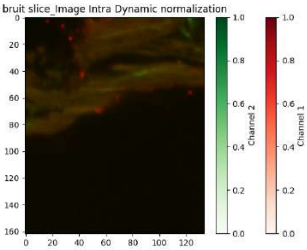	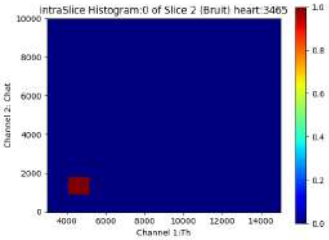
noise 2	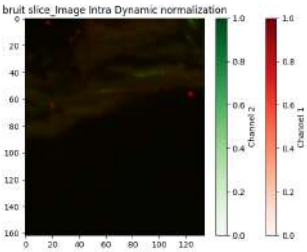	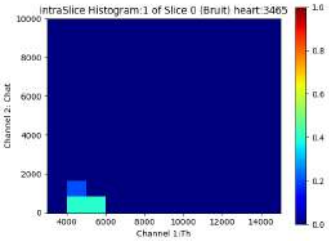
fibre 1	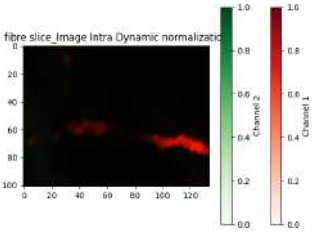	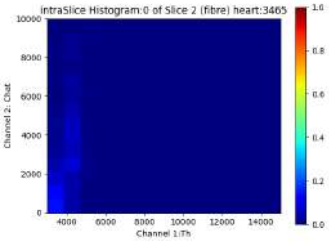
fibre 2	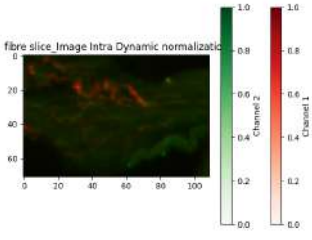	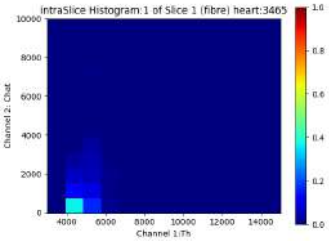

Table 22: Boxplots for zones from Heart 1

	Ganglion	Fibre	Noise
Channel 1	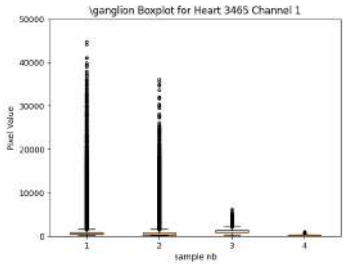	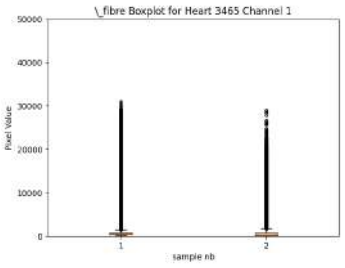	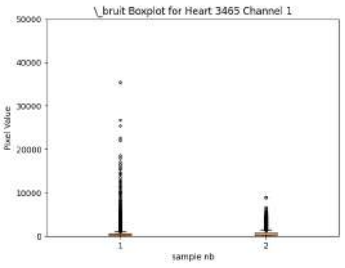
Channel 2	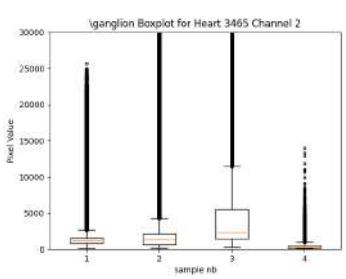	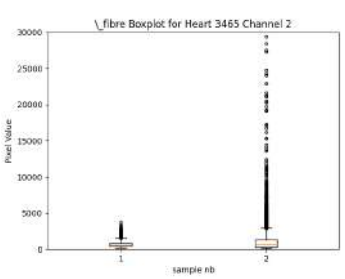	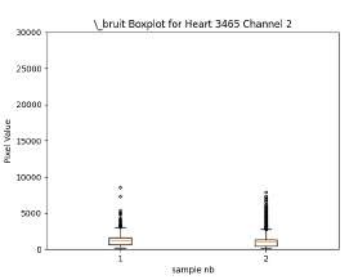

Table 23: Boxplots for zones from Heart 2

	Ganglion	Fibre	Noise
Channel 1	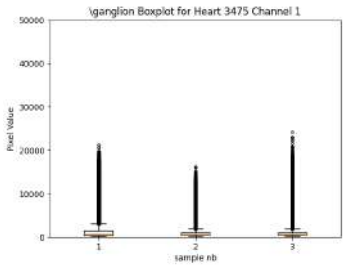	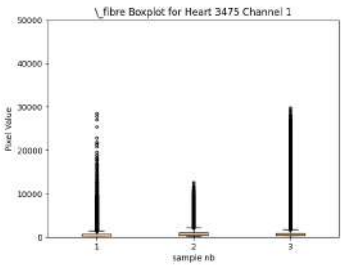	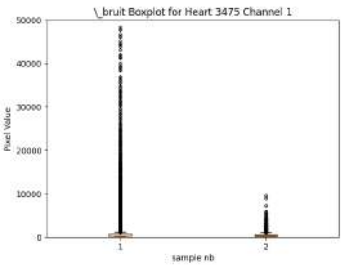
Channel 2	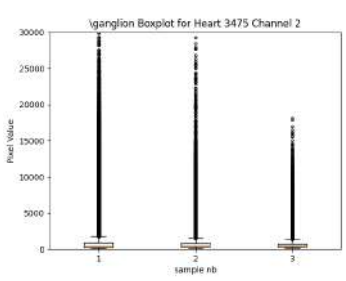	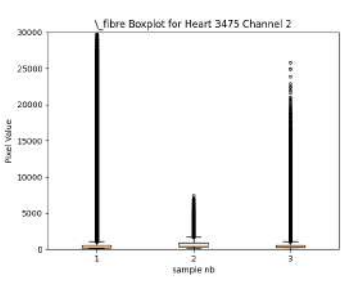	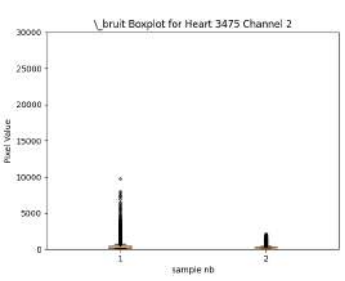

9 Summary

9.1 English

During this research internship at XLIM ICONES research team, we collaborated with the Préti pathology researchers who were acquiring 3D two-channel images of Mice heart cardiac nervous system to investigate cardiac arrhythmia. Previous attempts to analyze these images using Deep learning-based methods were not successful due to a limited dataset, normalization challenges, and a weak and indistinct marker response. To overcome these limitations, we developed handcrafted descriptors based on texture analysis to detect ganglia. Initial results on poor acquisitions showed promising outcomes, with post-processing helping to differentiate some fibers. However, some noise caused by issues in the heart clearing process during the acquisition protocol remained undifferentiated, and smaller ganglia were not always detected. Additionally, we explored multivariate mathematical Morphology-based filtering to extract specific shapes in the images and utilized probing methods to detect specific templates, particularly neurons for counting purposes. Our significant contribution was the extension of template probing methodology in Mathematical Morphology to color and multivariate images, known as CMOMP. We implemented CMOMP using an idempotent ordering of multivariate coordinates with an extended convergence points approach for multivariate mathematical morphology operators. The validation and testing of CMOMP were performed, and we are currently conducting experiments on the Mice heart images based on the perceptual distance of color.

9.2 French

Durant ce stage de recherche au sein de l'équipe de recherche XLIM ICONES, nous avons collaboré avec les chercheurs en pathologie de Préti qui effectuaient l'acquisition d'images en 3D à deux canaux du système nerveux intrinsèque dans les cœurs de souris, en investigant les arythmies cardiaques. Les tentatives précédentes d'analyser ces images à l'aide de méthodes basées sur l'apprentissage profond n'ont pas été concluantes en raison d'un jeu de données limité, de défis de normalisation et d'une réponse de marqueur faible et floue. Pour surmonter ces limitations, nous avons développé des descripteurs basés sur l'analyse de texture pour détecter les ganglions. Les résultats initiaux sur des acquisitions de faible qualité ont montré des résultats prometteurs, avec un post-traitement permettant de différencier certaines erreurs. De plus, nous avons exploré le filtrage basé sur la morphologie mathématique pour extraire des formes spécifiques dans les images et utilisé des méthodes de sondage pour détecter des modèles spécifiques, en particulier les neurones à des fins de décompte. Notre contribution a concerné l'extension de la méthodologie de sondage de modèles en morphologie mathématique aux images couleur et multivariées, connue sous le nom de CMOMP. Nous avons implémenté CMOMP en utilisant un ordre idempotent de coordonnées multivariées avec une approche de points de convergence étendue pour les opérateurs de morphologie mathématique multivariée. La validation et les tests de CMOMP ont été effectués, et nous réalisons actuellement des expériences sur les images du système nerveux intrinsèque du cœur de souris en utilisant la distance perceptuelle de couleur.